Magnetic Refrigeration for Nanoelectronics on a Cryogen-Free Platform

Inauguraldissertation

zur

Erlangung der Würde eines Doktors der Philosophie

vorgelegt der

Philosophisch-Naturwissenschaftlichen Fakultät

der Universität Basel

von

Dario Maradan

aus Val-de-Charmey (FR), Schweiz

UNI
BASEL

Basel, 2015

Genehmigt von der Philosophisch-Naturwissenschaftlichen Fakultät auf Antrag von

Prof. Dr. D. M. Zumbühl

Prof. Dr. G. A. Csáthy

Basel, den 23. Juni 2015

Prof. Dr. J. Schibler

Dekan

Melodie: Oh, my God.

Randy: What are you thinking?

Melodie: Entropy.

Randy: Entropy?

Melodie: Yeah, entropy. Boris explained it.
It's why you can't get the toothpaste back in the tube.

Randy: You mean, once something happens,
it's difficult to put it back the way it was?

— quote from "Whatever works"

a movie written and directed by Woody Allen (2009)

Abstract

Nanostructured samples serve as a playground of solid state physics due to their vast diversity of applications. In addition to various fabrication recipes and measurement methods, the temperature at which these experiments are performed plays a crucial role because thermal excitations can conceal the underlying physics. Thus advancing to lower temperatures in solid state systems might shed light on presently unknown physical phenomena, as e.g. new topological states of matter.

We present a novel type of refrigerator using adiabatic nuclear demagnetization with the goal of reaching sub-millikelvin electron temperatures in nanostructured samples. The nuclear stage consists of electronically separated Cu plates, each of which is part of a measurement lead. Before connecting to the nuclear stage, each lead is strongly filtered and then thermalized to the mixing chamber of the dilution refrigerator. This thesis presents measurements on two of these systems: the first operated in a standard, "wet" cryostat and the second on a "dry" pulse tube refrigerator. Both nuclear stages cool below 300 µK with heat leaks in the order of a few nanowatts per mol of copper.

We perform electronic transport measurements on various nanostructured samples. For the wet system, we extract electron temperatures around [5..7] mK after replacing the sample holder material and including an additional filtering stage. These measurements are highly sensitive to noise of the experimental setup and to the electrostatic environment of the devices, e.g. wafer-intrinsic charge noise. In yet another experiment on a high-mobility two-dimensional electron gas, we observe a quantization of the longitudinal resistance R_{xx} which arises from a density gradient across the wafer.

As for the dry system, we attach a home-built magnetic field fluctuation thermometer to the nuclear stage. While calibrated at 4 K, it shows good agreement with various other thermometers down to 5 mK, with the lowest temperature being 700 µK. However, electron temperatures in the samples are around 15 mK, possibly caused by the increased heat leak combined with the weakened thermalization.

Acknowledgement

All the experimental work described in this thesis would not have been possible without the help of many people. First of all, I'd like to express my gratitude to Dominik Zumbühl for being my PhD supervisor. In the numerous meetings over more than four years, he guided me through the project while his will to understand every experimental detail was always encouraging me. Dominik's various contacts to scientists around to world was useful in many cases when we felt stuck. Thanks to his motivating words whenever something was not working, be it in a tricky measurement or in a challenging piece of handicraft work, I never stopped trying.

Secondly, I would like to thank Gabor Csáthy and Rob Blaauwgeers for being part of my committee and reading my thesis. Some of Gabor's publications made the preparations for several of my group meeting talks less cumbersome and Rob was always a friendly and helpful source of information regarding the BlueFors system.

Owing to Dominik's social network, many scientists from abroad were involved in our research. First of all, I'd like to acknowledge the help and support from BlueFors Cryogenics, namely Rob Blaauwgeers, Pieter Vorselman, Tauno Knuuttila and Anssi Salmela. Whenever there was a problem with the dry system, they were immediately supplying us with helpful advice or replacement parts. Furthermore, Rob gave important input to the design of the mixing chamber piece, where we finally managed to feed through 34 wires while still being superfluid leak-tight. Along these lines, the whole microkelvin team is truly indebted to the following experts in all low temperature matters: George Pickett and Richard Haley from Lancaster University as well as Giorgio Frossati and Arlette de Waard from Leiden Cryogenics. Regarding noise thermometry and SQUIDs, Henry Barthelmess from Magnicon was very cooperative and a reliable source of information.

A large part of the experiments on the wet system is based on the fruitful collaboration with the group of Jukka Pekola from Aalto University. His team provided us

with valuable input on low temperature thermometry and theoretical background. In particular, I thank Matthias Meschke and Anna Feshchenko for the fabrication of the CBT and NIS devices.

Next, I wish to thank all current and former members of the Zumbühl group for the vivid and entertaining work environment. Most of all Lucas Casparis, who became a true friend in the years of our study and our PhD. During all those years, I appreciated his knowledge and interest in all kind of topics as well as his outstanding memory for numbers and facts – and sometimes even his "clumsiness" [47] and his pronounced lack of patience. During part of my PhD, I had the pleasure to work with Tai-Min Liu, who shared his scientific and cultural experiences with us and became a friend. I thank the master students Larissa Conrad and Samuel Hess for their commitment to the microkelvin project. Furthermore, I am thankful to Tony Clark and Kai Schwarzwälder for introducing me to low temperature physics, and to Christian Scheller for his contributions and creative ideas on filtering and measurement techniques. Finally, I'm pleased to know that the project will be continued and wish Mario Palma good luck for his PhD – may the fate be merciful with the BlueFors system.

All of this work was only possible thanks to the efficient and reliable services provided by the administrative personnel of the physics department. In particular, I'd like to acknowledge the mechanics workshop of Sascha Martin, especially Patrick Stöcklin and Stefan Gentsch, who are of extreme importance for a PhD work like mine, involving so many technical aspects. I benefited much from Michael Steinacher and his crew from the electronic workshop who supported us with useful simulations and instructive hints how to improve our measurements. I thank Dominik Sifrig for the reliable supply of cryoliquids and for helping us maintaining lab devices. Barbara Kammermann and Astrid Kalt are heavily acknowledged for relieving me from many administrative matters.

Last but not least, I am truly indebted to my parents for financial and moral backing and to my girlfriend Leonie for her support and listening to my physics problems.

Contents

1 Introduction & Motivation

Physics is the science that aspires to gain and increase knowledge of nature in order to get a better understanding of the world we live in. Owing to the newly acquired ability of researchers to observe phenomena at very small scales, quantum physics started to evolve in the beginning of the 20^{th} century and paved the way for modern physics. The impact was tremendous and the confusion about how this new understanding of physics in the microscopic scale can be brought into agreement with the macroscopic conception of our everyday life was ubiquitous. My main motivation to study physics always was to better understand the world around us and to gain the ability to explain phenomena that will seem like miracles to someone who is neither used to it nor aware of the underlying principles, which often reveal themselves only on an atomic level, as e.g. in electricity, magnetism or photonics.

Since also in chemistry and biology most processes ultimately occur on very small scales, physics also influences living organisms. In the early years of quantum physics, famous physicists like Erwin Schrödinger were thinking about the effect of quantum physics on life in general. He argued in a book [1] that complex life has to necessarily exceed the microscopic scale to prevent the statistical uncertainties that are inevitably bound to small scales and numbers. In other words, if a biological cell would consist of a few atoms only, it would be impossible for this cell to perform a specific task, since the cell is subject to the laws of statistics and random thermal excitations.

However, it is important to understand the basic physical principles at the level of elementary particles and single atoms in order to acquire a complete picture. By drawing our attention to non-living matter, immense progress in condensed matter physics [2] achieved in the last decades allows humanity nowadays to build up tailor-made structures which can be used to probe and utilize these quantum mechanical effects. Due to the small energies involved, quantum effects are only revealed when the samples are cooled to temperatures below which the thermal energy is less than their

characteristic energy scale, for example the energy separation between the many-body ground state and the first excited state. Besides temperature, other environmental effects, e.g. impurity scattering or charge noise, can prevent or at least reduce the visibility of these effects, too.

In recent years, many new phenomena in condensed matter physics have been theoretically proposed and partially discovered by cooling devices to progressively lower temperatures. Examples include qubit systems showing entanglement [3] and strongly correlated states in semiconductor devices as helical nuclear spin ordering in a 1D system [4–6] or fragile fractional quantum Hall states [7–12]. At low temperatures, electrons often reveal a collective behavior in these systems, which was successfully described by the introduction of so-called quasiparticles. Examples of such quasiparticles include composite fermions [13], Dirac fermions [14, 15], Majorana fermions [16, 17] and topologically trivial or non-trivial particles [18–20] as well as particles with non-integral statistics [21, 22]. Some of these exotic quasiparticles in fractional quantum Hall devices or semiconductor / superconductor hybrid samples are considered for topological quantum computation [23, 24]. Furthermore, cooling to ever lower temperatures also facilitated the investigation of detrimental effects like remote alloy disorder and local impurity scattering for integer quantum Hall states [25, 26] and more exotic fractional quantum Hall states [27]. Other experiments shed some light on the phenomenon of reentrant integer quantum Hall states [28], which is still not completely understood.

There are only a few research groups performing nanoelectronic experiments at temperatures below 10 mK. While not making any claim to be complete, examples include mainly experiments on quantum Hall samples [7, 9, 10, 27–34] but also on 1-D wires [4]. In the range between [10..30] mK, experiments include investigations on the Kondo effect [35], antidots [36] as well as shot noise measurements [37, 38] and quantum Hall devices [24, 25].

Even though the techniques for cooling to microkelvin or even nanokelvin temperatures are at hand, the emphasis of the ultralow temperature community focused on the

investigation of quantum fluids and pure metals [39, 40]. Quite recently, the idea came up to open the range of microkelvin temperatures to nanostructured devices – which is the main objective of this thesis. In comparison to earlier measurements at microkelvin temperatures, there are two important changes: First, the nanostructured sample must be connected to the outside world by several measurements leads. Whereas the simplest devices are two- or four-terminal, more complicated structures as for example double quantum dots employ numerous gates and contacts and require easily 15 wires or more. Secondly, the sample must be connected to a cold reservoir by an efficient thermal link to drain residual heat leaks.

1.1 A New Concept

At low millikelvin temperatures, different degrees of freedom inside a solid start to decouple which complicates thermal conductance and thus efficient cooling in a low temperature apparatus. In particular, the lattice excitations (phonons) start to freeze out and can therefore not be used to transport heat anymore. Thus, cooling nanodevices gets very challenging and the choice of an appropriate cooling technique as well as a careful choice of materials becomes essential. A promising approach is to use conduction electrons to thermally couple the sample to the coldest spot of the refrigerator, because they are always present in electronic transport measurements, either in metals or doped semiconductors.

Since the technique of adiabatic nuclear demagnetization (AND) is well-established [41–46] and it is known that the cold nuclei are able to absorb heat from the surrounding electronic system, the pioneering idea arose to build an AND stage with a number of parallel nuclear refrigerators (NRs), each of which is serving as an electronically isolated measurement lead connected to the sample. This should then allow to cool the sample under investigation directly by using the electrons rather than the phonons.

1.2 Thesis Outline

A prototype of such a refrigerator consisting of 12 NRs in parallel was built as a proof of principle apparatus. For reasons of completeness, a publication presenting the new concept and describing this system can be found in appendix A. This work was done during my master's studies and can be seen as my entry into the field, leading to the PhD thesis at hand. After introducing some general background information needed to understand the concept of using AND to cool nanodevices and putting it into a broader context, I describe the efforts achieved on a second generation stage with 21 NRs. This part describes measurements with a focus on thermometry with devices like Coulomb Blockade Thermometers (CBT, chapter 3), single and double quantum dots (chapter 4), fractional quantum Hall samples (chapter 5) and Normal-metal / Insulator / Superconductor junctions (NIS, chapter 6). A more detailed description of the design and the assembly of this system, which is housed in a cryostat, is described in detail in Lucas' PhD thesis [47] and in my master's thesis [48]. The entirety of the experiments presented here demonstrates the usefulness of our approach, although various barriers have been revealed which currently limit our lowest temperature readings.

In a second part, I will focus on a third generation setup implemented on a "dry" cryogen-free platform. This nuclear stage consists of 16 parallel NRs and is equipped with a magnetic field fluctuation thermometer, described in chapters 7 and 8. The implementation of AND on a cryocooler, which uses a double-stage pulse tube to provide the starting temperature for the dilution refrigerator of 4 K (provided by the ^{4}He bath in a standard "wet" system in a cryostat), only became possible in recent years owing to heavily decreased vibrations levels in state-of-the-art pulse tube systems. Nevertheless, the vibrations levels are still higher than in a conventional wet system, necessitating a very careful design of the AND stage.

At the end, I will conclude in chapter 9 naming existing issues and possible solutions and give an outlook on possible future experiments.

2 Introduction to Nuclear Refrigeration for Nanoelectronic Samples

Dilution refrigerators are the work horses for most low temperature laboratories. By solution and separation of the two isotopes ^{3}He and ^{4}He [49], temperatures around 10 mK are commonly reached, whereas the best systems can reach temperatures as low as 2 mK in continuous operation [50, 51]. Using adiabatic nuclear demagnetization (AND) [52, 53], temperature can be decreased even more [54], but in contrast to dilution refrigeration, it is a single-shot technique. Refrigerators with two AND stages in series have been intensively used to investigate nuclear magnetic ordering phenomena and the behavior of ^{3}He at microkelvin temperatures. The lowest temperatures in metals measured were also reached with this method: electrons were cooled below 10 µK in Pt [39] and the nuclear spin system below 300 pK in Rh [40].

Since it is impossible to perfectly decouple a system from its environment, there will always be some heat flow into any object whose temperature is lower than the environment's temperature. The same applies for a cryogenic apparatus: all the parts are ultimately connected to room temperature. As an additional difficulty, certain degrees of freedom in solid matter start to decouple at low temperatures. This emphasizes the importance of a suitable refrigeration technique and of a clever choice of materials.

Hence cooling nanodevices to temperatures in the microkelvin regime is a formidable challenge. The thermal coupling between the liquid helium of a dilution refrigerator, e.g. in the mixing chamber (MC), and a solid gets strongly suppressed at temperatures below ~ 100 mK due to the Kapitza boundary resistance [45], and a similar weakening is observed for the electron-phonon coupling, see chapter 2.1.2. A promising approach is therefore to use the conduction electrons for thermal coupling at microkelvin temperatures – which is compatible with AND (chapters 2.1.3 and 2.2) because nuclear refrigerators can be chosen to be metallic.

This chapter presents the topics from low temperature physics which are relevant for cooling nanostructured samples. Firstly, physical properties like heat capacity and thermal conductivity at low temperatures will be discussed. Secondly, I will introduce possible sources of heat leaks and their effects on low temperature environments. At last this chapter will close with a general introduction to adiabatic nuclear refrigeration and different methods of thermometry. A large part of these topics can also be found in textbooks, e.g. Refs. [41, 42, 44–46, 55, 56], but they are recapitulated here and flavored with some important project-related information.

2.1 Basic Concepts

The process of "cooling" an object physically denotes "removing heat" from it. Thus, two tasks have to be fulfilled to efficiently thermalize a reservoir A with temperature T_A to a cold reservoir B at temperature T_B: the thermal contact between A and B has to be maximized and the heat $\dot{Q}$ flowing into A has to be minimized. This simple point of view illustrates that every low temperature apparatus has to be carefully designed and built to achieve $T_A \approx T_B$. The dependence of the thermal conductivity on material parameters, geometry and temperature is discussed in the following paragraphs. Possible sources of $\dot{Q}$ are listed in chapter 2.1.4. Methods like on-chip cooling are not considered here (see Ref. [57] and references therein).

2.1.1 Thermal Conductance of Solids at Low Temperatures

Many physical properties of heat transport have an analog in electricity: a temperature gradient (voltage) leads to a heat flow (current), whereas the amount of heat flow depends on the thermal resistance (electrical resistance) of the path. Thus using an approximation, heat flow can be described by a linear response theory, where elementary excitations from electrons, phonons or more exotic quasiparticles [58] carry energy and therewith enable heat transport.

Due to the fact that objects of our interest are usually larger than typical mean free paths of the particles carrying the energy excitations, the conduction of heat is a diffusive rather than a ballistic process. The rate of heat flow per unit area $\dot{q} = \dot{Q}/A$ resulting from a temperature gradient ∇T can be written as [45]

$$\dot{q} = -\kappa \nabla T \,. \tag{2.1}$$

In a simple model heat is carried by additive channels whereof we consider two, namely conduction electrons and phonons, such that $\kappa = \kappa_{el} + \kappa_{ph}$. Using kinetic gas theory by depicting the heat carriers (electrons or phonons) as a gas diffusing through the material with velocity v, we get for the thermal conductivity [44]

$$\kappa = \frac{1}{3} c_m v \lambda = \frac{1}{3} c_m v^2 \tau \,, \tag{2.2}$$

with molar heat capacity c_m, mean free path $\lambda = v\tau$ and scattering rate τ. In other words, the thermal conductance is given by the product of the transported quantity (here: c_m), the velocity of this transport and the distance until the carrier is scattered again. The factor 1/3 demonstrates the limitation of the carriers moving in three dimensions to a unidirectional flow. In order to understand processes of heat conduction at low temperatures, we will enlighten the temperature dependence of the parameters on the right-hand side of Eq. (2.2) for phonons as well as for electrons in the following paragraphs.

As mentioned above, phonons are not reliable heat carriers at low temperatures anymore. The reason for that arises from the phonon density, and consequently their scattering rate and heat capacity. At $T \leq 100\,\mathrm{K}$, not all phonon degrees of freedoms can be excited anymore because the thermal energy $k_B T$ becomes comparable to the energy needed for lattice vibrations. The temperature at which phonons begin to "freeze out" is called Debye temperature Θ_D, and the molar vibrational heat capacity of phonons is $c_{ph} \propto (T/\Theta_D)^3$. This means that only few phonon modes are excited

for $T \ll \Theta_D$, the mean free path is dominated by scattering at crystal boundaries and defects [44] rather than phonon-phonon scattering, i.e. independent of T.

The important quantity for the velocity is how fast vibrations (excitations) can be transferred through the lattice by phonons. This is characterized by the sound velocity v_s of phonons, which is typically in the order of $10^3\,\mathrm{m/s}$ for solids and independent of temperature [59]. So, we end with a cubic temperature dependence of the thermal conductivity from phonons: $\kappa_{ph} \propto T^3$. As opposed to room temperature this thermal conduction path is heavily suppressed at low temperatures, it is the only mechanism present in insulators.

In the case of electrons, only particles close to the Fermi energy E_F can move freely and therewith participate in heat transport, because they can perform transitions to higher non-occupied states. This allows us to replace v by the Fermi velocity v_F (typically $10^5 - 10^6\,\mathrm{m/s}$, so $v_F \gg v_s$), which is temperature independent. At temperatures below a few kelvin, the number of phonons is small and electrons mainly scatter on lattice defects and impurities, as we have found for the phonons, again making the mean free path temperature independent. Thus, the last parameter to be discussed is the molar electron heat capacity, which below the Fermi temperature is given by $c_{m,e} = \gamma T$ with the Sommerfeld constant γ. Because the temperature dependence is only carried by $c_{m,e}$, we obtain a linear scaling of electronic thermal conductivity with temperature: $\kappa_{el} \propto T$. This assures reasonably good thermal conductance for metals at low temperatures.

In the introduction of this chapter, I mentioned the analogy between electricity and heat. Now, we found that the free electrons in metals do not exclusively transfer charge but also heat. This fact facilitates to estimate κ of a metal by measuring its electrical conductivity σ – a material property that is easily measurable. Following the same reasoning as above, also σ is constant at low T [60]. The ratio between κ and σ should therefore be proportional to T caused by $\kappa_{el} \propto T$. Using a Fermi-Dirac distribution around E_F, we can insert $v_F^2 = \frac{2E_F}{m^*}$ and $c_e = \frac{\pi^2 k_B T}{2E_F} n_e k_B$ into Eq. (2.2). After inserting

the electrical conductivity from the Drude model, $\sigma = \frac{n_e e^2 \tau}{m^*}$ with electron density n_e and effective electron mass m^*, we get the Wiedemann-Franz law [56]

$$\frac{\kappa}{\sigma} = \frac{\pi^2 k_B^2}{3e^2} T = L_0 T \tag{2.3}$$

with the Lorenz number $L_0 \approx 2.445 \cdot 10^{-8}\,\mathrm{W\,\Omega\,K^{-2}}$. Although this relation holds for many metals, variations of L_0 have been observed in some metals at the lowest temperatures due to more exotic scattering processes as e.g. the Kondo effect [45]. By combining Eqs. (2.2) and (2.3), we can calculate the rate of heat flow $\dot{Q}$ arising from an electrical resistance R between two reservoirs with electron temperatures $T_{e,1}$ and $T_{e,2}$:

$$\dot{Q}_e = \frac{\pi^2 k_B^2}{6e^2 R} \left(T_{e,2}^2 - T_{e,1}^2 \right) . \tag{2.4}$$

Since both, electrical and thermal conductivity, are limited by the mean free path of the electrons at low temperatures, this emphasizes the importance of using high purity metals with low defect scattering to assure large κ_{el}. A simple method to characterize the number of scattering impurities is to measure the electrical resistivity $\rho = 1/\sigma$ at room temperature (RT) and at low temperature (typically at liquid He temperature), i.e. phonon scattering versus defect scattering regime. The ratio of these quantities is called the residual resistivity ratio (RRR) and represents a direct figure of merit of the metal's purity [44, 45]

$$\mathrm{RRR} = \frac{\rho_{300\,\mathrm{K}}}{\rho_{4.2\,\mathrm{K}}} = \frac{\sigma_{4.2\,\mathrm{K}}}{\sigma_{300\,\mathrm{K}}} . \tag{2.5}$$

For superconductors, we find a situation similar to insulators. Because there are essentially no free electrons available at the chemical potential due to the superconducting gap Δ, heat can be conducted only by phonons and quasiparticles. The latter are exponentially suppressed for $T < T_c$, where T_c is the critical temperature of the super-

conductor. Hence, the thermal conductivity of a superconductor κ_{sc} approaches the phonon behavior ($\propto T^3$) for temperatures well below T_c. Due to the fact that superconductors can easily be coerced in their normal conducting state by a magnetic field, we can use the large difference between κ_{sc} and κ_{el} as a heat switch. The ratio is typically $\kappa_{el}/\kappa_{sc} \sim 10^4$ for $T \ll T_c$ (see appendix A), but can be as large as $10^6 - 10^7$ [45, 54].

In summary, we conclude that the total heat capacity at $T \ll \Theta_D$ is $c_m = \gamma T + \beta T^3$, consisting of an electron (linear in T) and a phonon (cubic in T) term. The total thermal conductivity is given accordingly as $\kappa = \kappa_{el} + \kappa_{ph}$. This means that for mK temperatures, κ_{el} dominates in metals and doped semiconductors and assures a reasonable thermal conductivity. κ_{ph} prevails in insulators and superconductors because there are no free electrons, but it can be extremely small. In order to achieve good thermal contact, metals with a high purity (large RRR) should be used due to their large thermal conductivity caused by low impurity scattering.

2.1.2 Thermal Coupling at Interfaces

The variable properties outlined in the previous chapter entail the use of diversified materials in a low temperature apparatus. This chapter introduces the temperature dependence of thermal coupling mechanisms at interfaces between solids and fluids.

Metals are popular materials to work with at low temperatures because of their thermal conductivity. However, metals like Al and Cu form oxide layers on their surfaces when exposed to air, which deteriorates the thermal conductance across boundaries. For Al, this effect is very detrimental, so the best remedy is to melt the metals at the interface, i.e. use fused contacts rather than just surface contacts [42, 61]. For Cu on the other hand, the oxidation process is not as severe. Nevertheless, Cu contacts are normally coated with a thin layer of Au (e.g. by electrochemical gold plating) to avoid thermal conductance degradation over time [56] and pressed together with a high force. Whenever possible, fused or spot-welded joints are preferred by reason of their small ρ and large κ. For a press contact between two metals, the thermal conductance is often

found to be proportional to the applied force. Soldering is not a good option because most (soft) solders become superconducting and behave like a dielectric or, in other words, like a heat switch with regard to thermal conductance [45].

Another important interface is the boundary between liquid ^{3}He/^{4}He and metals, for example in the mixing chamber (MC) of a dilution refrigerator. If one wants to cool an object, one has to thermally couple it effectively to the liquid He inside the MC. This coupling mechanism is described by a thermal boundary impedance called Kapitza resistance R_{Kap} [42, 44] and varies strongly with temperature

$$R_{\mathrm{Kap}} = \frac{\Delta T}{\dot{Q}} \propto \frac{1}{AT^3}\,, \tag{2.6}$$

where A is the area of the interface. Whereas the left part of this equation is generally valid, the right-hand side describes the thermal impedance between liquid He and bulk Ag ($\propto T^{-3}$) in a temperature range of [10..100] mK. The reason for this weak coupling is twofold: on the one hand, the large difference of the sound velocities in liquid He and in a metal (factor ~ 20) leads to a critical angle of 3°, and on the other hand, the acoustic impedances differ by about 10^3 [62]. This results in less than 1 out of 10^5 phonons being able to cross the helium-metal boundary. Below $T \approx 10\,\mathrm{mK}$, there is a crossover to $R_{\mathrm{Kap}} \propto T^{-1}$ due to soft phonon modes [45]. To facilitate cooling of metals inside the MC, one therefore increases the surface area A by using metal powder sinters [41, 45, 55, 63].

2.1.3 Thermal Coupling Between Nuclei, Electrons and Phonons

There are three subsystems in an ordinary metal or semiconductor: nuclei, electrons and phonons. Every species can interact with itself as well as with other species – but the thermal coupling strength depends strongly on temperature in the range of our interest. Generally, thermal equilibrium can be reached much faster among a certain species than with other degrees of freedom, which allows us to assign different

temperatures to the subsystems. For instance, the spin-spin relaxation time τ_2 needed to establish thermal equilibrium among the nuclei at temperature T_n is in the order of 1 ms for typical metals [45].

As an example of coupling between two subsystems, we consider the heat $\dot{Q}_{e-ph}$ flowing from the electron system at temperature T_e to the phonon system at temperature T_{ph}:

$$\dot{Q}_{e-ph} = \Omega\Sigma\left(T_{ph}^5 - T_e^5\right) \tag{2.7}$$

Here, Ω depicts the volume and Σ the electron-phonon coupling constant (for Cu: $2 \cdot 10^9\,\mathrm{W\,K^{-5}\,m^{-3}}$ [59]). The strong power-law indicates a heavy suppression of the coupling between phonons and electrons at low temperatures, complicating the cooling of electrons via the lattice phonons.

Since we are interested in low electron temperatures in nanostructured samples, we have to find a more efficient coupling mechanism. One possible and practical avenue is to use the hyperfine interaction between nuclei and electrons. This interplay is based on the electromagnetic interaction between the magnetic moments of the electrons and the nuclei and is reasonably strong even at very low temperatures. The time needed to reach thermal equilibrium between the electronic and the nuclear system τ_1 ("spin-lattice relaxation time") is defined [41, 64] through

$$\frac{dT_n^{-1}}{dt} = \frac{T_n - T_e}{KT_n} = -\frac{T_n^{-1} - T_e^{-1}}{\tau_1}\,. \tag{2.8}$$

The inverse nuclear temperature T_n^{-1} on the left-hand side arises from the conversion of nuclear magnetization to temperature using the Curie law. Since the dominant term in the hyperfine interaction is the overlap of the electron wave function at the site of the nucleus, it is particularly strong for metals with valence electrons in the *s*-shell. Again, only electrons close to E_F can exchange energy with the nuclei, because free states within the exchanged energy difference have to be accessible. This leads to the formulation of the Korringa law

$$K = \tau_1 T_e \tag{2.9}$$

with the Korringa constant K defining the strength of the hyperfine coupling [45]. K is independent of temperature but becomes a function of magnetic field if the applied field B is comparable to the internal field of the material. At $T_e < 1\,\mathrm{mK}$, τ_1 is typically in the order of several days for insulators and superconductors, whereas for metals $\tau_1 \sim 1\,\mathrm{h}$ owing to the presence of conduction electrons.

For the special case of AND where $T_n \leq T_e$, this situation further improves due to another effect. The nuclei are absorbing heat from the electrons and we can write the heat flow [45] as

$$\dot{Q} = nC_e\dot{T}_e = -nC_n\dot{T}_n\,, \tag{2.10}$$

where n is the amount of material in mol, C_e and C_n denote the specific heat of electrons and nuclei (see Eq. (2.18)), respectively, and $\dot{T} = dT/dt$. By using Eqs. (2.8) and (2.9), we find

$$\dot{T}_n = (T_e - T_n)T_n/K \tag{2.11}$$

and thus the rate of change of electronic temperature

$$\dot{T}_e = -\left(T_e - T_n\right)\frac{T_n C_n}{K C_e}\,. \tag{2.12}$$

Hence the hot electrons come into equilibrium with the nuclei much faster than predicted by the pristine Korringa law because $C_e \ll C_n(B, T_n)$ for moderate B and low T_n. This results in an effective time constant

$$\tau_{1,\mathrm{eff}} = \frac{\tau_1 C_e}{C_n + C_e} \approx \frac{\tau_1 C_e}{C_n}\,. \tag{2.13}$$

In summary, choosing a material with an appropriate K (which has to be a metal, see chapter 2.2.2) is an important technical aspect for the performance of an AND stage intended to cool electrons. The equilibration time needed for hot electrons to cool to $\sim T_n$ is rather short because in case of AND the heat capacity of the cold nuclear spin reservoir is much larger than the heat capacity of the warmer conduction electrons.

2.1.4 Sources of Heat

The physical fact that energy always flows from hot to cold complicates measurements at ultra-low temperatures. This gets more and more challenging the lower the temperatures are, because a given amount of heat will create a larger temperature gradient at ultra-low T compared to elevated temperatures. As in every other low temperature apparatus, heat can arise in an AND system from multiple sources – the most prominent of which will be discussed here.

Probably the most obvious candidate is the heat flow originating from higher temperature stages. This contribution can be split into three parts: thermal conductance through (i) residual gas particles, (ii) solid materials assuring the stability of the AND stage and (iii) thermal blackbody radiation according to the Stefan-Boltzmann law. However, by operating the AND stage in high vacuum ($p < 10^{-5}\,\mathrm{mbar}$) and choosing appropriate materials in combination with careful radiation shielding [46], heat leaks arising from higher T stages can be reduced to $\ll 1\,\mathrm{nW}$ per mol of NR material.

Another heat source is eddy current heating $\dot{Q}_{\mathrm{eddy}}$. If a time-varying magnetic field $\dot{B}$ is applied to an electrically conductive material, eddy currents are generated according to the formula [45]

$$\dot{Q}_{\mathrm{eddy}} = \frac{GV\dot{B}^2}{\rho}\,, \text{ with } \quad \dot{B} = \frac{dB}{dt} \propto \frac{dB}{d\vec{r}}\frac{d\vec{r}}{dt}\,. \tag{2.14}$$

Here, G is a geometry factor and V the volume of the conductor. The same effect is observed in a static magnetic field, if the conductor is moving in a region of inhomo-

geneous B due to vibrations $d\vec{r}/dt$. On a similar note, vibrations can lead to frictional heating if two solid pieces are not strongly bolted. Mechanical vibrations can arise from compressors, pumps, ventilation motors, building activities or even from people interfering with the experiment. For an AND system on a pulse tube (PT) driven refrigerator, vibrations caused by the PT compressor and remote motor are the most obvious and strongest source of heat leaks, for which reason actions against vibrations are particularly important, see chapter 7.

By far less obvious is the heat leak from emitted energy due to internal relaxation in materials, often referred to as heat release. These time-dependent processes follow a power law and are not only contingent on the material itself but also on its manufacturing method. One commonly known example is the exothermic ortho-para conversion of H_2 in copper: Ref. [45] reports a heat leak of 5 nW one week after cooldown caused by 1 ppm of hydrogen in 1 kg of Cu. Another group of processes are structural relaxations often present in noncrystalline and amorphous materials [44] like ceramics and epoxies (two-level-system tunneling). Therefore one should minimize the amount of materials like glue, grease, epoxy and plastics. In the course of our experiments on the AND system in a standard dewar with cryofluids (see chapters 3 to 5), the lowest electron temperatures $T_e \sim [5..6]$ mK [47] have only been observed after the ceramic (Macor) chip socket was replaced with a Ag epoxy socket featuring additional Ag epoxy filters [65]. Figure 2.1 further emphasizes that substantial temperature differences ΔT can result from tiny heat leaks, depending on the thermal conductance $\kappa(T)$ of the material.

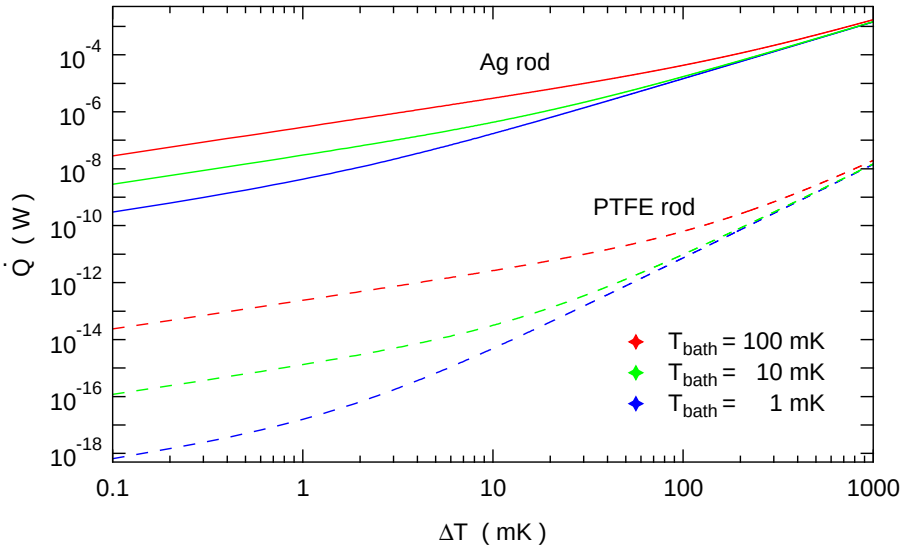

Figure 2.1: $\dot{Q}$ needed to create a certain ΔT across a Ag (RRR = 1′000) and PTFE rod, respectively, with the same geometry (diameter $d = 2\,\mathrm{mm}$, length $l = 200\,\mathrm{mm}$) at three different bath temperatures $T_{\mathrm{bath}} = 100$, 10 and 1 mK. Values for $\kappa(T) \propto T^a$ are taken from Ref. [45] with material-dependent exponents a. Independent of the material, there is a low temperature regime in the expansion $\dot{Q} \propto \left[(T_{\mathrm{bath}} + \Delta T)^{a+1} - T_{\mathrm{bath}}^{a+1}\right]$ where a term linear in ΔT prevails and a high-temperature regime where ΔT^{a+1} dominates.

Regarding the sample, two additional origins of heat come into play. On the one hand, radio-frequency (rf) radiation coupled into the low temperature environment from RT can cause a considerable amount of heat. In order to avoid rf heating, all the measurement leads are made of lossy thermocoax [66] or twisted pair wires between RT and 4 K. Before they connect to the sample, additional low-pass filtering is performed at low T. On the other hand, samples as well as temperature sensors can suffer from Joule heating [56] due to the interplay of a finite electrical resistance R and the bias voltage V_{bias} or current I_{bias} applied to measure their transport properties or temperature

$$\dot{Q}_{\mathrm{Joule}} = R I_{\mathrm{bias}}^2 = \frac{V_{\mathrm{bias}}^2}{R}\,. \tag{2.15}$$

To minimize resistive heating, the bias has to be carefully adjusted to small values where no heating can be observed. In some special situations as e.g. in the fabrication of ohmic contacts to 2DEGs, R can be minimized [67, 68].

A detailed description of the design and the filtering configuration to minimize heat leaks in the AND system based on a pulse tube platform is given in chapter 7.1. Similar characterizations for the AND system housed in a standard dewar with cryofluids can be found in Refs. [47, 48].

2.2 Adiabatic Nuclear Demagnetization

The process of adiabatic nuclear demagnetization (AND) is a well-established single-shot technique that can be used to reach ultra-low temperatures. Its sequence can be split into four parts [45, 69]. First, the magnetic field B at the nuclear refrigerator (NR) is ramped up to an initial field B_i of several tesla. This process generates nuclear spin polarization and hence also a significant heat of magnetization in the NR [62], which is drained by a dilution refrigerator in the second step – the precooling. Here, a large cooling power of the dilution refrigerator and a high thermal conductance between the MC and the NR is essential to precool the NR to a temperature T_i. Next, the NR is thermally isolated from the MC by superconducting heat switches [61] and B is ramped down adiabatically to a final field B_f, preserving the nuclear spin polarization. For ideal adiabaticity, a final temperature of $T_f = T_i \cdot B_f/B_i$ is reached. In a last step, experiments can be performed at these ultra-low temperatures for time spans of hours, days or even weeks (or in extreme cases months [70]), depending on B_f and the heat leaking into the system. All of these steps will be discussed in more detail below.

To explain the principle of AND, the thermodynamics are sufficiently described by an ensemble of non-interacting nuclei with spin I and magnetic moment μ_n in a magnetic field B [45]. The Zeeman effect leads to a splitting of the spin states at energies

$$E_Z = -m\mu_n g_n B \tag{2.16}$$

with the magnetic quantum number m running from $-I$ to $+I$ and the nuclear g-factor g_n. In the limit of high temperatures ($k_B T \gg E_Z$), the molar entropy of the

nuclear spins is

$$S_n = R \ln (2I + 1) - \frac{\lambda_n B^2}{2\mu_0 T_n^2}\,, \tag{2.17}$$

where R is the molar gas constant, λ_n the molar Curie constant and μ_0 the vacuum permeability. Using the relation $C_B = T\left(\frac{\partial S}{\partial T}\right)_B$, we then deduce the Schottky-law for the nuclear specific heat

$$C_n(B,T) = \frac{\lambda_n B^2}{\mu_0 T_n^2}\,. \tag{2.18}$$

As introduced in the previous chapter, the nuclear specific heat $C_n(B,T)$ gets very large in magnetic fields, but temperatures between $[10..20]\,\mathrm{mK}$ are necessary to attain a reasonable nuclear polarization, see Fig. 2.2. Note that both, molar nuclear spin entropy and nuclear specific heat, are functions of B/T only. At the end of the precooling, the thermal path between NR and MC is cut by ramping a small heat-switch field B_{HS} from 15 mT to zero. The critical field of the Al heat switches is in the order of $B_{c,\mathrm{Al}} = 10.5\,\mathrm{mT}$ and excited quasiparticles are highly suppressed because $T \ll T_{c,\mathrm{Al}} = 1.1\,\mathrm{K}$ [71]. During the demagnetization, the entropy (and therewith also the relative polarization, Fig. 2.2) stays constant for a perfectly adiabatic process, $S(B_i/T_i) = S(B_f/T_f)$, and consequently we find

$$\frac{B_i}{T_i} = \frac{B_f}{T_f} \qquad \rightarrow \qquad T_f = T_i\,\frac{B_f}{B_i}\,, \tag{2.19}$$

i.e. the final temperature T_f is the product of the precooling temperature T_i and the inverse field reduction factor. The lowest possible B_f is given by the internal field of the NR, where internal interactions will align the nuclei's magnetic moments. Further, the high-temperature approximation $k_B T \ll E_Z$ can break down. However, in both our AND setups substantial heat leaks in the order of nW prevent us from demagnetizing to $B_f < 50\,\mathrm{mT}$, such that we encounter neither the limit of the internal field nor of the

high-temperature approximation.

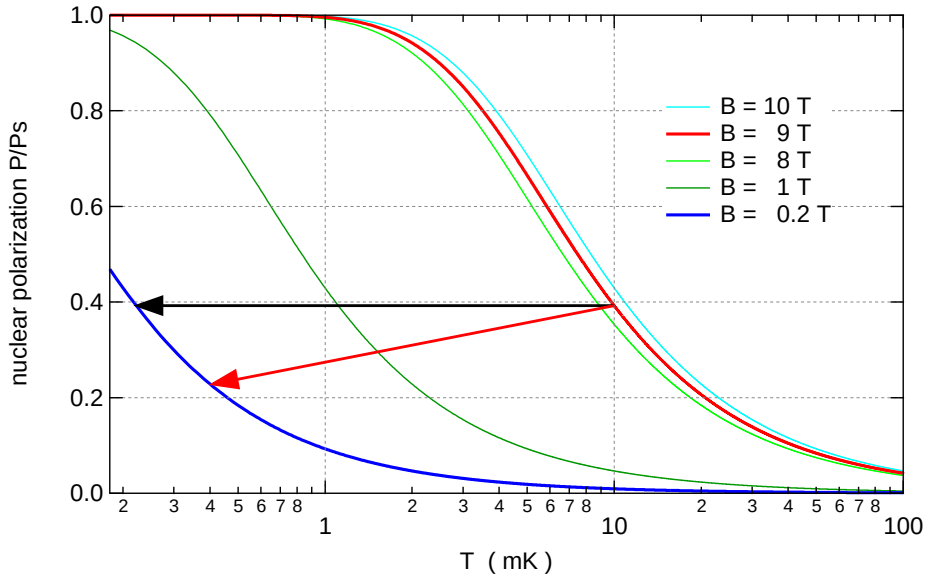

Figure 2.2: Relative polarization of Cu nuclei versus temperature for different magnetic fields B calculated using Eq. (9.15c) in Ref. [45]. In a typical demagnetization run, we reach a precooling temperature of roughly 10 mK in a field of 9 T (red trace), which results in about 40 % of polarized nuclei. Assuming perfect adiabaticity during the demagnetization process ($\dot{Q} = 0$, black arrow), the fraction of polarized nuclei (and therewith also the entropy) is constant, resulting in $T_f = 222\,\mu\text{K}$ for $B_f = 0.2\,\text{T}$ (blue trace). A deviation from perfect adiabaticity results in increased final temperatures (red arrow, $T_{f,\dot{Q}} = 400\,\mu\text{K}$).

2.2.1 Influence of Static and Dynamic Heat Leaks

For a more realistic description of the AND process, an external heat load $\dot{Q} > 0$ has to be considered. Such a heat load can arise from one of the sources discussed in chapter 2.1.4. Even for a perfectly shielded and filtered setup, a finite heat leak is generated by eddy currents due to the demagnetization. A heat leak will lead to a loss of spin polarization and thus cause a deviation from perfect adiabaticity, as indicated by the red arrow in Fig. 2.2.

Since the heat flowing in the AND stage has to be absorbed by the cold reservoir, i.e. the nuclei, we can write

$$\int \dot{Q} dt = \int n C_n(B,T) dT\,. \tag{2.20}$$

Since the important quantity is the heat load per mol of nuclear stage material, we introduce the molar heat leak $\dot{Q}_m = \dot{Q}/n$. By combining Eqs. (2.10), (2.11) and (2.18), we can deduce the temperature difference between the electronic and the nuclear system resulting from $\dot{Q}_m$ as

$$\dot{Q}_m = C_n(B, T_n)\dot{T}_n = (T_e - T_n)\,\frac{\lambda_n B^2}{\mu_0 K T_n}\,, \tag{2.21}$$

which can be rewritten as

$$\frac{T_e}{T_n} = 1 + \frac{\mu_0 K \dot{Q}_m}{\lambda_n B^2}\,. \tag{2.22}$$

The latter equation indicates that $\dot{Q}_m$ is raising T_e above T_n. The temperature difference between T_e and T_n grows at small B due to the decreasing nuclear heat capacity. Therefore a certain optimum in final field $B_{f,\mathrm{opt}}$ exists, where T_e is minimal

$$B_{f,\mathrm{opt}} = \sqrt{\frac{\mu_0 K \dot{Q}_m}{\lambda_n}}\,. \tag{2.23}$$

In general, the total $\dot{Q}_m$ consists of an eddy current term due to the demagnetization $\dot{Q}_{\mathrm{eddy}}$, which can be calculated using Eq. (2.14), and a residual, intrinsic heat leak $\dot{Q}_i$ arising from other sources. Thus we can estimate the total energy loss ΔE during the AND process with a given ramp rate $\dot{B}$, assuming $\dot{Q}_i$ to be independent of B and T. Figure 2.3 shows the energy loss versus the ramp rate $\dot{B}$ for different intrinsic heat leaks $\dot{Q}_i$. The eddy current heating is calculated using Eq. (2.14) for the NR geometry of the AND stage on the PT setup (2x[34 x 1.7 x 120] mm^3) and RRR = 250. The optimum ramp rate is indicated by black dots. The larger the intrinsic heat leak, the less important is the eddy current term and thus the ramp rate should be increased.

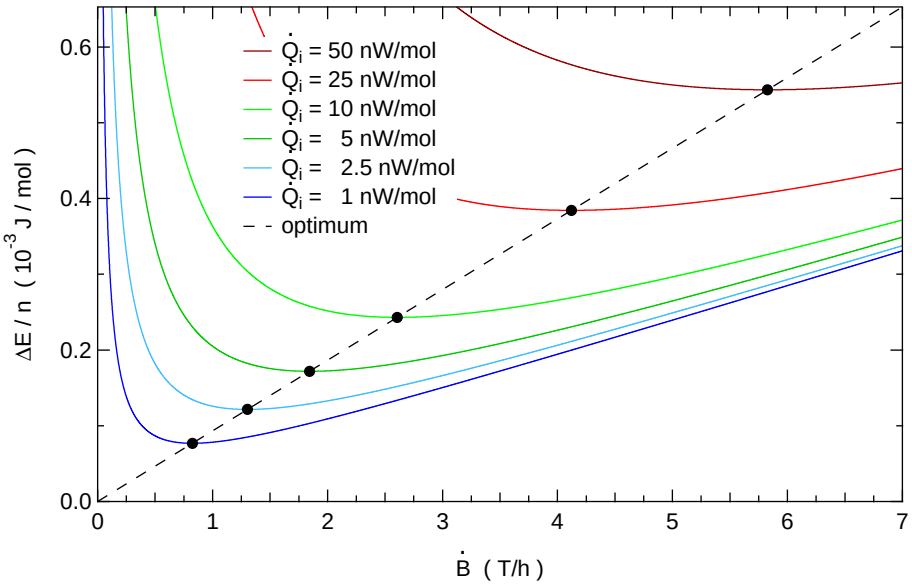

Figure 2.3: Molar energy loss $\Delta E/n$ during demagnetization from $B_i = 9\,\mathrm{T}$ to $B_f = 0.2\,\mathrm{T}$ versus ramp rate $\dot{B}$. The loss increases at high $\dot{B}$ because of large eddy current heating and at low $\dot{B}$ because of a long exposure to an intrinsic molar heat leak $\dot{Q}_i$. The optimum $\dot{B}$ (i.e. minimum in $\Delta E/n$, black dots) depends on $\dot{Q}_i$ (see text).

As AND is a single-shot technique, the question arises how long a system can stay in its "cold state" for a given B_f and $\dot{Q}_m$. Using the rate of change in nuclear temperature (right hand side of Eq. (2.10)), we can calculate the time t in which the NR at temperature $T_{n,1}$ will warm up to $T_{n,2}$ being exposed to a certain $\dot{Q}_m$ [45]:

$$t = \frac{\lambda_n B_f^2}{\mu_0 \dot{Q}_m} \left(T_{n,1}^{-1} - T_{n,2}^{-1} \right) . \tag{2.24}$$

Besides determining an important figure of merit of the AND stage, this relation can also be used for thermometry. Because many thermometers measure electronic rather than nuclear temperatures, the equation for the electronic temperatures is derived in chapter 2.3, see Eq. (2.27). As a further performance parameter, we define the efficiency ξ of the AND process from the ideal final temperature $T_{f,id}$ and the measured final temperature T_f according to

$$\xi = \frac{T_{f,id}}{T_f} = \frac{T_i}{T_f} \frac{B_f}{B_i} . \tag{2.25}$$

For a perfectly adiabatic AND process the efficiency is $\xi = 100\,\%$. If all the spin polarization is lost during demagnetization, $\xi = 0\,\%$.

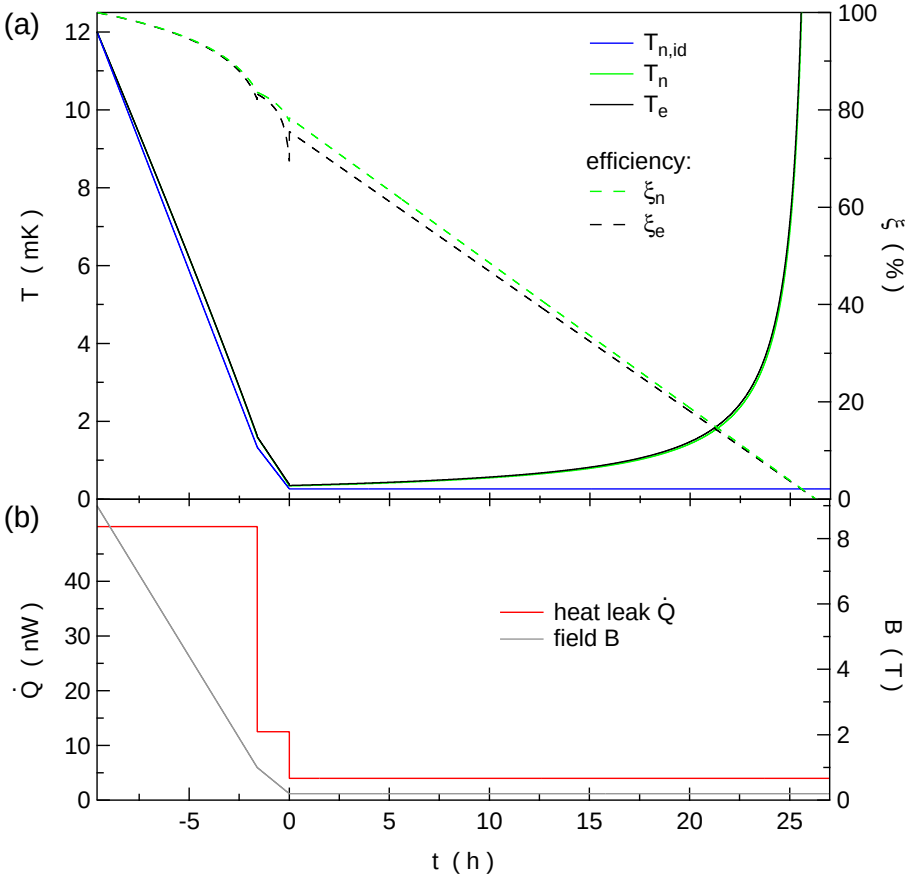

Figure 2.4: Simulation of an exemplary demagnetization process. (a) Temperature (left axis) and efficiency (right axis) versus time t for a typical AND run. $T_{n,\mathrm{id}}$ depicts the behavior of the nuclear temperature in a perfectly adiabatic process (blue), T_n (green) and T_e (black) indicate the nuclear and electron temperatures, respectively, under a finite heat load. Demagnetization starts at $t = -9.6\,\mathrm{h}$ from $T_i = 12\,\mathrm{mK}$ at $B_i = 9\,\mathrm{T}$. At $t = 0$, $B_f = 0.2\,\mathrm{T}$ is reached and the lowest temperatures are $T_{n,f} = 341\,\mu\mathrm{K}$ ($\xi_n = 78\,\%$) and $T_{e,f} = 382\,\mu\mathrm{K}$ ($\xi_e = 70\,\%$). Subsequently the NR warms up under a constant heat load. (b) Heat leak $\dot{Q}$ (red, left axis) versus time. $\dot{Q}_1$ is 50 nW/mol between 9 and 1 T, where $\dot{B}_1 = 1\,\mathrm{T/h}$, and $\dot{Q}_2 = 12.5\,\mathrm{nW/mol}$ for $\dot{B}_2 = 0.5\,\mathrm{T/h}$ between $B = 1\,\mathrm{T}$ and $B_f = 0.2\,\mathrm{T}$ due to $\dot{Q}_{\mathrm{eddy}} \propto \dot{B}^2$. The heat leak during the warm-up ($t > 0$) is 4 nW/mol. The demagnetization field B (gray) versus time is plotted at the right axis.

The equations presented above allow us to simulate an AND run. Figure 2.4 shows an exemplary AND process including warm-up from $B_i = 9\,\mathrm{T}$ to $B = 1\,\mathrm{T}$ with $\dot{B}_1 = 1\,\mathrm{T/h}$ and then to $B_f = 0.2\,\mathrm{T}$ with $\dot{B}_2 = 0.5\,\mathrm{T/h}$. The molar heat leaks during

demagnetization are assumed to be $\dot{Q}_1 = 50\,\mathrm{nW/mol}$ and $\dot{Q}_2 = \dot{Q}_1/4 = 12.5\,\mathrm{nW/mol}$ for the respective ramping steps 1 and 2. The residual heat leak in the warm-up state (i.e. at $t > 0$) is $\dot{Q} = 4\,\mathrm{nW/mol}$. Due to the large ratio C_n/C_e, there are jumps in the efficiency of the electron temperatures when the heat leak changes. The lowest temperatures in this exemplary demagnetization run are $T_e = 381\,\mu\mathrm{K}$ ($\xi_e = 75\,\%$) and $T_n = 341\,\mu\mathrm{K}$ ($\xi_n = 78\,\%$) at $t = 0$. According to this simulation, the AND stage can stay below 1 mK for 17.0 h and below 2 mK for 21.6 h (for T_e). The source code for this simulation of the AND process can be found in appendix B.

2.2.2 Refrigerator Material Considerations

A NR can be built from different materials, but there are a lot of requirements [41]. Most of the physical material properties have been discussed above, but the following list should give an overview and motivate why we chose Cu as a NR material. The material demands for successful AND are ...

- A considerable part of the material should possess a nuclear spin $I > 0$ such that its energy levels are split in a magnetic field according to Eq. (2.16).
- A large nuclear Curie constant is necessary to ensure a large heat capacity (Eq. (2.18)) and thus a large cooling power.
- The Korringa constant K should be small for a fast coupling to the electrons, as indicated by Eq. (2.9).
- The material must not be superconducting even at the lowest temperatures. This would impede the thermal conductance and the thermal coupling between nuclei and electrons.
- The electronic ordering temperature of the NR should be much lower than the temperature range of interest, since the nuclei would align along this internal magnetic field.

- A high purity is important for the material to achieve reasonable electrical and thermal conductance at the lowest T, see Eqs. (2.3) and (2.5).
- The material should be easily machinable. It has to be possible to make low-resistive contacts to another material / metal.

To meet all of these criteria is difficult and some of the requirements are contradictory, as for example a high electronic density at E_F (i.e. small K) also enhances electronic magnetism and superconductivity. In the end, some materials as In, Nb, Cu and $PrNi_5$ fulfill most of these criteria. In and Nb have a large nuclear spin of $I = 9/2$, but they are superconductors with critical fields of 30 mT and 200 mT, respectively.

As in many other ultra-low T laboratories, Cu was chosen as a NR material for both of our AND setups, albeit its severe demand on the precooling temperature to attain a reasonable spin polarization, see Fig. 2.2. Cu has a reasonable nuclear spin of $I = 3/2$ and a nuclear Curie constant of $\lambda_n/\mu_0 = 3.22\,\mu\mathrm{J\,K\,T^{-2}\,mol^{-1}}$ [45]. Its Korringa constant $K = 1.27\,\mathrm{K\,s}$ is sufficiently low to facilitate efficient thermal coupling. The nuclear spins in Cu order only at 58 nK [72], thus allowing to demagnetize to very low $B_f \sim 10\,\mathrm{mT}$. By precooling to $T_i \sim 12\,\mathrm{mK}$ in $B_i = 9\,\mathrm{T}$, ultra-low temperatures of $T_f < 50\,\mu\mathrm{K}$ can be reached with small but finite $\dot{Q}_m$. Cu is available in very high purities and can be easily machined. The spot welding technique can be used to achieve very low-resistive contacts to other metals.

Since H_2 is often used in the purification process of metals but a deal-breaker for successful AND (see chapter 2.1.4), we decided to use a special ETP1 alloy of Cu called NOSV, supplied by Aurubis (Hamburg, Germany). This alloy contains a considerable amount of O_2 (108 ppm), but almost no H_2. The RRR is specified to be larger than 420 in the native state, i.e. without annealing. Since the purity of the material is a trade-off between large thermal conductivity (as well as low heat leak) and large eddy current heating, the Cu used in our AND stages was not annealed after machining. The heat release of NOSV copper was measured to be $< 3.7\,\mathrm{pW/g}$ in Ref. [73], which corresponds to $< 235\,\mathrm{pW\,mol^{-1}}$. This is well below the usual literature values for standard Cu.

The last material in the list, $PrNi_5$, also exhibits some appealing properties and should be considered as a serious competitor of Cu. Compared to Cu, it has a large hyperfine enhancement and less stringent requirements on precooling temperatures and initial magnetic field: $T_i \sim 25\,\mathrm{mK}$ and $B_i \sim 6\,\mathrm{T}$ are sufficient. The bulk resistivity of $PrNi_5$ is comparable to the one of brass and thus minimizes eddy current heating. Furthermore, nuclear spin ordering allows for demagnetization to $B_f = 0\,\mathrm{T}$. In combination with the large ρ, this will substantially reduce eddy current heating during and after demagnetization. The ferromagnetic Curie temperature of $PrNi_5$ was found to be 0.4 mK and the Korringa constant $K < 10\,\mu\mathrm{K\,s}$ [74], the lowest K among all tested materials. By reason of more complicated handling and the limitation to $T_f \geq 0.4\,\mathrm{mK}$, we considered Cu to be a better choice at the time when the experiment was planned and designed.

2.3 Thermometry

The motivation to cool devices to ever lower temperatures arises from the reduction of thermal excitations that represent an ubiquitous energy scale in solid state systems. Because of this reason, an exact measurement of the temperatures in a low-temperature apparatus gains in importance – be it in different locations of the refrigerator or in different subsystems of the sample of interest that can be thermally decoupled from each other. However, exact temperature measurements get challenging at temperatures below $\sim [5..10]\,\mathrm{mK}$ and thus particularly in AND systems, since already the smallest amount of heat impinging on the thermometer can raise its temperature substantially above the "real" temperature.

There is a large variety of different thermometers that can be used in the mK-range. They can be differentiated in two groups: primary and secondary thermometers. Whereas the former can directly be used to read temperature from a single measurement just by using known relations and physical constants, the latter have to be calibrated against another primary (or secondary) thermometer at one or several temperatures.

Here, I will discuss exclusively the thermometers used in our AND systems, namely paramagnetic salt thermometers, fixed-point devices and RuO_2 resistors. The magnetic field fluctuation thermometer designed and built for the AND system on the PT platform is described in detail in chapters 7.2 and 8. All of those thermometers are susceptible to magnetic fields and have to be carefully shielded.

Nowadays, commercial dilution refrigerators are usually delivered with calibrated resistive thermometers (e.g. Ge, carbon Speer, RuO_2, ... [42]) at different locations, of particular importance in the MC. These kind of thermometers are of secondary nature and suffer from low thermal conductivity, insufficient thermal contact to the substrate, Joule heating and rf adsorption at low temperatures [46]. Another difficulty is that the temperature dependence of the resistance is not known *a priori*. It can be approximated by a power law or be described by a more sophisticated Mott-hopping model [75]. In our setups, the RuO_2 resistors saturate at temperatures between [5..10] mK. Nevertheless, this saturation limit is very low for RuO_2 and only made possible thanks to excellent electrical shielding and careful thermal anchoring.

To be independent of secondary thermometers, we employ a Fixed-Point Device (FPD) as a primary thermometer [46]. The superconducting transitions of different materials are detected by measuring the magnetic susceptibility. The used FPD features seven superconducting transitions between 3.3 K and 96 mK. The three lowest transitions (IrRh: 30 mK / Be: 21 mK / W: 15.5 mK) are smeared over a broad temperature range or not visible at all, potentially due to internal stress of the superconducting samples or residual magnetic flux [76].

A third type of commonly used thermometers are paramagnets containing elements with partially filled 3d or 4f orbitals. These thermometers utilize the temperature dependence of the magnetic sensitivity $\chi(T)$ which follows the Curie-Weiss law [46]

$$\chi(T) = \chi_0 + \frac{\lambda_C}{T - \Delta_W}\,, \tag{2.26}$$

where λ_C depicts the Curie constant and Δ_W the Weiss constant. Here, a temperature-independent background contribution to the susceptibility χ_0, which can result for example from wiring, was added to the Curie-Weiss equation. Δ_W depends on the shape of the sample, the symmetry of the crystal and the interactions between the magnetic moments [45]. At $T = \Delta_W$ the law predicts a singularity in χ. For typical susceptibility thermometers, $|\Delta_W| < 0.1\,\mathrm{mK}$. Related to the Weiss constant is the ordering temperature T_c, which represents another limitation for this law. The paramagnetic salt with the lowest $T_c \approx 2\,\mathrm{mK}$ is Cerium-Magnesium-Nitrate (CMN) [45]. By replacing a large fraction of Ce^{3+} by La^{3+} ions (LCMN), the magnetic interactions are weakened and thus T_c can be reduced by a factor of roughly 10 [46]. We use other secondary thermometers or the FPD to calibrate CMNs and LCMNs, where the measured values of the mutual inductances arising from the material's T-dependent susceptibility are plotted versus T^{-1}, resulting in a linear behavior for $\Delta_W = 0$, i.e. for a pure Curie law.

We observe a saturation at temperatures of $[1..3]\,\mathrm{mK}$ for all CMN and LCMN sensors used in both our setups. Because the warm-up behavior (linear in T^{-1}, see Eq. (2.27)) only appears after a few hours, depending on B_f, we infer that the NRs are much colder than the reading of the thermometers. While this saturation limit is expected for a CMN thermometer due to its $T_c \approx 2\,\mathrm{mK}$, the ordering temperature of LCMN is usually $[0.2..0.5]\,\mathrm{mK}$ [77]. At the same time, the saturation complicates the determination of Δ_W since its origin is unknown. A deviation from the Curie-Weiss behavior has been reported before at temperatures below 3 mK [78] and can be caused by heat release in the sensor, deficient thermal anchoring, Joule heating from the excitation current as well as the device architecture or fabrication. Since the saturation temperatures of the LCMNs vary between different cooldowns, we suspect that a hydration of the paramagnetic salt enhances the dipole-dipole interaction, which would result in a varying Δ_W [76].

To characterize the efficiency of our AND process, we use the time evolution of the nuclear temperature after AND depicted by Eq. (2.24). Using Eq. (2.22), we can

deduce an according expression for the electron temperatures. The warm-up of T_e as a function of time t at B_f under a certain $\dot{Q}_m$ is described by

$$T_e^{-1}(t) = T_{e,f}^{-1} - t\left(\frac{\lambda_n B_f^2}{\mu_0 \dot{Q}_m} + K\right)^{-1}. \tag{2.27}$$

This relation allows us to extract the electron temperature at the end of the demagnetization $T_{e,f}$ as well as $\dot{Q}_m$ by fitting a line to T_e^{-1} versus t in the regime where the thermometer is not saturated anymore (see appendix A) and thus shows the expected linear behavior [41]. Typically at $T_e \sim [30..80]\,\mathrm{mK}$, the heat leak is drained by the finite thermal conductance through the Al heat switch, leading to a temperature saturation. This approach can not be used for real-time temperature reading – temperature can only be determined as an extrapolation once the AND single-shot state is exhausted. An exemplary measurement using this formulation is presented in Fig. 8.4. The noise thermometer presented in chapter 7.2 allows us to measure temperatures down to $\sim 1\,\mathrm{mK}$, currently being limited by the experimental excess noise caused by electromagnetic interferences.

3 Metallic Coulomb Blockade Thermometry down to 10 mK and Below

L. Casparis, D. Maradan, A. C. Clark, C. P. Scheller,

K. K. Schwarzwälder, D. M. Zumbühl

Department of Physics, University of Basel, CH-4056 Basel, Switzerland

M. Meschke, J. P. Pekola

Low Temperature Laboratory (OVLL), Aalto University, 00076 Aalto, Finland

Abstract

We present an improved nuclear refrigerator reaching 0.3 mK, aimed at microkelvin nanoelectronic experiments, and use it to investigate metallic Coulomb blockade thermometers (CBTs) with various resistances R. The high-R devices cool to slightly lower T, consistent with better isolation from the noise environment, and exhibit electron-phonon cooling $\propto T^5$ and a residual heat-leak of 40 aW. In contrast, the low-R CBTs display cooling with a clearly weaker T-dependence, deviating from the electron-phonon mechanism. The CBTs agree excellently with the refrigerator temperature above 20 mK and reach a minimum-T of 7.5 $\pm$ 0.2 mK.

This chapter was published in *Rev. Sci. Instrum.* **83**, 083903 (2012).

3.1 Motivation

Advancing to even lower temperatures can open the door for the discovery of new physics: for example, submillikelvin temperatures in quantum transport experiments could lead to novel nuclear-spin physics [79, 80] in nanoscale semiconductor devices [3] or could facilitate the study of non-Abelian anyons, Majorana fermions and topological quantum computation in fractional quantum Hall samples [81, 82]. However, cooling of nanoscale devices below $T \sim 1\,\mathrm{mK}$ is a formidable challenge due to poor thermal contact as well as microwave and other heating, often resulting in device and/or electron temperatures raised well above the refrigerator temperature. Therefore, significant progress beyond the status quo in both cooling techniques and thermometry is necessary.

3.2 Strategy to Approach sub-mK Sample Temperatures

One approach to overcome these difficulties uses Ag sinters [41, 45, 55] to thermalize the sample wires [33], pioneered by the Florida group [7, 83]. Another approach – pursued by our Basel group [69] – is to use nuclear cooling [41, 45, 55] on the sample wires, with the potential to advance well into the microkelvin range. Thermometry in this regime [41, 45, 55] typically faces similar challenges as cooling nanostructures and is ideally integrated on-sample. Among numerous sensors [84], Coulomb blockade thermometers (CBTs) [85] are simple to use and self-calibrating yet offer high accuracy, demonstrated down to $\sim$20 mK [86]. Here, we present an improved nuclear refrigerator (NR) for cooling nanoelectronic samples and use it to investigate CBTs and their mechanisms of cooling.

3.2.1 Nuclear Refrigerator and Microwave Filtering Scheme

We employ a novel scheme for cooling electronic nanostructures into the microkelvin regime by thermalizing each sample wire directly to its own, separate nuclear refrig-

erator [69]. In this scheme, the sample cools efficienty through the highly conducting wires via electronic heat conduction, bypassing the phonon degree of freedom since it becomes inefficient for cooling at low T. A prototype of this refrigerator presented in Ref. [69] has been significantly improved in a second generation system, briefly outlined below and in Fig. 3.1. A network of 21 parallel NRs is mounted on a rigid tripod intended to minimize vibrational heating. Two separate 9 T magnets allow independent control of the NR and sample magnetic field.

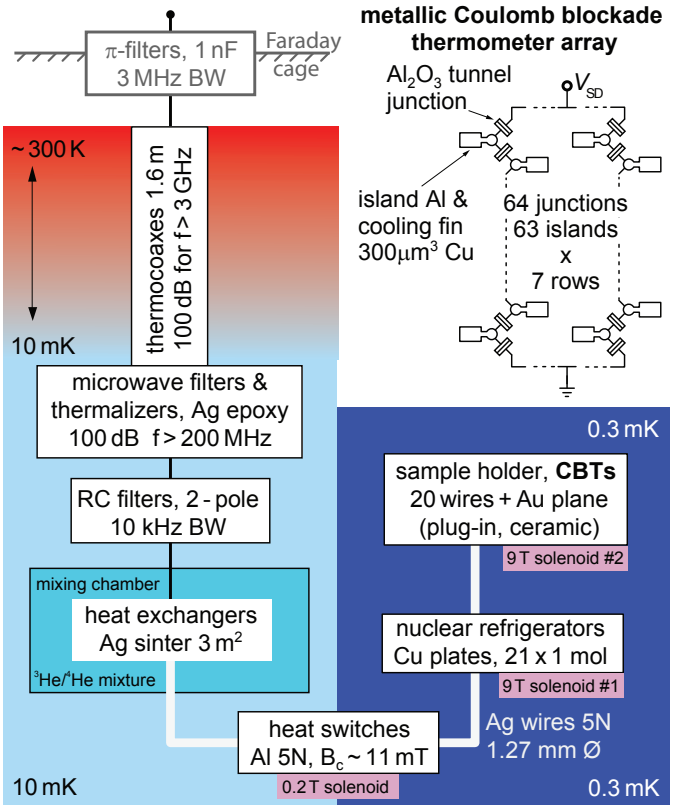

Figure 3.1: Layout of novel nanosample microkelvin refrigerator and CBT array. Radiation shields (not drawn) are attached to the still and cold plate ($\sim 50\,\mathrm{mK}$). The RC filters are $820\,\Omega\,/\,22\,\mathrm{nF}$ and $1.2\,\mathrm{k}\Omega\,/\,4.7\,\mathrm{nF}$. The 21 NR plates are $(32 \times 2.5 \times 90)\,\mathrm{mm}^3$ each, amounting to 64 g Cu per plate.

Several stages of thermalization and filtering are provided on each sample wire (see Fig. 3.1). After π-filter and thermocoax [66], each lead passes through a Ag-epoxy microwave filter [65], followed by an RC filter. Each wire then feeds into a Ag-sinter in the mixing chamber, emerging as a massive high-conductivity Ag wire. After Al

heat-switches with fused joints, each lead traverses a separate Cu-NR via spot-welded contacts, terminating in an easily-exchangeable chip carrier plugged into Au-plated pins which are spot welded to the Ag wires. Therefore, excellent thermal contact ($< 50\,\mathrm{m\Omega}$) is provided between the bonding pads and the parallel network of 21 Cu pieces – the micro kelvin bath and heart of the nuclear refrigerator – while maintaining electrical isolation of all wires from each other and from ground, as required for nanoelectronic measurements.

3.2.2 Performance of the Nuclear Refrigerators

The performance of the NRs is evaluated in a series of demagnetization runs. The temperature T_{Cu} of the Cu pieces is obtained using a standard technique [41, 45, 69]: after demagnetization, we apply power on heaters mounted on some of the NRs and evaluate the warm-up time-dependence $T_{Cu}(t)$ measured with Lanthanum Cerium Magnesium Nitrate (LCMN) thermometers above 2 mK. This allows us to determine both the temperature T_{Cu} of the Cu-NRs after demagnetization as well as a small field-offset. For each demagnetization run, the NRs are precooled to $T_i \sim 12\,\mathrm{mK}$ in a $B_i = 9\,\mathrm{T}$ magnetic field and then demagnetized to temperatures as low as $T_f \sim 0.3\,\mathrm{mK}$ after the field has been slowly ramped down to $T_f \sim 0.135\,\mathrm{T}$, giving efficiencies $(T_i/T_f)/(B_i/B_f) \gtrsim 60\%$. Reruns showed excellent repeatability, allowing us to chart T_{Cu} for various B_f. To determine T_{Cu} during the CBT experiments, we use the LCMN thermometers above 2 mK, warm-up curves at the lowest B_f and in-between, the pre-charted T_{Cu} values.

3.3 Electron Temperature Measurements

3.3.1 Sample Overview

The network with 21 NRs allows measurements of several CBTs (2-wire each). The CBT devices are Au-wire bonded and glued to the Au backplane of the chip carrier which is also cooled with a NR. Each CBT consists of 7 parallel rows of 64 Al/Al_2O_3

tunnel-junctions in series with an area of $2\,\mu m^2$ fabricated using e-beam lithography and shadow evaporation. The process used allows oxidation at elevated temperatures, giving junction resistances up to $1\,M\Omega\,/\,\mu m^2$. Each island extends into a large cooling fin made from Cu, since Cu gives excellent electron-phonon (EP) coupling. A small $B \sim 150\,mT$ is applied perpendicular to the sensor wafer to suppress the superconductivity of the Al. The differential conductance through a CBT sensor was measured with a standard lock-in technique adding a small AC excitation V_{AC} to a DC bias V_{SD}. Note that only 1/64 of the applied voltage drops across each junction and the sensor resistance is 64/7 times the junction resistance R_j, assuming identical junctions.

3.3.2 Performance for Different Sensors

We investigated CBTs with various R, see Fig. 3.2. Due to Coulomb blockade effects, the conductance around $V_{SD} = 0$ is suppressed below the large-bias conductance g_T. Both width and depth $\delta g = 1 - g(V_{SD} = 0)/g_T$ of the conductance dip are related to the CBT electron temperature T_{CBT}. To extract T_{CBT}, we perform fits (dashed curves) using a numerical model from Ref. [87]. We find excellent agreement between model and data (see Fig. 3.2). Independently, T_{CBT} can be obtained [87] from the conductance dip

$$\delta g = \frac{u}{6} - \frac{u^2}{60} + \frac{u^3}{630} \tag{3.1}$$

with $u = E_C/(k_B T_{\mathrm{CBT}})$ and charging energy E_C. We first extract E_C at high-T assuming $T_{Cu} = T_{\mathrm{CBT}}$ and then use this E_C to extract T_{CBT} from δg everywhere. While both methods produce very similar T_{CBT} (deviating slightly only at the lowest T), the δg approach makes no *a priori* assumptions about the cooling mechanism, allowing us an unbiased investigation, though now requiring high-T calibration against another thermometer. All T_{CBT} values given here are from the δg method.

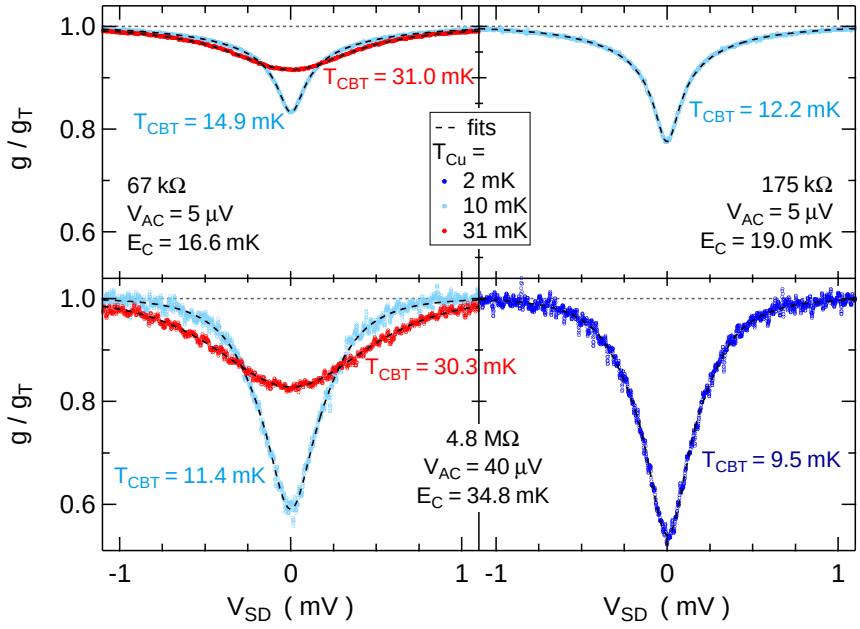

Figure 3.2: CBT normalized differential conductance g/g_T versus source-drain DC bias V_{SD} for various NR temperatures T_{Cu} as color-coded, with resulting T_{CBT} (δg method, see text) given adjacent to each trace. Data from a 67 kΩ, 175 kΩ and 4.8 MΩ CBT is shown. Dashed curves are fits to a model (see text). Note lower noise in low-R sensors due to larger resulting currents.

3.4 Cooling Mechanism

3.4.1 Theoretical Model Including EP and WF Cooling

The thermalization properties of T_{CBT} of the lowest and highest R CBTs are displayed in Fig. 3.3 for a wide range of T_{Cu} from 0.5 mK to 100 mK. As seen, excellent agreement is found between T_{CBT} and T_{Cu} at high temperatures, as expected. Further, T_{CBT} is seen to lie well above T_{Cu} at the lower temperatures (see Fig. 3.2 and 3.3), decoupling fully from T_{Cu} well below 10 mK. We note that V_{AC} was experimentally chosen to avoid self-heating. Also, the 4.8 MΩ sensor reaches lower temperatures than the other, lower impedance CBTs, consistent with better isolation from the environment, since the power dissipated is proportional to V_{env}^2/R_j, with environmental noise voltage V_{env}.

To model the CBT thermalization [87], we write down the heat flow $\dot{Q}_i$ onto a single island i with electron temperature T_i:

$$\dot{Q}_i = \frac{V_j^2}{R_j} + \sum_{\pm} \frac{\pi^2 k_B^2}{6e^2 R_j} \left(T_{i\pm1}^2 - T_i^2\right) - \Sigma\Omega \left(T_i^5 - T_p^5\right) + \dot{Q}_0 \,, \tag{3.2}$$

where $\dot{Q}_0$ is a parasitic heat leak and V_j is the voltage drop across the junction, appearing here in the Joule heating term. Σ is the Cu EP coupling constant, $\Omega = 300\,\mu\text{m}^3$ the island volume and T_p the phonon bath temperature assumed to be equal to T_{Cu}. This is well justified by the high thermal conductance between the NRs and bonding pads. Note that at $T \ll 1\,\text{K}$, the sample-to-Au-backplane interface resistance (Kapitza) is small compared to the EP coupling resistance [87]. Within this model, two cooling mechanisms are available: Wiedemann-Franz (WF, T^2 term) and EP cooling. Note the strong T^5 dependence of the EP term, ultimately rendering WF cooling dominant at sufficiently low T. Assuming one mechanism and simplifying to only one island gives a saturation curve

$$T_{\text{CBT}} = (T_S^p + T_{Cu}^p)^{1/p} \tag{3.3}$$

with a CBT saturation temperature T_S and an exponent p, corresponding to $p = 2$ for WF-electron cooling and $p = 5$ for EP cooling.

3.4.2 Measured Cooling Power Laws versus Theory

We study the mechanism of thermalization by fitting the saturation curve first to the $4.8\,\text{M}\Omega$ data. We find very good agreement, giving $p = 4.9 \pm 0.4$ (see Fig. 3.3), indicating that EP coupling presents the dominant cooling mechanism, limiting T_{CBT} to 9.2 mK even though $T_{Cu} = 0.75\,\text{mK}$. Using $\dot{Q}_0 = \Sigma\Omega T_{\text{CBT}}^5$, a small parasitic heat leak $\dot{Q}_0 = 40\,\text{aW}$ results for each island, with $\Sigma = 2 \cdot 10^9\,\text{W}\,\text{K}^{-5}\,\text{m}^{-3}$ from Ref. [87]. We speculate that $\dot{Q}_0$ could be caused by electrical noise heating such as microwave radiation, intrinsic residual heat release from materials used or other heat sources. Considering the high-R junctions and correspondingly weak WF cooling, it is not surprising that EP coupling is dominant here.

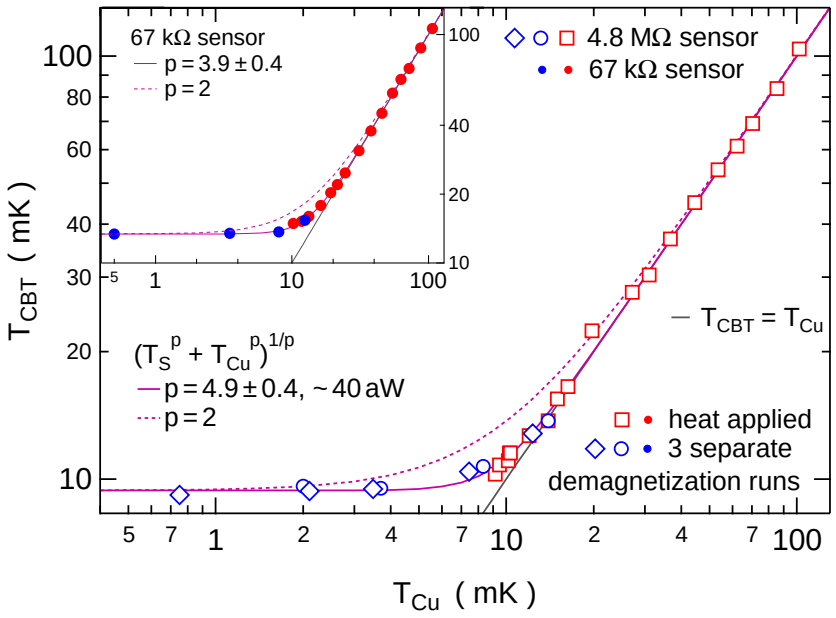

Figure 3.3: CBT electron temperature T_{CBT} versus NR temperature T_{Cu} for 4.8 MΩ (open markers) and 67 kΩ sensors (filled markers, same axes on *inset* as main figure). Below 10 mK, the data is obtained in three demagnetization sweeps (blue markers) with $B = 9\,\mathrm{T}$, 5 T, 2 T, 1 T and 0.4 T in a typical run, ramped at 1 T/h above 1 T and 0.5 T/h below. Error bars are about the size of the markers. Purple curves are T_{CBT} saturation curves (see text).

When analogously examining the low-R sensors, on the other hand, we find $p = 3.9 \pm 0.4$ and $T_S = 13.4\,\mathrm{mK}$ for the 67 kΩ sensor (see inset Fig. 3.3), and even $p = 2.7 \pm 0.2$ and $T_S = 6.9 \pm 0.1\,\mathrm{mK}$ for a 134 kΩ sensor (not shown) mounted on a conventional dilution refrigerator (base-$T \sim 5\,\mathrm{mK}$) with improved filtering and chip carrier. Note that T_S is the extrapolated $T_{Cu} = 0$ saturation temperature. The lowest T measured here was $7.5 \pm 0.2\,\mathrm{mK}$. These power-laws far below $p = 5$ indicate that EP cooling is no longer dominant but, rather, a more efficient mechanism $p < 5$ takes over at the lowest temperatures in the low-R sensors.

3.5 Summary

In summary, we have demonstrated operation of the NRs down to 0.3 mK while the CBTs cool as low as 7.5 mK. Though the high-R sensor is obviously cooled by EP cou-

pling, the low-R sensors, interestingly, appear to be entering a different cooling regime. However, the low-R sensors have slightly higher T_{CBT} given the same environment, consistent with stronger coupling to the environment. The lowest CBT temperatures are limited by the parasitic heat leak, which is drained by the cooling channels available.

To further improve the sensor performance, the cooling-fin volume can be increased or the heat leak can be reduced, potentially using improvements in microwave shielding and filtering, e.g. using on-chip capacitors, metal planes or alternative array designs. Such efforts will strongly enhance thermalization if a more efficient cooling mechanism is indeed present, since otherwise, in the EP regime, reducing $\dot{Q}_0$ by 5 orders of magnitude will only reduce T_{CBT} by a factor of ten.

An alternative avenue based on quantum dot CBTs, e.g. in GaAs, might also be rewarding, taking advantage of a much larger E_C and level spacing Δ. The resulting reduced sensitivity to the environment might allow a single dot to be used, rather than an array, cooling the reservoirs directly via the WF term, rather than through a long series of junctions.

Acknowledgement

We would like to thank R. Blaauwgeers, G. Frossati, R. P. Haley, G. R. Pickett, V. Shvarts, P. Skyba and A. de Waard for very useful discussions. This work was supported by the Swiss Nanoscience Institute (SNI), NCCR QSIT, Swiss NSF, ERC starting grant and EU-FP7 SOLID and MICROKELVIN.

4 GaAs Quantum Dot Thermometry Using Direct Transport and Charge Sensing

D. Maradan*, L. Casparis*, T.-M. Liu, D. E. F. Biesinger,
C. P. Scheller, D. M. Zumbühl
Department of Physics, University of Basel, CH-4056 Basel, Switzerland

J. D. Zimmerman, A. C. Gossard
Materials Department, University of California, Santa Barbara, CA 93106, USA

Abstract

We present measurements of the electron temperature using gate defined quantum dots formed in a GaAs 2D electron gas in both direct transport and charge sensing mode. Decent agreement with the refrigerator temperature was observed over a broad range of temperatures down to 10 mK. Upon cooling nuclear demagnetization stages integrated into the sample wires below 1 mK, the device electron temperature saturates, remaining close to 10 mK. The extreme sensitivity of the thermometer to its environment as well as electronic noise complicates temperature measurements but could potentially provide further insight into the device characteristics. We discuss thermal coupling mechanisms, address possible reasons for the temperature saturation and delineate the prospects of further reducing the device electron temperature.

* These authors contributed equally to this work.

This chapter was published in *J. Low Temp. Phys.* **175**, 784 (2014).

4.1 Introduction

Two-dimensional electron gases (2DEGs) are a versatile, widely-used experimental platform in low temperature solid state physics because of their nearly ideal two-dimensional nature and the possibility to confine electrons to almost arbitrary shapes using gate voltages. Groundbreaking experiments have been realized in these systems, including artificial atoms [88–90], the integer and fractional quantum Hall effect [18, 19] and spin qubits [3, 91]. In many experiments, the temperature of the 2DEG is much higher than the temperature T_{MC} of the dilution refrigerator mixing chamber due to various reasons, including poor thermal coupling and insufficient filtering. However, a wide range of phenomena contain small energy scales and are only accessible at very low temperatures. These include novel nuclear spin quantum phases in 2D [79, 80] and in interacting 1D conductors [4, 5] and multiple impurity [92] or multiple channel [93, 94] Kondo physics. Further, studies of fragile fractional quantum Hall states, including candidates for non-Abelian physics such as the $\nu = 5/2$ state [95], would benefit from low temperatures, possibly opening the doors for topological quantum computation [81].

To our knowledge, the lowest reliable temperature reported in a 2DEG is 4 mK [7, 33] in a fractional quantum Hall experiment, with sintered silver heat exchangers attached to the sample wires in a ^{3}He cell. In Ref. [7], a $PrNi_5$ demagnetization stage at 0.5 mK was used to cool the liquid ^{3}He, well below the 4 mK of the 2DEG sample. For quantum Hall samples loaded into a chip holder in vacuum, slightly higher temperatures [9..13] mK were reported [24, 34, 96]. Interestingly, in Ref. [24] (supplementary), the refrigerator base temperature was below 6 mK and the temperature measured with a Coulomb blockaded quantum dot was 16 ± 3 mK. The lowest GaAs quantum dot temperature measurement reported is 12 mK [35, 36], as far as we know.

We note that apart from noise measurements [96], electron temperature measurements in the (fractional) quantum Hall regime are of rather qualitative nature, usually lacking

a well-known temperature dependent effect to extract temperature from. Instead, some temperature dependent feature, typically a longitudinal resistance peak [7, 24, 33], is used, assuming a specific temperature dependence (e.g. linear) – resulting in estimates of temperature, rather than absolute temperature values. A quantum dot thermometer, on the other hand, is in principle a primary thermometer capable of reading absolute temperatures [88]. However, compared to quantum Hall samples, a quantum dot device operates at significantly larger resistance (typically $\gtrsim 1\,\mathrm{M\Omega}$). Thus, essentially the entire voltage drops over the dot, presumably making it more susceptible to electronic noise.

For any device electron thermometer, it is very instructive to compare the electron temperature with a suitable calibrated refrigerator thermometer over a broad temperature range. Ideally, both thermometers should agree very well, demonstrating effective operation of the device thermometer – in a much more convincing way than agreement at any single, isolated temperature. In addition, at the lowest refrigerator temperatures, often a saturation of the device temperature becomes apparent, either due to improper thermometer operation or insufficient device thermalization (or both). The functional form of the deviation of the device temperature from the refrigerator temperature in principle contains important information about the device cooling mechanism [97], if the thermometry is accurate enough and functioning properly. Previous reports have shown quantum dot thermometers to agree well with the refrigerator thermometer over a broad range of rather high temperatures $T \gtrsim 100\,\mathrm{mK}$ [98–100], with the best reaching down to about 50 mK [36, 58, 101–103] – but not to lower temperatures.

These examples indicate that cooling of a 2DEG embedded in a semiconductor such as e.g. GaAs is a difficult task. The main reason is the weakening of the electron-phonon interaction in the 2DEG $\propto T^5$ [7, 104, 105] at low temperatures. Therefore, at very low temperature, the system benefits from cooling through the conduction electrons (Wiedemann-Franz mechanism, $\propto T^2$ [45, 106]), where heat transfer is mediated through the electrical contact to the sample. For typical semiconductor devices with

large contact resistances, this comparably weak coupling makes the sample vulnerable to heat leaks, e.g. high frequency radiation or dissipative heating. Additionally, the weakening of the electron-phonon interaction significantly complicates the thermal coupling of the insulated sample wires to the coldest part of the refrigerator.

Recently, we have proposed a way to overcome these limitations by integrating a copper nuclear refrigerator into each of the electrical sample wires connected to an electronic transport sample, providing efficient thermal contact to a bath at low mK or microkelvin temperature [69]. For efficient precooling of the nuclear refrigerators as well as for regular dilution refrigerator operation, every sample wire is connected to a sintered silver heat exchanger located in the plastic mixing chamber (facilitating superfluid leak-tight feedthroughs) of the dilution refrigerator with a base temperature of 9 mK. Further, to minimize the effect of high-frequency radiation, all electrical lines are filtered extensively using thermocoax cables, cryogenic Ag-epoxy microwave filters [65] and double-stage RC filters of bandwidth 30 kHz. The measurement setup is described in detail in reference [97]. In semiconductor samples such as GaAs 2DEGs, the ohmic contacts will probably present the largest electrical and thermal impedance in this cooling scheme.

4.2 Quantum Dot Thermometry

Gate defined GaAs quantum dots in deep Coulomb blockade are used as a thermometer directly probing the electron temperature T in the surrounding 2DEG by measuring the thermal smearing of the Fermi edge [88]. As shown in Fig. 4.1(a), the quantum dot is coupled to two electron reservoirs via left and right tunnel barriers with tunnel rates Γ_L and Γ_R. In the symmetric case $\Gamma_L = \Gamma_R = \Gamma$, the direct current through the quantum dot is approximated by $I_{\mathrm{DC}} = e\Gamma/2$ assuming sequential tunneling, with e the electron charge. In the temperature broadened Coulomb blockade regime ($h\Gamma \ll k_B T$, with Boltzmann constant k_B and Planck constant h), the narrow dot level with broadening $\sim \Gamma$ acts as a variable energy spectrometer which can resolve and directly map the

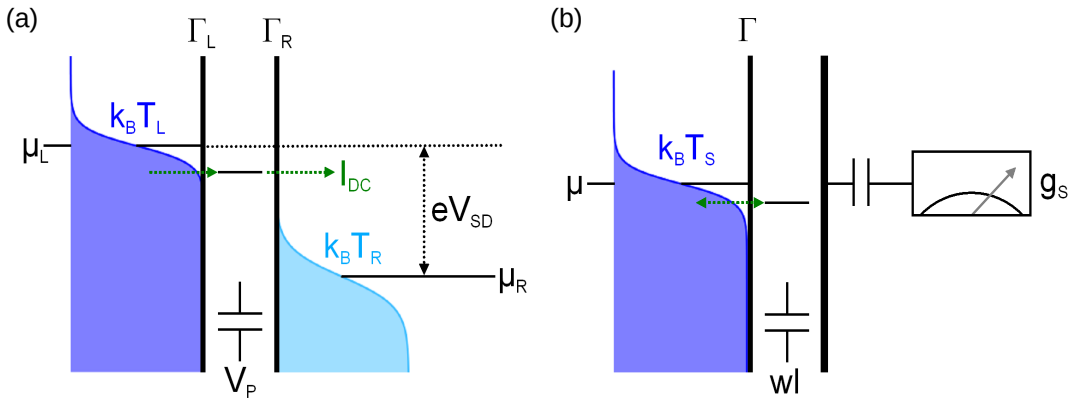

Figure 4.1: (a) Schematic for a temperature measurement using a single quantum dot. Low tunnel rates to the left and right reservoir, Γ_L and Γ_R respectively, result in an energetically sharp quantum dot level which can be tuned with the plunger gate V_P. By sweeping the dot level through the source-drain window eV_{SD}, given by the difference in chemical potentials $\mu_L - \mu_R$, the temperature of each reservoir can be extracted individually; the thermally smeared Fermi-Dirac distributions ($\propto k_B T$, here $T_R > T_L$) are mapped with the measured current I_{DC}. (b) Working principle for the charge sensing measurement: the dot level can be swept through the Fermi level at chemical potential μ using the topgate voltage wl. The average occupation probability, which again reflects the Fermi-Dirac distribution (i.e. temperature T_S) in the double dot reservoir, is probed by the conductance g_s through a charge sensing quantum dot capacitively coupled to the dot. For details see text.

Fermi-Dirac (FD) distribution in the current through the dot. The energy of the spectrometer can be tuned by capacitively shifting the dot energy level with a gate, e.g. the plunger gate at voltage V_P. With a sufficiently large DC source-drain bias $V_{\mathrm{SD}} \gg k_B T/e$, the chemical potential of source and drain reservoirs can be individually resolved, separately giving the distribution functions of each reservoir when sweeping the plunger gate voltage V_P through both source and drain chemical potentials.

To stay in the single level transport regime, the bias V_{SD} has to be small compared to the excited state energy Δ. To obtain the temperature from each distribution function, the gate lever arm α is required for the conversion from gate voltage to energy. The separation ΔV_P in gate voltage between the inflection points of the two FD distributions can be taken from the plunger gate sweep $I_{\mathrm{DC}}(V_P)$ at a fixed, known bias V_{SD}. This measurement gives the lever arm $\alpha = eV_{\mathrm{SD}}/\Delta V_P$ without additional measurements and delivers the temperatures T_L and T_R of the left and right reservoir, respectively, from a

single $I_{\mathrm{DC}}(V_P)$ sweep. This allows a temperature measurement without calibration by another thermometer, thus constituting a primary thermometer. As an alternative, the differential conductance through the dot can be measured using a small AC voltage, resulting in the derivative of the FD function [88].

We note that here, the device is operated in a highly non-linear regime where the dot current I_{DC} depends only on the tunneling rate Γ but is – to lowest order – independent of the applied bias $k_BT \ll V_{\mathrm{SD}} \ll \Delta$ once the dot level is well within the transport window spanned by source and drain chemical potentials. However, the electrons traversing the dot are injected at a high energy $V_{\mathrm{SD}} \gg k_BT$ into the reservoir with the lower chemical potential. These hot electrons will relax their energy and thereby cause heating in the 2DEG reservoir. The currents and biases used here are rather small, typically giving heating powers $\sim I_{\mathrm{DC}}V_{\mathrm{SD}}$ below 1 fW. Nevertheless, this heat will need to be removed, e.g. through the ohmic contacts or the phonon degree of freedom. We experimentally choose the bias V_{SD} small enough to avoid measurable heating.

For ultra-low temperatures, one critical aspect of the quantum dot thermometer is the requirement to have a dot level much sharper than the FD distribution to be probed and resolved. The broadening of the dot level is given by lifetime broadening: the finite time an electron spends on the dot, defined by its escape rate $\sim \Gamma$, introduces an uncertainty on its energy through the time-energy Heisenberg uncertainty principle. In gate defined dots, the tunneling rate Γ can be tuned widely over many orders of magnitude with gate voltages, affording broad flexibility. While Γ can easily be made sufficiently small to satisfy $h\Gamma \ll k_BT$ even at the lowest temperatures, reduced Γ also suppresses the dot current $I_{\mathrm{DC}} \sim e\Gamma/2$. Taking $2h\Gamma = k_BT$, an upper bound on the dot current of $I \sim 1\,\mathrm{pA}\cdot\vartheta$ results, where ϑ is the temperature in mK. Thus, to be clearly in the temperature broadened regime, currents far below these upper bounds are required, setting a practical limit of order of 10 mK as the lowest temperature that can be measured with the current setup.

An integrated charge sensor directly adjacent to the quantum dot [107, 108] makes it

possible to overcome this limitation: a measurement of the average dot charge occupation while sweeping the dot level through a charge transition [109] reflects the FD distribution under similar conditions as described before. However, the dot-reservoir tunneling rate Γ can now be made essentially arbitrarily small, ensuring $h\Gamma \ll k_B T$ even for temperatures well below 1 mK. This is possible because the size of the charge sensor signal is nearly independent of Γ and the charge sensor remains operational for arbitrarily small Γ. The distribution function is conveniently measured when the dot tunneling is fast compared to the data acquisition rate, avoiding complications due to real time detection of single electron tunneling. The current through the charge sensor still gives rise to phonon or photon emission [110] and generally causes heating, analogous to a current flowing directly through the dot as discussed above. However, the sensor and its reservoirs can be electrically isolated and spatially separated somewhat from the dot, reducing heat leaks and coupling strength [111] and improving the situation compared to a direct current through the quantum dot. Nevertheless, the sensor biasing will need to be experimentally chosen to minimize such heating effects.

Similar thermometry can also be performed in a double quantum dot configuration, where charge transitions involving a reservoir can be used to measure the FD distribution and the corresponding temperature, see Fig. 4.1(b). The relevant double dot lever arm can be extracted again from finite bias measurements [112] or can be calibrated at elevated temperatures where it is safe to assume $T_{\mathrm{MC}} = T_{L,R}$ with the temperature of the left and right reservoir $T_{L,R}$, respectively. It is worth noting that in a double dot, the thermal smearing of the reservoirs can be essentially eliminated when studying internal transitions such as inter-dot tunneling, allowing measurements with a resolution much better than the reservoir temperature [112]. Nevertheless, internal double dot transitions can also be used for reservoir thermometry depending on the dot configuration [109]. Similarly, in optically active semiconductor quantum dots, the reservoir temperature can be irrelevant and the optical line width is limited by the lifetime and/or other noise sources such as semiconductor charge instabilities or nuclear

spin noise [113].

Interestingly, the energy levels of the double dot can easily be configured (e.g. sufficiently far away from the triple points or bias triangles) so that no net current can flow through the double dot even at some finite bias (here always assuming sequential tunneling only), avoiding dissipative heating originating from the double dot altogether. Despite the absence of current flow, the system can still easily be probed with a charge sensor and the reservoir temperature can be extracted as described above. A similar situation can also be exploited in a single dot with one barrier tuned to be very opaque [114]. The biasing of the charge sensor nevertheless still dissipates energy, as already described.

4.2.1 Thermometry with Direct Transport

The quantum dots were fabricated with standard UV and ebeam lithography and evaporation of Ti/Au depletion gates. The single quantum dot (SQD) layout, see inset of Fig. 4.2(b), was adapted from Ref. [115], giving access to the few electron regime in transport measurements. The 2DEG is formed at a single AlGaAs/GaAs interface, located 110 nm below the surface, with charge carrier density $n = 2.8 \cdot 10^{11}\,\mathrm{cm}^{-2}$ and mobility $\mu = 2.8 \cdot 10^{5}\,\mathrm{cm}^{2}\,\mathrm{V}^{-1}\,\mathrm{s}^{-1}$. This wafer was chosen because of excellent charge stability. The devices were cooled down without positive voltage bias on the gates. The ohmic contacts are non-magnetic, made from AuGe/Pt, and optimized for minimal contact resistances, typically $\lesssim 100\,\Omega$. The direct current I_{DC} through the dot was measured with a 3 Hz low-pass filter.

We now show how the reservoir temperatures T_L and T_R can be extracted from a measurement of the current I_{DC} through the dot at finite applied bias V_{SD} as a function of the plunger gate voltage V_P, as shown in Fig. 4.2(a). The plunger gate V_P allows us to shift the energy of the dot level through both source and drain chemical potentials without significantly changing the reservoir tunneling rates for a small change of V_P: more negative V_P capacitively shifts the dot level to higher energy. A finite current

flows through the dot when the dot energy level is located within the transport window, see Fig. 4.1(a). Otherwise, no current can flow, either due to a lack of filled electron states when the dot energy is above the higher chemical potential reservoir, or due to a lack of empty states the dot electron can tunnel into when the dot energy is below the lower chemical potential reservoir. The transitions between zero and finite current I_{DC} each reflect the distribution function of the respective reservoir and can be fit by a FD function of the form

$$I_{FD}(V_P) = I_1 \left[\exp\left(\frac{\alpha(V_P - V_{P0})}{k_B T_{L,R}} \right) + 1 \right]^{-1} + I_0, \tag{4.1}$$

with step height I_1, offset current I_0 and plunger gate offset V_{P0}. For a given step height I_1 and lever arm α, the temperature is essentially given by the slope of the transition, where lower temperature corresponds to a steeper, sharper curve. A rising (falling) step is obtained by the choice of the relative sign of I_0 and I_1. We note that this fit function will only apply in a rather narrow window of energy (i.e. plunger gate voltage) around the transition, since other effects not captured by the FD function alone can also play a role, such as local density of states variations due to the finite size lead reservoirs. The FD function gives high quality fits to the data within the measurement noise, see Fig. 4.2(a), and delivers separate temperatures $T_{L,R}$ for the left and right reservoirs, respectively. The right reservoir was connected to the current preamplifier and gives slightly higher temperatures $T_R > T_L$, see Fig. 4.2(a). Swapping the current preamplifier to the other reservoir inverts the situation. Upon increasing T_{MC}, we have observed better agreement with T_L than with T_R, thus we will focus on T_L. The weak dependence of dot current on V_P in the high current state can arise e.g. due to variations in the local density of states in the leads, but is not part of the transition region fit by the FD function. The DC bias voltage was reduced until no effects on the extracted temperatures were observed, typically $V_{\mathrm{SD}} < 100\,\mu\mathrm{V}$ at the lowest temperatures – still allowing to clearly separate the two flanks.

Despite significant noise on the I_{DC} data, the error-bars on the temperatures extracted

from the individual FD fits are rather small $\lesssim 10\,\%$, see Fig. 4.2(a), plus $\lesssim 10\,\%$ error from uncertainty of the lever arm α. A further uncertainty (typically about $\lesssim 20\%$) becomes apparent when the fits are performed over a large number (of order 10) of repeated current traces under nominally identical conditions, see Fig. 4.2(b). This uncertainty is due to charge instabilities and resulting random telegraph noise – occasionally directly identifiable in the data as a discrete switch – as well as slow drifts in the 2DEG material and quantum dots, or external influences. Semiconductor charge noise is known for a long time and has been studied extensively, see e.g. Refs. [113, 116, 117] and references therein. We note that the sensitivity to such disturbances becomes more pronounced at lower temperature, already requiring an energy jitter of much less than $\sim 1\,\mu$eV at 10 mK – a quite remarkable charge stability [113]. The severity of such charge noise depends sensitively on the detailed dot gate voltage configuration as well as the wafer material and fabrication procedure and can become negligible at elevated temperatures due to increased thermal broadening. Current traces with obviously apparent switching events are not included in the ensemble of traces used to extract temperature. Nevertheless, charge switching is not always directly identifiable and the fluctuating temperatures extracted from the FD fits upon repeating the measurement are predominantly due to charge noise. A switch occurring during the scan at the transition is the only obvious source we are aware of that could lead to both a narrowing or a broadening of the FD distribution, resulting in artificially fluctuating temperatures extracted from the FD fits, as seen in the experiment.

Due to the sizable charge noise, we cannot use an individual temperature measurement as in Fig. 4.2(a), but rather have to gather statistics in order to obtain a more reliable measure of temperature. In Figure 4.2(b), we extract the average temperature of the left reservoir $\langle T_L \rangle$ measured with the quantum dot at fixed configuration for several refrigerator mixing chamber temperatures T_{MC}, measured with a Cerium-Magnesium-Nitrate (CMN) thermometer. The CMN thermometer was calibrated using a standard fixed-point device with six superconducting transitions between 1.2 K and

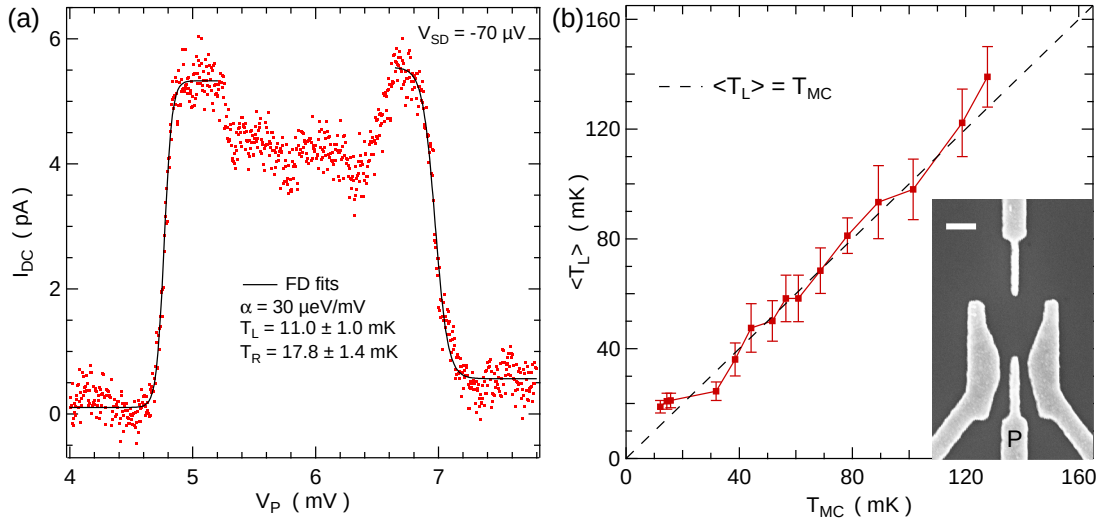

Figure 4.2: (a) DC current I_{DC} through the single quantum dot as a function of plunger gate voltage V_P at refrigerator temperature $T_{\mathrm{MC}} = 9\,\mathrm{mK}$, showing a high current region (dot level between source and drain chemical potential) and a low current region (dot level outside source-drain window). These regions are separated by the Fermi-Dirac distributions in each reservoir, separately giving T_L and T_R from Fermi-Dirac fits (solid curves). The error bars shown here are the uncertainties from the FD fits only. An additional uncertainty of $\lesssim 10\,\%$ arises from the error on the lever arm. The right reservoir is connected to the current preamplifier and slightly warmer than the left reservoir. (b) Average temperature $\langle T_L \rangle$ obtained over several repeated T_L measurements, as a function of refrigerator temperature T_{MC}. The dot configuration was not changed during this temperature sweep. The error bars shown are the statistical errors from repetition of the T_L measurement. An additional uncertainty of $\lesssim 10\%$ on $\langle T_L \rangle$ needs to be added to the error bars shown, arising from the uncertainty of the lever arm. *Inset:* SEM picture of a device similar to the one measured (P: plunger gate, scale bar: 200 nm).

96 mK, giving excellent agreement between fixed-point device and CMN. A calibrated RuO_2 resistor (also in very good agreement with the fixed points) was used to extend the CMN calibration range to lower temperatures, giving excellent agreement with the CMN to below 20 mK. Almost identical CMN temperatures are obtained in the range from [10..200] mK, regardless of whether a Curie law or a Curie-Weiss law is used to calibrate the CMN thermometer [45].

The standard deviation resulting from the repeated current traces is used to give the error bars on $\langle T_L \rangle$ in Fig. 4.2(b). The lever arm uncertainty $\lesssim 10\%$ is in addition to the error bars shown. As seen in Fig. 4.2(b), we find decent agreement between $\langle T_L \rangle$ and T_{MC} within the error bars over the temperature range from ~ 20 mK to ~ 130 mK. At the lowest temperatures, however, $\langle T_L \rangle$ appears to saturate at ~ 20 mK for the particular gate configuration used for this temperature sweep. When the measurement is further optimized and the tunnel rates are decreased a bit more (trading off current signal amplitude), the lowest temperature we extract in direct current through the dot is $\langle T_L \rangle = 11 \pm 3$ mK (including all errors) averaged over several traces similar to the data shown in Fig. 4.2(a). This is within the error bars of the base temperature $T_{\mathrm{MC}} = 9$ mK. Given agreement between $\langle T_L \rangle$ and T_{MC} over a wide temperature range, we can be confident that the sample is well thermalized and the dot thermometer is properly working, reading a reliable temperature despite charge noise.

4.2.2 Thermometry with Charge Sensing

We now turn to thermometry with a charge sensor adjacent to a double quantum dot device. The design of the device was adapted from Ref. [118], see inset of Fig. 4.3(a), employing quantum dots as very sensitive charge detectors, directly adjacent on either side of the double dot. Here, we focus on data from one of the sensors since the other sensor gave very similar results. A GaAs 2DEG material very similar to the wafer used for the single dots was used, again experimentally tested to exhibit excellent charge stability. The differential conductance $g_s = dI/dV$ of the charge sensing quantum dot

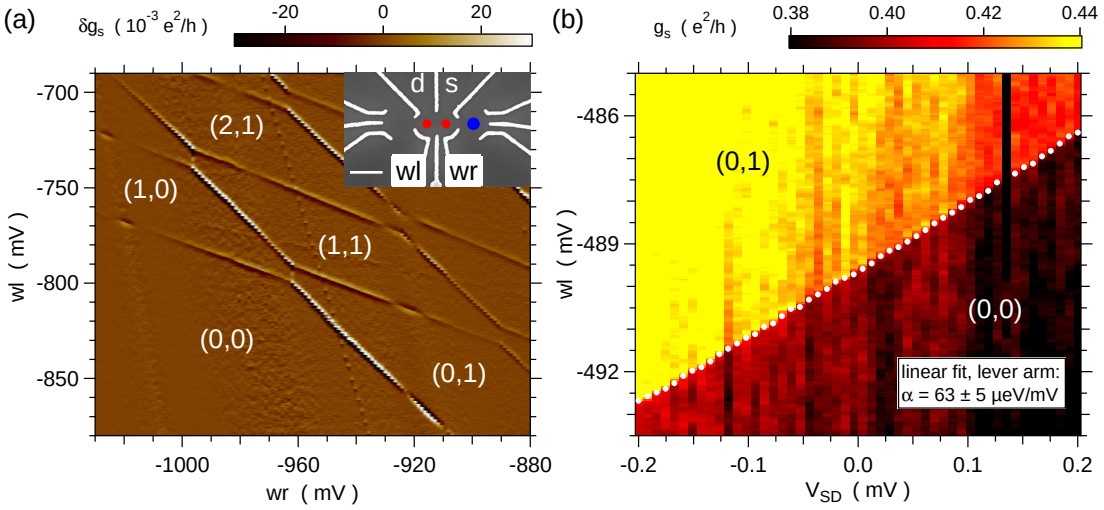

Figure 4.3: (a) Change in differential conductance δg_s of the sensor on the right side measured as a function of the voltage on the left wall wl and right wall wr of the double dot. The average of each vertical trace was subtracted to improve visibility. The charge stability diagram shows the honeycomb structure typical of a double dot. The absolute electron occupation (n,m) is labeled, indicating the charge state in the left and right dot, respectively. *Inset:* SEM picture of a device similar to the one measured (d/s: drain/source, scale bar: 400 nm, red dots: DQD, blue dot: charge sensing quantum dot). The colored dots refer to the estimated positions but not the actual sizes of the quantum dots. (b) Sensor differential conductance g_s as a function of wl and V_{SD} around the (0,0) to (0,1) transition, allowing extraction of the lever arm α, see text.

was measured with standard analog lock-in technique with an AC bias voltage $\leq 2\,\mu\mathrm{V}$. The sensor bias voltage was carefully experimentally restricted to avoid excess heating. The voltage and current noise of the measurement setup was carefully monitored and minimized, with optimal rms values of 0.5 µV and 50 fA, respectively.

The sensitivity of the charge sensor can be defined as $2|g_1 - g_2|/(g_1 + g_2) = |\Delta g|/g_{\mathrm{avg}}$ with the conductance values g_1 and g_2 corresponding to the charge states before and after the transition and $g_{\mathrm{avg}} = (g_1 + g_2)/2$. The charge sensor was operated in the lifetime broadened regime, tuned on a steep slope of a Coulomb blockade peak, giving excellent sensitivities of up to 100%. This is clearly superior to typical quantum point contact charge sensors, as previously reported [118]. Even better sensitivities could be achieved when tuning the sensor dot into the temperature broadened regime, where much narrower, sharp peaks result. However, staying on such a sharp peak becomes

experimentally difficult due to parasitic capacitive coupling between double dot gates and the sensor dot. Once the sensor is shifted to a region where the slope is very small (e.g. a Coulomb blockade valley with nearly vanishing conductance), the charge sensitivity is lost. Already in the lifetime broadened sensor regime used here, changes on the double dot gate voltages needed to be carefully compensated on the plunger gate of the sensor dot in order to maintain charge sensitivity.

The double dot charge stability diagram, as measured with the charge sensor, is shown in Fig. 4.3(a) as a function of gate voltage on the left wall wl and right wall wr of the double dot, as labeled in the inset. The typical honeycomb pattern as expected for a double dot [112] is observed. Each dot can be emptied of all electrons (bottom left), as evidenced by the absence of further charge transition lines in the diagram at more negative gate voltages. This allows us to label the double dot charge state (n,m), indicating the absolute electron occupation in the left and right dot, respectively. A couple of additional weak charge transitions are also appearing with slopes deviating from those occurring in the honeycomb of the double dot, presumably due to some nearby charge traps in the semiconductor. These are also related to the charge noise as seen in the temperature measurements.

The reservoir temperature can again be extracted, here from the charge sensor signal with analogous FD fits to any of the charge transitions in the honeycomb involving one of the reservoirs. The data are fitted using equation (4.1) by replacing currents I with sensor conductances g_s as well as V_P and V_{P0} with wl and wl0, respectively. As before, the corresponding lever arm is required for the conversion from gate voltage to energy and is extracted from measurements at high enough temperatures where double dot reservoir temperature T_S measured with the sensor is equal to T_{MC}. Bias triangles were not accessible in the regime the double dot was operated here due to tunnel rate asymmetries. We note that the inter-dot tunnel rate was tuned to be very small for the temperature measurements, with the double dot operated in a gate voltage configuration different from the one shown in Fig. 4.3(a).

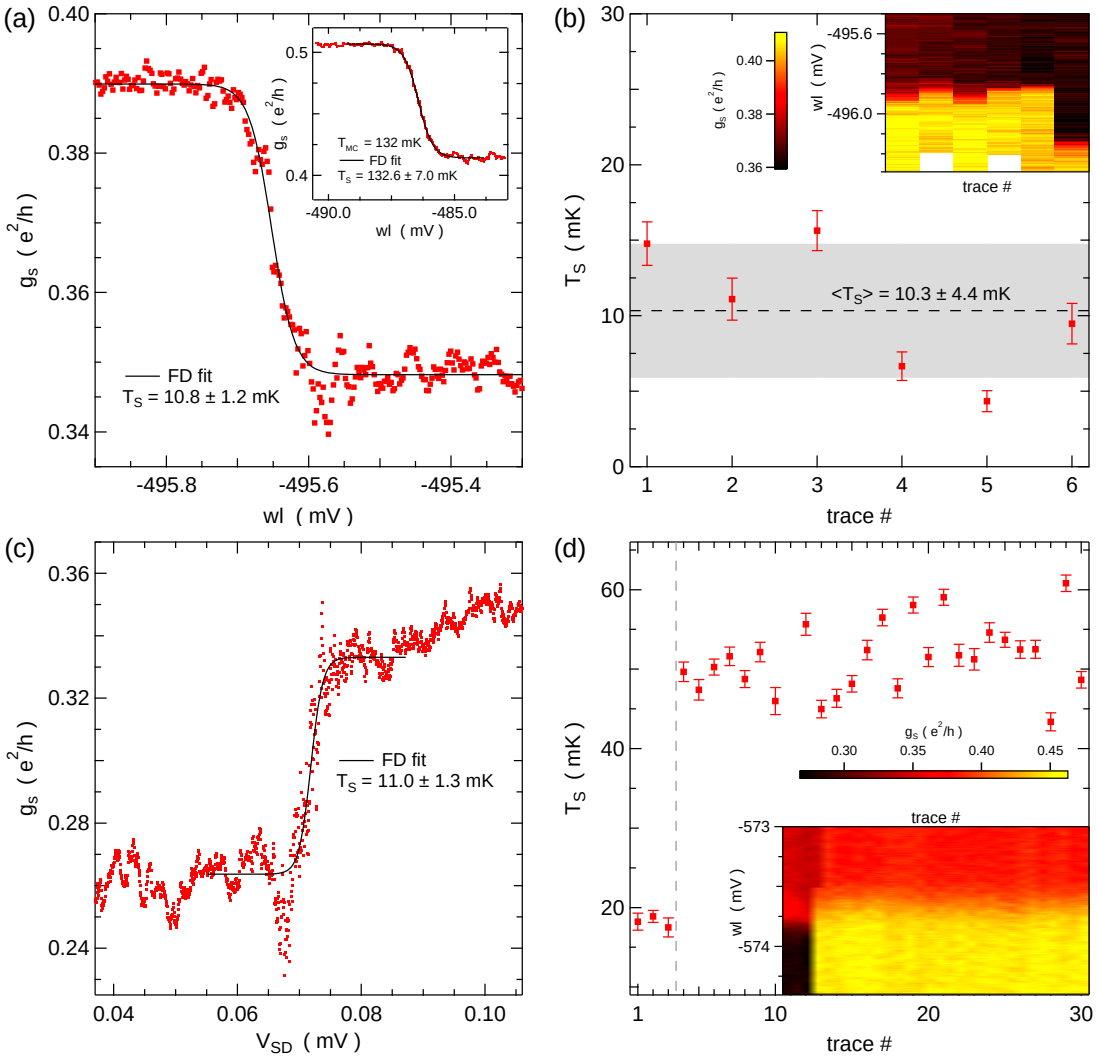

Figure 4.4: (a) Sensor differential conductance g_s (sensor dot on the right side) as a function of gate voltage wl at $T_{\mathrm{MC}} = 9\,\mathrm{mK}$, showing the transition from the (0,0) to (0,1) charge state. The reservoir temperature T_S is extracted from a FD fit (black curve) to sensor data, as indicated. *Inset:* Similar measurement with corresponding fit at $T_{\mathrm{MC}} = 132\,\mathrm{mK}$ showing $132.6 \pm 7.0\,\mathrm{mK}$. (b) Series of repeated T_S measurements in the same dot configuration with an average temperature $\langle T_S \rangle = 10.3 \pm 4.4\,\mathrm{mK}$ (dashed line: average, gray shaded area: standard deviation). *Inset:* Corresponding sensor conductance g_s as a function of gate voltage V_{wl} versus trace number. (c) Sensor conductance g_s of the right charge sensor as a function of V_{SD} at the transition from (0,0) to (0,1), with FD fit (black curve) and extracted temperature (see text) as labeled. (d) Reservoir temperature T_S extracted with the sensor from several repeated wl sweeps (see *inset*) versus trace number, showing an abrupt change of the electronic dot configuration after three sweeps, which increases the temperature reading from 18 mK to 52 mK. The systematic lever arm error of $\lesssim 8\%$ is to be added to all error bars here in (a)-(d).

Alternatively, the same charge transition can be followed for various double dot source-drain voltages V_{SD} applied to the reservoir involved in the transition, as shown in Fig. 4.3(b). Due to a finite capacitance of this reservoir to the dot, this gives an upper bound for the lever arm and the extracted temperature. However, the lever arm extracted at high temperature turns out to be the same as the upper bound (within the error bars of 10%), thus indicating that the reservoir-dot capacitance is small compared to the total dot capacitance for the configurations used in our device – at least at the very low tunnel rates utilized here. Hence, the slope of the charge transition line in the wl-V_{SD} plot gives the inverse of the lever arm. The lever arm error of $\lesssim 10\%$ needs to be added to all temperatures appearing in this section (unless noted otherwise) as a systematic rather than fluctuating error, i.e. affecting all temperatures in the same way. All temperature measurements shown here were carried out at the transition from (0,0) to (0,1), although similar results were obtained for other transitions.

Figure 4.4(a) shows a charge sensor measurement through the (0,0)-(0,1) transition and a FD fit at $T_{\mathrm{MC}} = 9\,\mathrm{mK}$, resulting in $T_S = 10.8 \pm 1.2\,\mathrm{mK}$. While the sensor measurements give very good agreement with the FD fits at elevated temperatures (see Fig. 4.4(a) inset, giving $T_S = 132.6 \pm 7.0\,\mathrm{mK}$ at $T_{\mathrm{MC}} = 132\,\mathrm{mK}$) over a broad temperature range, the charge sensor temperature measurement again becomes more difficult at the lowest temperatures. The inset of Fig. 4.4(b) shows the sensor signal for the same charge transition repeated a few times under identical conditions. Both the position and width of the transition is seen to fluctuate as a function of time, resulting in fluctuating T_S extracted with the FD fit, see Fig. 4.4(b), similar as described for temperature measurements via current through the dot. The error bars shown here (and also in Fig. 4.4(d)) are from the FD fit only. In addition, the configuration of the sensor can also affect the extracted temperatures, typically resulting in elevated temperatures for stronger sensor–double dot coupling. Thus, at lower temperature, smaller sensor step heights are required, making fitting more difficult. As before, curves displaying obvious switching events are not considered for determining temperature.

We can also use the double dot source-drain voltage V_{SD} instead of gate voltage to drive the charge transition and directly obtain a temperature value without needing a lever arm, since the reservoir–dot capacitance is small here, as previously discussed. In this way, we obtain an upper bound on the reservoir temperature which here is close (within 10%) to the actual temperature. Such a V_{SD} charge transition measurement is illustrated in Fig. 4.4(c), again for the (0,0)-(0,1) transition, and gives a very similar temperature as obtained from the gate sweep. The undershoot before and the overshoot after the rising edge has been observed in several measurement curves at the lowest temperatures, both by sweeping V_{SD} or a gate, though it is not seen in some other traces, e.g. Fig. 4.4(a). These features are only seen for certain gate voltage configurations and their origin is not currently understood.

The extreme sensitivity of the charge transition to the electrostatic environment is demonstrated in Fig. 4.4(d). While scanning the same transition 30 times, an abrupt change in the charge configuration during the fourth scan has altered the charge sensor conductance considerably, even inverting the sign of the sensor response to the dot charge transition. This switching event caused the apparent FD fit temperature to change from 18 mK to 52 mK. While the sensor conductance and double dot configuration can be strongly altered by a local charge rearrangement, the temperature of the large reservoirs was most certainly not affected by this single switching event. Thus, the lower temperature 18 mK reflects the reservoir temperature both before and after the switching event, while the higher temperature is artificially elevated due to improper dot/sensor configuration. Scanning charge transitions different from (0,0) to (0,1) revealed similar temperatures but also suffered from the same problems with charge instabilities.

4.3 Discussion

After considerable experimental efforts due to the pronounced sensitivity to electronic noise and device charge instabilities, we approach mixing chamber base temperature

with both methods, direct transport and charge sensing. By using the nuclear refrigerator ($T_{\mathrm{NR}} < 1\,\mathrm{mK}$ [97]), no further reduction of the electron temperature was observed, in contrast to measurements with other thermometers mounted in the same refrigerator in subsequent cool downs. In the direct transport measurements, we might suspect lifetime broadening of the quantum dot level as a limiting factor. But the temperatures obtained with the charge sensor are not evidently lower than the temperatures measured in direct transport, despite much lower dot tunneling rates.

In direct transport, dissipative heating from the voltage drop over the dot will eventually become significant at sufficiently low T. Estimates of the electron temperature T assuming dominant Wiedemann-Franz cooling, an ohmic contact resistance of $100\,\Omega$, $V_{\mathrm{SD}} = 100\,\mu\mathrm{V}$ and a current of $8\,\mathrm{pA}$ ($\Gamma/2 = 50\,\mathrm{MHz}$) indicate that the temperature is only increased by $\Delta T = 0.3\,\mathrm{mK}$ above the bath temperature at $T_{\mathrm{MC}} = 10\,\mathrm{mK}$. At a much lower temperature $T_{\mathrm{NR}} = 1\,\mathrm{mK}$, however, the electron temperature is estimated to rise to $T = 2.8\,\mathrm{mK}$ due to poor thermal contact. This strong increase is due to the ohmic contact resistance, which could potentially be further reduced with improved fabrication. In addition, the voltage bias V_{SD} can also still be made much smaller, since a temperature of $T_{\mathrm{NR}} = 1\,\mathrm{mK}$ corresponds to a broadening of the FD distribution of only $\sim 0.1\,\mu\mathrm{V}$, thus still leaving room to fulfill $eV_{\mathrm{SD}} \gg k_B T$.

Our experiments indicate that the electronic noise and external disturbances in the measurements setup play a very important role: excess voltage noise clearly increases the temperatures extracted. Filtering and shielding can be further improved, though already in the present experiment, a significant amount of work was invested [97]. We obtain noise levels as low as several hundred nanovolts across the dot measured at room temperature, but significantly less at the cold device due to filtering. The electron temperature here becomes independent of the noise power at the lowest noise levels, indicating that electronic noise is not the only or not the dominating limitation. The role of the charge sensor as a noise source and possible effects of coupling, back action [111] or sensor heating require further investigation.

The devices used here have outstanding charge stability, with noise on the dot energy level well below 1 µeV [103, 113, 116, 117], making possible temperature measurements as low as ~ 10 mK presented here. Still, device charge instabilities present a serious obstacle if much lower temperatures are to be reached, already severely impeding the measurements here. The temperature measurement would benefit from faster measurements, thus cutting off the noise spectrum at the lowest frequencies and reducing the effect of random telegraph noise. The obvious trade-off is increased signal noise at faster measurement speeds. We emphasize that the charge switching noise exceeds other setup noise such as the voltage sources on the gates, preamplifiers and Johnson noise of the sample wires.

Besides semiconductor charge instabilities, the GaAs nuclear spins can also act as a noise source, giving rise to a fluctuating Zeeman splitting and thus broadening of the single electron energy level (though the energy of a spin singlet would be immune to this noise). With GaAs hyperfine coupling constant $A = 90$ µeV [119] and number of nuclear spins $N \sim 10^5$ to 10^6 enclosed in the electron wave function [120], the resulting energy fluctuations are of order $A/\sqrt{N} \sim 0.1$ µeV and become a limiting factor for $T \lesssim 1$ mK. Finally, heat release from sample holder or other components can also be a limiting factor, resulting in temperatures decaying slowly over a timescale of days. This is difficult to quantify in the present experiment due to the rather large error bars on the extracted temperatures.

In conclusion, we have measured the reservoir electron temperature T with a GaAs quantum dot in both direct transport and charge sensing. We find decent agreement with a CMN thermometer over a broad range down to 10 ± 3 mK. Currently, the main limitations are charge switching noise in the GaAs device, external electronic noise, heating effects due to the charge sensor as well as potential heat release at the lowest temperatures. Even lower temperatures might be achievable by further improving the setup and device, e.g. by better shielding and filtering, choosing materials with lower heat release and possibly optimizing the wafer material and device fabrication.

Acknowledgement

We would like to thank G. Frossati, G. R. Pickett, V. Shvarts, P. Skyba, P. Stano, M. Steinacher and A. de Waard for valuable inputs. This work was supported by Swiss Nanoscience Institute (SNI), NCCR QSIT, Swiss NSF, ERC starting grant and EU-FP7 MICROKELVIN and SOLID.

5 Longitudinal Resistance Quantization and Density Gradient in the Integer Quantum Hall Regime

L. Casparis, M. Lafkioti, T.-M. Liu, D. Maradan, D. M. Zumbühl

Department of Physics, University of Basel, CH-4056 Basel, Switzerland

C. Reichl, W. Dietsche, W. Wegscheider

Solid State Physics Laboratory, ETH Zurich, CH-8046 Zürich, Switzerland

Abstract

We present quantum transport measurements in high-mobility GaAs 2D electron gases at low temperatures. We find a novel sequence of finite resistance plateaus in longitudinal resistance R_{xx} in the integer quantum Hall regime, accompanied by a striking B-field asymmetry and weak or absent fractional quantum Hall states. These signatures can be well understood with charge density gradients across the sample, as confirmed by R_{xy} data. The activation energies of the novel R_{xx} plateaus are surprisingly small, allowing experimental observation only at the lowest temperatures and in ultra-clean samples. Density gradients can be reduced with improved waver growth and smaller distances between ohmic contacts. Nevertheless, our results show that R_{xx} can easily be misleading, characterizing gradients rather than quantum Hall gaps, thus fundamentally jeopardizing R_{xx} as the predominant probe of integer and fractional quantum Hall physics.

This chapter is prepared for publication.

5.1 Introduction

Ever since the discovery of a fractional quantum Hall state (FQHS) at the even-denominator filling factor $\nu = 5/2$ [95], both extensive theoretical [22, 121, 122] and experimental [7, 10, 105, 123] studies have investigated the $\nu = 5/2$ ground-state [23, 81, 124, 125]. Due to its exotic quantum statistics, which are predicted to be non-Abelian [22], a fault tolerant topological quantum computer based on $\nu = 5/2$ quasiparticles [23, 124, 125] has been suggested. Other theoretical proposals have proposed the realization of Majorana fermions in the $\nu = 5/2$ state [82]. Experiments have endeavored to confirm the Moore-Read description through various measurements, including quasiparticle shot-noise [126], quasiparticle tunneling [24, 127], interferometry [128–130] and spin polarization [131] measurements. These experiments are complicated by the small energy gap of the $\nu = 5/2$ state, $\Delta_{5/2} \sim 600\,\mathrm{mK}$ [132], and its fragility in confined structures. Considerable effort has been made to optimize wafer growth in order to increase $\Delta_{5/2}$ and also to get some insight into the mechanisms limiting $\Delta_{5/2}$ [31, 132–134]. From the first observations of the $\nu = 5/2$ state in samples with high mobility, it has been realized that disorder plays a crucial role in the stability of the $\nu = 5/2$ state. Although the correlation between mobility and $\Delta_{5/2}$ has not been so clear in later experiments [31, 135]. Recent results suggest that disorder is indeed a key ingredient [27, 134], but a distinction has to be made between remote impurities, background impurities, alloy disorder in the 2DEG and the interface roughness.

5.2 Experiment

In this letter we report on quantized Shubnikov-de-Haas (SdH) oscillation peaks in the differential longitudinal resistance R_{xx} in a high mobility two dimensional electron gas (2DEG). The strength of this quantization is dependent on the measured contact pairs. Our data can be explained by invoking a charge carrier density gradient. A simple binary charge carrier density gradient model, which is based on the edge channel

picture is discussed. The gradient model can further account for the highly asymmetric behavior of R_{xx} in magnetic field B. Additionally, we investigate the temperature dependence of the R_{xx} quantization. An energy gap associated with the density gradient can be defined. The extracted gaps are in the order of few tens of millikelvin and possibly explain why such a clear observation of the R_{xx} quantization has to the best of our knowledge not been reported before, making very low electron temperatures a prerequisite for the observation. We further demonstrate that the density gradient influences the energy gap determination of the FQHS at $\nu = 5/2$. As typically, the energy gap Δ of any given FQHS is determinined by measuring R_{xx} as a function of temperature. It has been previously shown that this method of extracting the energy gap can be fundamentally flawed in the presence of a density gradient, as then R_{xx} contains no information about the underlying ρ_{xx} [136, 137]. Pan *et al.* also observed a quantization in R_{xx} similar to the one reported in this letter, but only in the special case for reentrant states next to fractional states [136, 137]. Our data shows that the effect of disorder, local density variations and temperature on FQHS is not resolved yet and fundamentally questions the role of R_{xx} as a measure of $\Delta_{5/2}$.

5.2.1 Samples

The devices used in this work are AlGaAs/GaAs quantum wells grown by molecular beam epitaxy (MBE). Two different samples from different wafers are measured. For sample A the 2DEG is formed in a 30 nm wide potential well which lies 245 nm below the surface. Sample B consists of a 30 nm wide 2DEG, buried 195 nm below the surface. The 2DEGs are electrically contacted in a 4 mm by 6 mm van der Pauw geometry. It is important to note that the two wafers have not been rotated during MBE growth.

The mobility of device A at base temperature is $1.9 \cdot 10^7\,\mathrm{cm^2\,V^{-1}\,s^{-1}}$ and the electron density is in the order of $2.3{\cdot}10^{11}\,\mathrm{cm^{-2}}$. The inset of Fig. 5.1(a) displays a contact scheme of sample A. Measurements on sample A are carried out in a dilution refrigerator with a base temperature of 9 mK using standard four-wire lock-in techniques, with

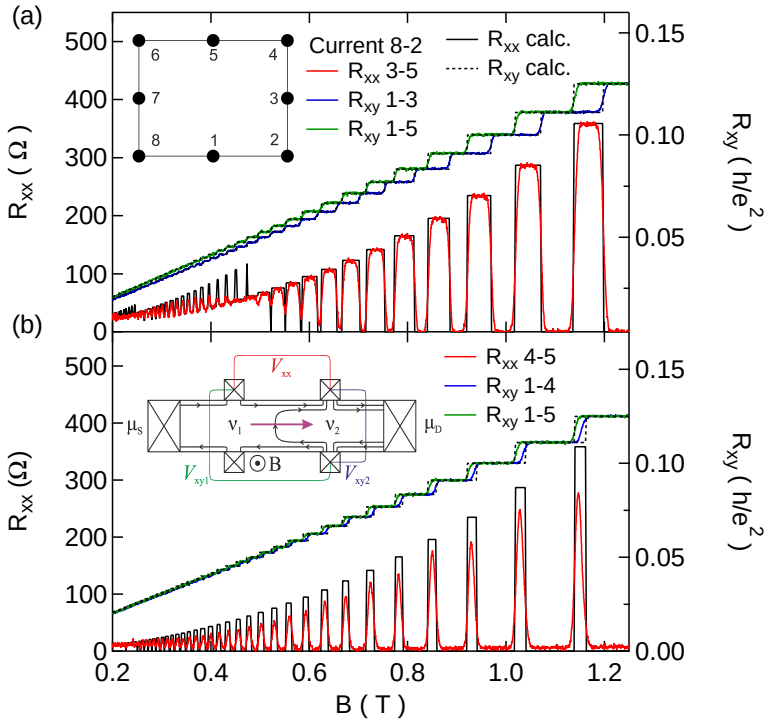

Figure 5.1: Longitudinal resistance quantization. (a) The *inset* shows the contact scheme for sample A. Transversal resistance R_{xy} (blue, green) for contact pairs 1-3 and 1-5 versus magnetic field B. The corresponding longitudinal resistance R_{xx} (red) for contacts 3-5 versus magnetic field B, current flows through contacts 8-2. Black traces are calculated R_{xy} (dashed) and R_{xx} (solid), based on a gradient model, see text. (b) R_{xy} and R_{xx} for a different voltage probe configuration with the same current contacts 8-2 and calculated R_{xy} (black, dashed) and R_{xx} (black, solid). The *inset* illustrates an edge channel picture for the measured device with a density gradient (purple arrow), resulting in two filling factors ν_1 and ν_2.

an AC current-bias excitation of 2 nA at 2.4 Hz. The setup has been optimized for low temperature measurements, including several filtering stages and Ag sinters in the mixing chamber thermalizing every measurement lead [65, 97, 138].

The differential longitudinal resistance R_{xx} and the two corresponding differential Hall resistances R_{xy} are measured simultaneously as a function of magnetic field B. All quoted temperatures are measured using a Cerium Magnesium Nitrate (CMN) thermometer mounted on the mixing chamber. The CMN thermometer was calibrated using a standard fixed-point device with six superconducting transitions between 1.2 K and 96 mK.

5.2.2 Magnetic Field Dependence

In Fig. 5.1(a) R_{xx} between contacts 3 and 5 (current flowing through contacts 8 and 2) is plotted against magnetic field B for sample A. At low B SdH oscillations are visible and exhibit a clear beating (see also Fig. 5.2(a) inset), indicating the presence of two different densities. At higher fields the minima in R_{xx} reach zero, as expected. The striking feature of our data is the quantized value of the maxima in R_{xx}, visible as flat-top peaks. The corresponding R_{xy} traces for contacts 3 and 5 provide further evidence that the densities for contacts 3 and 5 significantly differ. Analyzing the slope of the two R_{xy} traces in the low field region gives the two different densities $n_{1,5} = 2.36{\cdot}10^{11}\,\mathrm{cm}^{-2}$ and $n_{1,3} = 2.48{\cdot}10^{11}\,\mathrm{cm}^{-2}$. To characterize the magnitude of the gradient, we use $\frac{2(n_a-n_b)}{n_a+n_b}$, for two densities n_a and n_b. This results in a 5 % density gradient for contacts 3 and 5. The dashed black curves are calculated Hall resistances for $n_{1,5}$ and $n_{1,3}$, fitting the experimental data very well. The black solid line is the difference between the calculated R_{xy} for the two densities, reproducing the quantization in R_{xx}. As the density gradient might be anisotropic and nonhomogenous, different contact configurations might give different R_{xx} traces, which is indeed observed. Figure 5.1(b) displays the R_{xy} and R_{xx} traces of a different contact pair on the same sample. The difference in density is lower, roughly 2 %, and the maximum R_{xx} values do not reach the quantization values ($n_{1,5} = 2.36 \cdot 10^{11}\,\mathrm{cm}^{-2}$, $n_{1,4} = 2.41 \cdot 10^{11}\,\mathrm{cm}^{-2}$). In the simplest case, a linear density gradient might be easily eliminated choosing the right contact configuration along the direction perpendicular to the gradient. However, we do not observe a simple density gradient in our samples.

Plateaus in R_{xx} have been previously observed in samples with spatially varying electron densities, either due to inhomogeneities in the wafer [136, 137, 139] or due to a constriction in which the density was different [140–142]. In an edge state picture [143], valid at fields above a few hundred millitesla, the two different densities can result in a sample with two different integer filling factor regions (i.e. integer filling factor ν_1 for the lower density region and integer ν_2 for the higher density region). This is schemat-

ically drawn in the inset of Fig. 5.1(b). Combining this binary density edge state picture with the Landauer-Büttiker formalism [144], the observed data is reproduced. One can show that, if the innermost edge channel is returning from the lower sample side between the two upper V_{xx} contacts, R_{xx} is quantized,

$$R_{xx} = \frac{h}{e^2}\left(\frac{1}{\nu_1} - \frac{1}{\nu_2}\right) . \tag{5.1}$$

The measured quantized R_{xx} values are described by the above formula within a few percent accuracy (see also inset of Fig. 5.3). The position of the returning edge state is shifted by a change in B perpendicular to the gradient (purple arrow in the inset of Fig. 5.1(b)), resulting in the observed R_{xx} trace.

Following the observation of plateaus in R_{xx} for fractional states next to reentrant states by Pan *et al.* [137], Ilan *et al.* [145] could show with a classical model that in presence of density gradients, current flows only along one sample side. Therefore, R_{xx} on the current carrying sample side is given by the difference of the local Hall resistivities. On the opposite sample side, where no current flows, no voltage drops between the two contacts, V_{xx} is very small. This is consistent with the edge state picture as displayed in the inset of Fig. 5.1(b), where the return of one edge channel from the lower to the upper side of the sample is not noticed on the lower side voltage contacts.

5.2.3 Asymmetry in Magnetic Field

To test for the predictions of the model, one can switch the magnetic field polarity, as this changes the direction of current flow. Thus either examining the opposite sample side or changing the B-field polarity should result in a vanishing R_{xx}. Figure 5.2(a) shows the same contact configuration as in Fig. 5.1(a) but now for a wider field range and field inversion. One can clearly see the asymmetry upon B-field sign change. The inset in Fig. 5.2(a) shows a zoom-in around zero field, additionally emphazising the

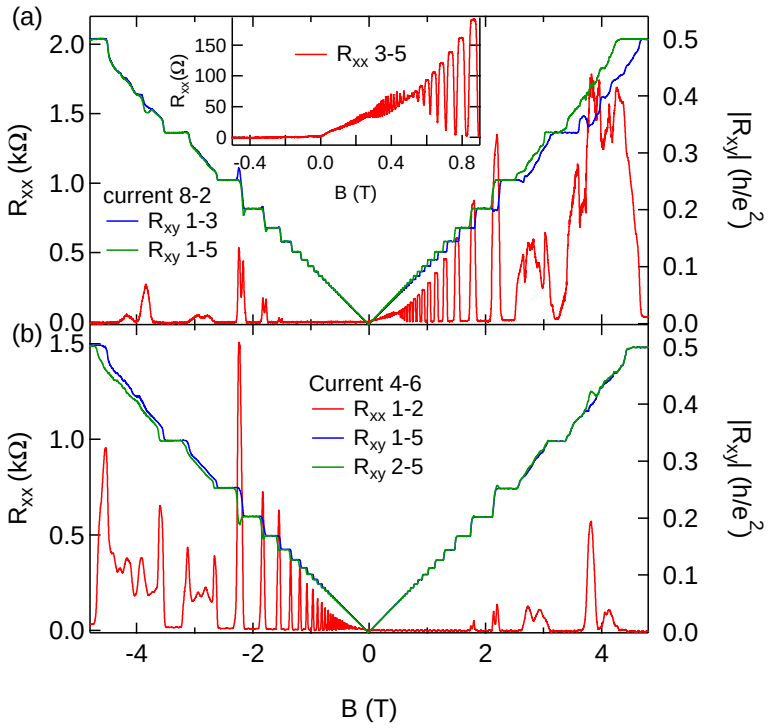

Figure 5.2: Asymmetry in B-field. (a) R_{xy} and R_{xx} versus B for both field polarities. The *inset* shows a zoom-in for R_{xx} around zero field. (b) R_{xy} and R_{xx} plotted versus B for a current and voltage configuration on the opposite sample side.

asymmetry.

At higher negative magnetic fields, overshoots and weak reentrant features can be observed, leading to a peak in R_{xx}. As suggested by Pan *et al.* [137] reentrant features could be viewed as an inversion of filling factors, being consistent with our observations. A recent paper suggests co-existing evanescent incompressible strips as the origin for resistance overshoots [146], which we cannot include in the present model. Interestingly, the overshoots appear for the two different densities always on opposite sides of the QHE plateaus.

In Fig. 5.2(b) we plot a different contact configuration with V_{xx} contacts on the other sample side. The qualitative behavior of R_{xy} and R_{xx} is very similar, except for the inverted polarity for the B-field. Further the quantization in R_{xx} is not that clear, which indicates a lower density gradient.

We propose the inversion of the B-field polarity as a detection tool for possible density

gradients, as in homogeneous samples the two field sides should be perfectly symmetric. For smaller density gradients ($\leq 1\,\%$), Eq. (20) in Ref. [145] could help to reconstruct information about the intrinsic ρ_{xx} [136]. As the density gradient in our sample is large, such that we are not able to measure V_{xx} in the opposite field direction, this method is not applicable. We further note that a B-field asymmetry has been observed before [147], but has been interpreted as an anisotropic resistance state [148].

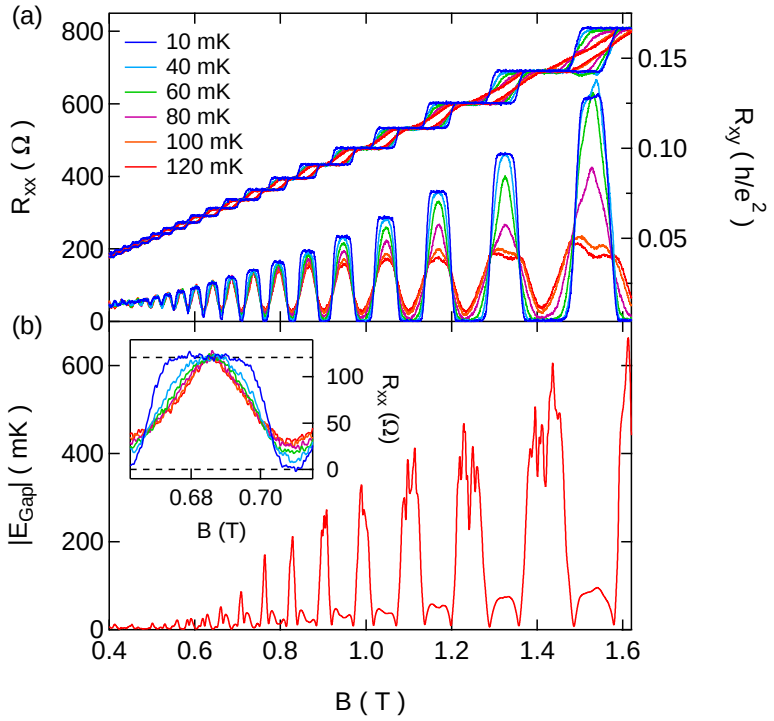

Figure 5.3: Temperature dependence. (a) R_{xx} and R_{xy} against magnetic field B for different temperatures T. (b) From the temperature dependence of $R_{xx}(B,T)$, E_{gap} is extracted and plotted against B, see text. The *inset* shows a zoom-in for the T dependent R_{xx} measurement. Dashed black lines indicate the zero resistance line and the expected value of quantized R_{xx} based on the gradient model.

5.2.4 Temperature Dependence

In order to characterize the density gradient further, we measure the temperature dependence of the R_{xx} quantization. Figure 5.3(a) plots both R_{xy} and R_{xx} against B-field for temperatures between 10 mK and 120 mK. Already at 40 mK the R_{xx} quantization is barely visible anymore. To quantify the temperature range where the effect of the density gradient can be observed, we introduce an energy gap E_{gap}. $E_{gap}(B)$ is extracted

with an Arrhenius plot. $|E_{gap}|$ is determined with a linear fit using $\ln(R_{xx}) \propto \frac{E_{gap}}{2T}$ and plotted in Fig. 5.3(b).

One can see that as the field is increased, the gap of the integer states also increases which is expected. However, the magnitude of the gap is much lower than expected, as at a $B \sim 1\,\mathrm{T}$, the cyclotron energy is in the order of 20 K. Generally, in high mobility samples the QHE plateaus starts only to develop well below 4 K [19, 136]. In our case the density gradient is reducing the gap even further, because of the effective smearing of the integer plateaus. The noise on $|E_{gap}|$ values extracted around the $R_{xx} = 0$ positions is due to the fact that it is impossible to characterize $|E_{gap}| > 300\,\mathrm{mK}$ with a maximum temperature of 120 mK. The energy gap of the R_{xx} quantization is even smaller, showing gaps in the order of few tens of millikelvin. Thus not only a high gradient, but also low electron temperatures are required to observe the quantization in R_{xx}.

5.2.5 $\nu = 5/2$ State Gap Characterization

Another important aspect of our findings is the influence of the gradient on the thoroughly investigated region between filling factors $\nu = 3$ and $\nu = 2$. In the case of the high gradient contact configuration, the R_{xx} trace between 3.2 T and 4.8 T look very unstructured (Fig. 5.2(a)). On the other hand the lower gradient R_{xx} data (Fig. 5.2(b)) exhibits the typical minima for different fractional states, i.e. the $\nu = 7/3$ and $\nu = 8/3$ states. It has been established that for very high quality samples the fractional R_{xx} minima should drop to zero [7], indicating full condensation into the FQHE ground state. We now find that the magnitude of the density gradient might influence the saturation temperature and thus distorts the extraction of the energy gap.

Figure 5.4 presents data from sample B with an electron density of approximately $3 \cdot 10^{11}\,\mathrm{cm^{-2}}$, and a mobility of $\sim 1.9 \cdot 10^{7}\,\mathrm{cm^2\,V^{-1}\,s^{-1}}$. Sample B also exhibits a density gradient, but not as pronounced as sample A. Data for sample B is recorded at a frequency of 27.3 Hz in a different dilution fridge with a base T of 5 mK. An excitation of

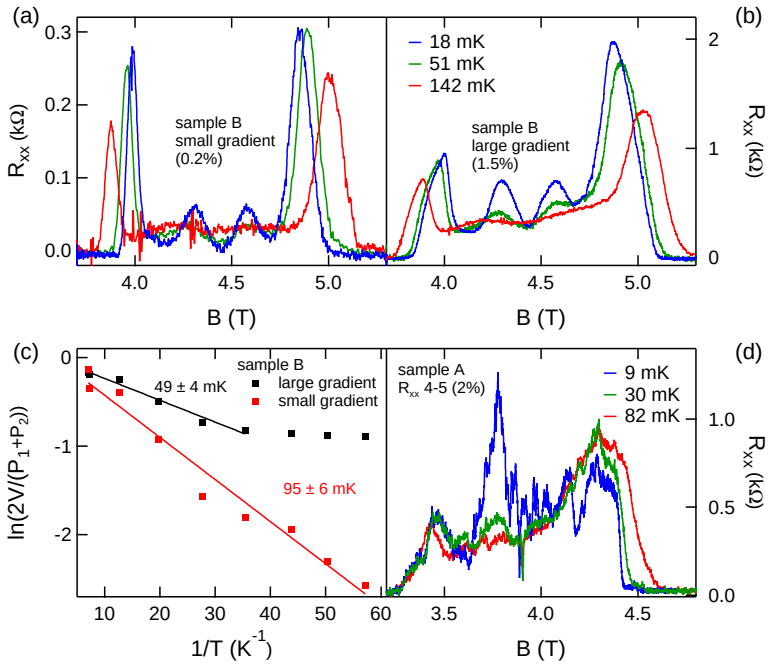

Figure 5.4: Influence of the density gradient on $\Delta_{5/2}$. (a) R_{xx} between $\nu = 3$ and $\nu = 2$ at three different temperatures for the lowest density gradient contact configuration on sample B. (b) R_{xx} between $\nu = 3$ and $\nu = 2$ at three different temperatures for the highest density gradient contact configuration on sample B. (c) Arrhenius plot to extract $\Delta_{5/2}$ for the high gradient (black) and the low gradient (red) configurations. Linear fits give the accordant $\Delta_{5/2}$. (d) R_{xx} between $\nu = 3$ and $\nu = 2$ at three different temperatures for the lowest density gradient contact configuration (contacts 4 and 5) on sample A.

1 nA was chosen in order to prevent heating of the electrons, especially for the sensitive $\nu = 5/2$ gap measurement. Figure 5.4(a) displays R_{xx} data between filling factors $\nu = 3$ and $\nu = 2$ for the lowest gradient contact pair (0.2 %) for three temperatures. As a comparison in Fig. 5.4(b) the highest gradient contact pair (1.5 %) is plotted. The amplitudes of the R_{xx} peaks are lower for the low gradient pair. Further, the $\nu = 5/2$ minimum is lower for the lower gradient contacts. We extract $\Delta_{5/2}$ for the different density gradients on the same sample, by dividing the depth of the minimum V of R_{xx} by the averaged peak heights P_1 and P_2 flanking the minimum [105, 123]. In Fig. 5.4(c) the Arrhenius plot for the two different contact configurations in Fig. 5.4(a) and (b) are plotted. Interestingly, the extracted $\Delta_{5/2}$ differ by a factor of 2 for the two contact configurations. The high gradient R_{xx} measurement results in a gap of approximately 50 mK. On the same sample the low electron density gradient configuration yields a

$\nu = 5/2$ gap of almost 100 mK. Further the saturation temperature below which $\frac{2V}{(P_1+P_2)}$ does not follow temperature anymore seems to be correlated to the gradient. For the low electron density gradient the data follows temperature down to roughly 17 mK, whereas the high gradient data already saturates at 28 mK. In a very simple picture, the density differences in the sample lead to a smearing effect of signatures of intrinsic FQHS features. If the temperature broadening is smaller than the density smearing one only sees the effect of the density gradient, i.e. R_{xx} saturates at a temperature given by the density smearing. At higher temperatures the broadening due to temperature will be visible again, as observed in our data.

We note that for the low gradient contact configuration the density gradient is actually comparable to gradients observed in very high quality samples [137]. Therefore the saturation of the temperature dependence of $\frac{2V}{(P_1+P_2)}$ and $\Delta_{5/2}$ seem to be limited by disorder, rather than the density gradient.

In order to compare the two samples A and B, Fig. 5.4(d) plots a low gradient configuration (2 %) for sample A, where no gap extraction was possible.

5.3 Discussion

In summary, we have demonstrated that a density gradient in a 2DEG can lead to a longitudinal resistance R_{xx}, which is governed solely by the difference in local electron density between the two contacts, in extreme cases leading to quantization of R_{xx} in the integer regime. As a consequence upon inversion of magnetic field or current direction, the R_{xx} traces are highly asymmetric, which allows to check for density gradients. The temperature dependence of R_{xx} shows that even for the biggest density gradient the quantization is only visible at the lowest electron temperatures, showing energy gaps in the order of tens of millikelvin.

We show that a significant density gradient can fundamentally flaw the $\Delta_{5/2}$ extraction, because R_{xx} is not reflecting the intrinsic ρ_{xx} [137], which would carry the information

about the ground state population of the $\nu = 5/2$ state. Depending on the contact configuration, $\Delta_{5/2}$ vary between 100 mK and 50 mK on the same wafer. The temperature below which R_{xx} at $\nu = 5/2$ saturates also seems to be related to the gradient. We suggest that in order to determine $\Delta_{5/2}$, future experiments should focus not on R_{xx} (or only after thoroughly investigating it), but rather on R_{xy}. For example the field range over which R_{xy} is quantized at $\frac{2h}{5e^2}$ as a function of temperature could serve as an indication for the size of $\Delta_{5/2}$.

It is very likely that rotation during wafer growth, as the standard procedure is, will suppress the density gradient. However, due to different locations of the MBE targets within the vacuum chamber it will be difficult to eliminate some local variation in density completely. Another approach to overcome this limitation could be a reduction of contact to contact distances.

6 Tunnel-Junction Thermometry Down to Millikelvin Temperatures

A. V. Feshchenko*, I. M. Khaymovich, O.-P. Saira, M. Meschke, J. P. Pekola

Low Temperature Laboratory, Aalto University, FI-00076 Aalto, Finland

L. Casparis*, D. Maradan, M. Palma, D. M. Zumbühl

Department of Physics, University of Basel, CH-4056 Basel, Switzerland

Abstract

We present a simple on-chip electronic thermometer with the potential to operate down to 1 mK. It is based on transport through a single normal-metal–superconductor tunnel junction with rapidly widening leads. The current through the junction is determined by the temperature of the normal electrode that is efficiently thermalized to the phonon bath, and it is virtually insensitive to the temperature of the superconductor, even when the latter is relatively far from equilibrium. We demonstrate here the operation of the device down to 7 mK and present a systematic thermal analysis.

* These authors contributed equally to this work.

This chapter was published in *Phys. Rev. Appl.* **4**, 034001 (2015).

6.1 Introduction

On-chip electronic thermometry is an important part of modern research and commercial applications of nanotechnology, and it has been studied already for several decades; see Ref. [149] and references therein. Many of these thermometers are based on tunnel junctions or quantum dots [99, 138, 150]. Temperature sensors based on normal (N) and superconducting (S) metal tunnel junctions are used in a wide range of experiments [151–153] and applications [154, 155]. An example of such a device is a primary Coulomb blockade thermometer (CBT) that is based on normal-metal tunnel junctions with an insulator "I" as a tunnel barrier (NIN) [85, 97], where the electronic temperature can be obtained by measuring the smearing of the single-electron blockade. One more example is an SNS thermometer [156], whose critical current I_c depends strongly on the temperature. Primary electronic thermometry has also been successfully demonstrated down to 10 mK using the shot noise of a tunnel junction (SNT) [84, 157, 158]. Nowadays, a standard dilution refrigerator reaches a temperature of [5..10] mK, with a record of 1.75 mK [51, 159]. Nevertheless, a thermometer that has a modest structure and a simple but accurate temperature reading at sub-10 mK temperatures and does not require a complicated experimental setup is still missing. For this purpose, we present an NIS junction that is widely used both as a refrigerating element and a probe of the local electronic temperature in different experiments and applications [151–155, 160–162]. The possibility to use the NIS junction at sub-10 mK temperatures makes this thermometer suited for cryogenic applications at low temperatures. For instance, quantum information is a highly focused and rapidly developing field in modern physics. For many realizations, such as superconducting and quantum dot qubits, one needs to define a set of quantum states at low temperature that are well separated and well controlled and insensitive to noise and decoherence effects [82]. Several experimental realizations of two-level systems [79, 103, 163] suggest that decreasing temperature further will increase the coherence times as well as improve charge sensitivity. We think that our thermometer will be interesting for a community who is willing to discover

new physics as well as improve already existing devices that require low temperatures for their proper functioning. The NIS thermometer is easy to operate compared to SNT [84, 157], and its thermalization is quite straightforward compared to CBT [97] due to the single junction configuration and can be combined on-chip with other solid-state devices. A measurement of the NIS current-voltage (I-V) characteristic yields a primary temperature reading.

In this paper, we study both experimentally and theoretically an on-chip electronic thermometer based on a single NIS tunnel junction at sub-10 mK temperatures. We demonstrate the operation of the NIS thermometer down to 7.3 mK. In addition, we develop a thermal model that explains our measurement data and shows that self-heating effects remain negligible for temperatures down to 1 mK.

6.2 Theoretical Background

Transport through an NIS junction has strong bias and temperature dependence. Near zero bias voltage, the current is suppressed due to the superconducting gap Δ [164]. When biased at voltage V, the current depends on temperature due to the broadening of the Fermi distribution $f_N(E) = [\exp(E/k_B T_N) + 1]^{-1}$ in the normal metal with temperature T_N and Boltzmann constant k_B. The current can be expressed as [164]

$$I = \frac{1}{2eR_T} \int_{-\infty}^{+\infty} dE\, n_S(E) \left[f_N(E - eV) - f_N(E + eV) \right], \tag{6.1}$$

where R_T is the tunneling resistance of the junction and E is the energy relative to the chemical potential.

In the superconductor, the Bardeen-Cooper-Schrieffer (BCS) density of states is smeared and typically described by the Dynes parameter γ, which can be expressed as $n_S(E) = \left| \Re e(u/\sqrt{u^2 - 1}) \right|$ (see supplemental material in Ref. [165]), where $u = E/\Delta(T_S) + i\gamma$ and T_S is the temperature of the superconductor. Possible origins of γ include broadening of the quasiparticle energy levels due to finite lifetime [166],

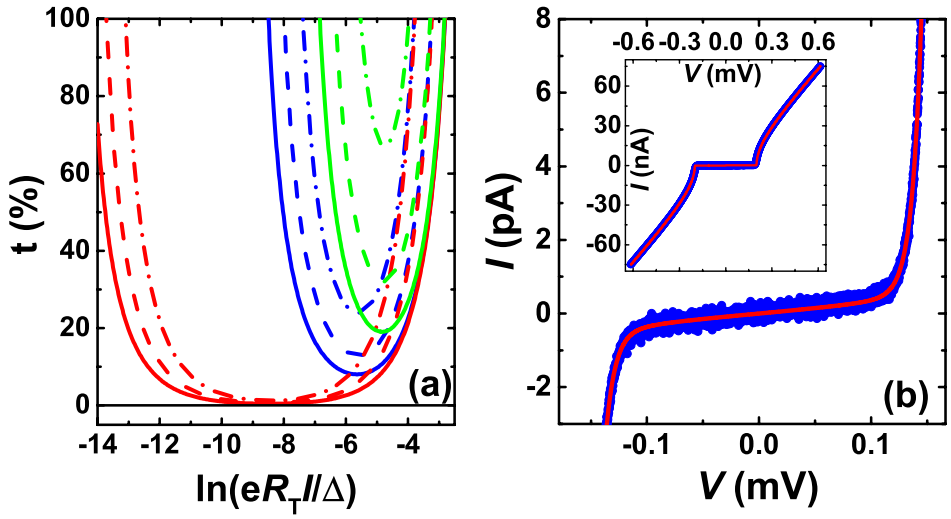

Figure 6.1: In panel (a), we show the relative deviation of the present thermometer reading using method B with a numerically calculated I-V, Eq. (6.1). Sets of curves present the values of t for three γ parameters: 10^{-7}, $2.2 \cdot 10^{-5}$ (the actual value in the experiment), and 10^{-4} shown as red, blue and green curves from left to right. For each γ, temperatures 1, 3, and 7 mK are shown as dash-dotted, dashed, and solid lines, respectively. All curves are calculated using the parameters of the measured device with $\Delta = 200\,\mu\text{eV}$ and $R_T = 7.7\,\text{k}\Omega$. The main panel (b) shows the measured I-V characteristic (blue dots) together with the full fit (solid red line) enlarged in the superconducting gap region. *Inset:* Measured and calculated I-V curve on a wider voltage scale at approximately 10 mK.

Andreev current [167, 168], as well as photon-assisted tunneling caused by high-frequency noise and black-body radiation [165]. The typical experimental range of γ for Al-based[1] tunnel junctions is 10^{-4} to 10^{-5} for a single NIS junction [165, 173], getting as low as 10^{-7} in SINIS single-electron transistors with multistage shielding [174].

One can determine T_N from a measured I-V curve using Eq. (6.1). As we show below, the self-heating of both N and S electrodes has a small effect on the I-V characteristic; thus, for now, we neglect these effects. Therefore, we assume temperatures to be small, $k_B T_{N,S} \ll eV, \Delta(T_S)$, and the superconducting gap to be constant and equal to its zero-temperature value Δ. In this case for $eV < \Delta$, one can approximate Eq. (6.1) by

$$I \simeq I_0 \exp\left(\frac{-(\Delta - eV)}{k_B T_N}\right) + \frac{\gamma V}{R_T \sqrt{1 - (eV/\Delta)^2}}\,, \tag{6.2}$$

[1] Tunnel junctions based on Nb, NbN or NbTiN have higher γ values, usually up to 10^{-2} [169–172].

where $I_0 = \sqrt{2\pi\Delta k_B T_N}/2eR_T$ [152, 167]. Here the second term stands for the corrections to the I-V characteristic due to smearing. It leads to the saturation of the exponential increase of the current at low bias values. In the regime of moderate bias voltages, one can neglect this term and invert Eq. (6.2) into

$$V = \frac{\Delta}{e} + \frac{k_B T_N}{e} \ln(I/I_0)\,. \tag{6.3}$$

This equation provides a way to obtain the electronic temperature T_N^B by only fundamental constants and by the slope of the measured I-V characteristic on a semilogarithmic scale as

$$T_N^B(V) = \frac{e}{k_B} \frac{dV}{d(\ln I)}\,. \tag{6.4}$$

Equation (6.4) allows us to use the NIS junction as a primary thermometer, however, with some limitations. One can include the effects of γ into Eq. (6.4) by subtracting the last term in Eq. (6.2) from the current I and obtain a better accuracy. We do not take this approach here, since the main advantage of Eq. (6.4) is its simplicity as a primary thermometer without any fitting parameters.

Next, we will compare the two methods used to extract the electronic temperature from the measured I-V curves. In method A, we employ Eq. (6.1) and perform a nonlinear least-squares fit of a full I-V curve with T_N as the only free parameter. The value of T_N obtained in this manner, named T_N^A, is not sensitive to γ. Method B is based on the local slope of the I-V, see Eq. (6.4). The smearing parameter γ has an influence on the slope of the I-V characteristic and, thus, induces errors in the temperature determination. The temperature T_N^B is extracted as the slope of measured V vs $\ln I$ over a fixed I range for all temperatures where Eq. (6.4) is valid. In the experiment, it is usually difficult to determine the environment parameters precisely, but one can determine γ from the ratio of R_T and the measured zero-bias resistance of the junction. The I-V which takes the γ parameter into account, see Eq. (6.2), gives indistinguishable

results from the ones obtained by method A.

We evaluate the influence of the γ parameter on the relative deviations of the present thermometer based on method B numerically, as shown in Fig. 6.1(a). This deviation t is defined as the relative error $t = (T_N^B/T_N) - 1$. We show the values of t vs $\ln(eR_T I/\Delta)$ for two extreme cases $\gamma = 10^{-7}$, 10^{-4} and for $\gamma = 2.2 \cdot 10^{-5}$ extracted from the present experiment at temperatures of 1, 3 and 7 mK. The lowest bath temperature is 3 mK, and 7 mK is the saturation of the electronic temperature in the current experiment. The larger the values of γ and the lower the temperature, the higher the relative deviations. In addition, the range of the slope used to extract T_N^B shrinks with increasing γ and with decreasing temperature, see e.g. red curves in Fig. 6.1(a). Thus, reducing the leakage will significantly improve the accuracy of the device, especially towards lower temperatures. Possible avenues for suppressing γ include improved shielding [174, 175] and encapsulating the device between ground planes intended to reduce the influence of the electromagnetic environment [165]. Finally, higher tunneling resistance of the junction decreases Andreev current [176]. We note that one can also use $dV/d(\ln g)$ as a primary thermometer, where $g = dI/dV$ is the differential conductance – typically a more precise measurement since it is done with a lock-in technique. Compared to Eq. (6.4), this method has the minimal deviation t reduced by at least a factor of 3.5 for $T_N \geq 1$ mK (6 for $T_N \geq 10$ mK), though exhibiting qualitatively similar dependencies on γ and T_N.

6.3 Experimental Realization and Measurement Techniques

Next, we describe the realization of the NIS thermometer that is shown together with a schematic of the experimental setup in the scanning-electron micrograph in Fig. 6.2.

The device is made by electron-beam lithography using the two-angle shadow evaporation technique [177]. The ground plane under the junction is made out of 50 nm of Au. To electrically isolate the ground plane from the junction, we cover the Au layer with 100 nm of AlO_x using atomic layer deposition. Next, we deposit a layer of $d_S = 40$ nm

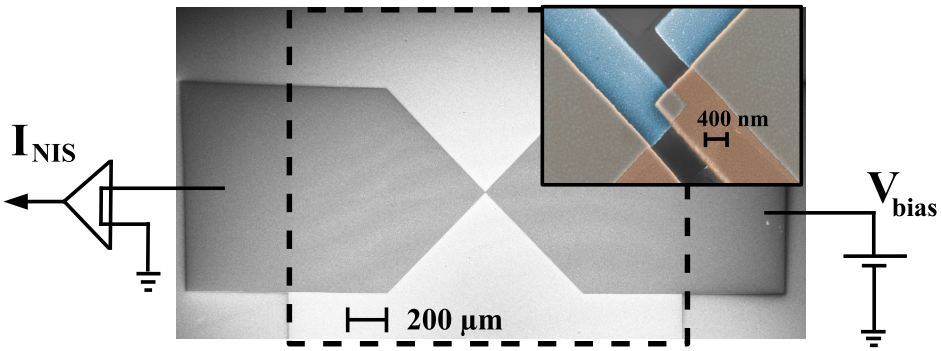

Figure 6.2: A scanning-electron micrograph of the NIS device together with a schematic of the experimental setup. In the main panel, the S and N leads of the junction visible, and underneath the pads, the ground plane of a square shape is indicated by a dashed line. The enlarged *inset* shows the actual tunnel junction where the S and N leads are indicated by blue and brown color, respectively.

of Al that is thermally oxidized *in situ*. The last layer is formed immediately after the oxidation process by deposition of $d_N = 150\,\mathrm{nm}$ of Cu, thus creating an NIS tunnel junction with an area $A = (380 \times 400)\,\mathrm{nm}^2$. The geometry of the junction is chosen such that the leads immediately open up at an angle of 90° and create large pads with areas of $A_N = A_S = 1.25\,\mathrm{mm}^2$ providing good thermalization. The S lead is covered by a thick normal-metal shadow as shown in brown in the inset of Fig. 6.2, where N and S layers are interfaced by the same insulating layer of AlO_x as the junction.

The experiment is performed in a dilution refrigerator (base temperature 9 mK) where each of the sample wires is cooled by its own, separate Cu nuclear refrigerator (NR) [69], here providing bath temperatures T_{bath} down to 3 mK. Nuclear refrigerator temperatures after demagnetization are highly reproducible and obtained from the precooling temperatures and previously determined efficiencies [97]. Temperatures above $\sim 9\,\mathrm{mK}$ are measured with a cerium magnesium nitrate thermometer which is calibrated against a standard superconducting fixed-point device. Since the sample is sensitive to the stray magnetic field of that applied on the nuclear refrigerators, this field is compensated down to below 1 G using a separate solenoid. The I-V curves (see Fig. 6.2 for the electrical circuit) are measured using a home-built current preamplifier with input offset-voltage stabilization [178] to minimize distortions in the I-V curves.

Filtering, radiation shielding and thermalization are crucial for obtaining a low γ and

low device temperatures. Each sample wire goes through 1.6 m of thermocoax, followed by a silver epoxy microwave filter [65], a 30 kHz low-pass filter and a sintered silver heat exchanger in the mixing chamber before passing the Al heat switch and entering the Cu nuclear stage. The setup is described in detail in Ref. [97] (chapter 3) and has been further improved here (see 6.7 Appendix for more details).

6.4 Results and Discussion

In Fig. 6.1(b), the measured I-V characteristic in the superconducting gap region is shown by blue dots. The solid red line corresponds to the full fit based on method A. In the inset, we present the I-V characteristic at a larger voltage scale used to extract R_T.

In Fig. 6.3(a), the measured I-V's of the NIS junction are shown in logarithmic scale by blue dots at various $T_{\rm bath} = [100..3]$ mK from left to right. The full fits are shown as dashed red lines. The tunneling resistance $R_T = 7.7\,\mathrm{k}\Omega$ and the Dynes parameter $\gamma = 2.2 \cdot 10^{-5}$ used in all these fits are determined based on the I-V's shown in Fig. 6.1(b) at high and low voltages, respectively. For the lowest temperatures, T_N from the nonlinear fit depends strongly on the superconducting gap[2], making it difficult to determine the gap with high enough accuracy[3]. However, Eq. (6.1) gives a possibility to perform a nonlinear least-squares fit and Eq. (6.3) gives a linear fit, where the parameters Δ and T_N are responsible for the offset and the slope, respectively. Therefore, at high temperatures (~ 100 mK in the present experiment), one can narrow down the uncertainty in Δ such that T_N becomes essentially an independent parameter for the fits. Thus, the gap extracted from the high-temperature data using Eq. (6.1) remains fixed, $\Delta = 200 \pm 0.5\,\mu$eV, for all temperatures below 100 mK. In addition, we show as solid black lines an exponential I-V dependence corresponding to method B with a fitting range between 5 and 400 pA. The enlarged inset shows the I-V curves at temperatures of 10 and 7 mK. The I-V characteristics presented in Fig. 6.3(a) agree well

[2] A reduction of the superconducting gap by 0.1 % changes T_N by 10 % at the lowest temperature.

[3] With the given experimental uncertainties, we can determine the gap with a precision of 0.25 % ($\pm 0.5\,\mu$eV).

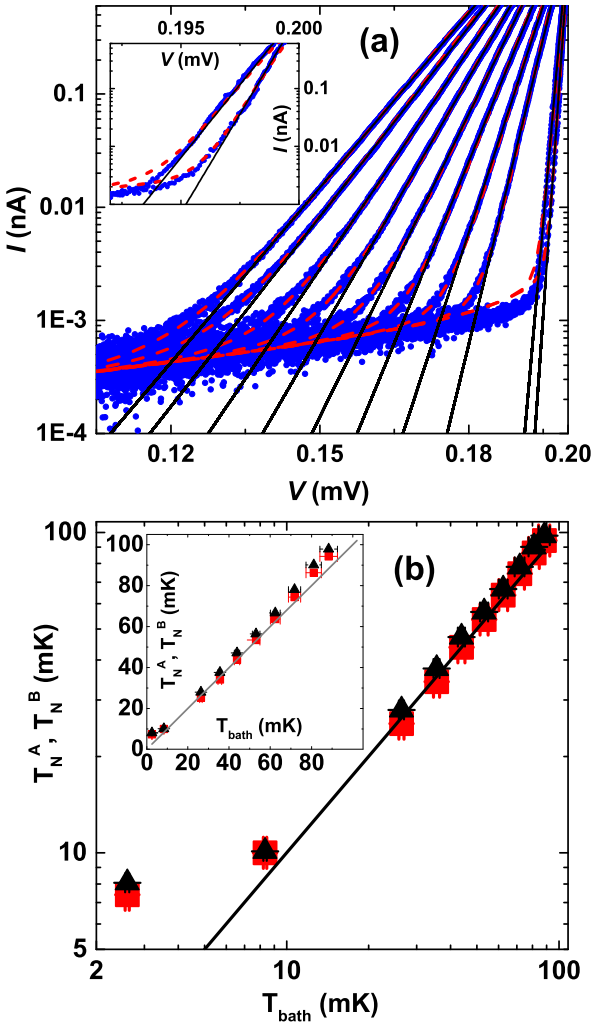

Figure 6.3: Panel (a) shows measured I-V's (blue dots) when T_{bath} is lowered from left to right together with fits as solid black and dashed red lines (see text). *Inset:* Close-up of two I-V's for temperatures of 10 and 7 mK. The electronic temperature extracted from both the full fit (red squares) of the I-V's and their slopes (black triangles) are shown in (b).

with the theoretical expressions in Eqs. (6.1) and (6.2) (the latter form is not shown). In Fig. 6.3(b), we show the electronic temperatures obtained using method A (red squares) and method B (black triangles) vs T_{bath}. Method A (B) shows a relative error in the electronic temperature up to 6 % (11 %). The error in method B is larger, as we neglect the influence of the γ parameter.

The lowest temperature obtained from the full fit is $T_N^A = 7.3\,\mathrm{mK}$ with statistical uncertainty of 5 % at $T_{\mathrm{bath}} = 3\,\mathrm{mK}$. The NIS temperature decreases slowly over time, arriving at 7.3 mK several weeks after the cool down from room temperature. This suggests that internal relaxation causing a time-dependent heat leak, e.g. in the silver epoxy sample holder, is limiting the minimum temperature. Future improvements will employ low-heat-release materials better suited for ultralow temperatures such as sapphire or pure annealed metals, e.g. for the socket and chip carrier, minimizing organic noncrystalline substances such as epoxies.

6.5 Thermal Model

The total power dissipated in the device is equal to $IV = \dot{Q}^N_{\mathrm{NIS}} + \dot{Q}^S_{\mathrm{NIS}}$, where $\dot{Q}^N_{\mathrm{NIS}}$ and $\dot{Q}^S_{\mathrm{NIS}}$ are the heat powers to the normal metal and to the superconductor, respectively. The heat released to the superconductor is given by

$$\dot{Q}^S_{\mathrm{NIS}} = \frac{1}{e^2 R_T} \int E_S n_S(E) \left[f_N(E - eV) - f_S(E) \right] dE\,, \tag{6.5}$$

where $E_S = E$ is the quasiparticle energy. To evaluate $\dot{Q}^N_{\mathrm{NIS}}$, one has to substitute E_S by $E_N = (eV - E)$ in Eq. (6.5). Almost all of the heat is delivered to the superconductor in the measured (subgap) bias range, thus, $\dot{Q}^S_{\mathrm{NIS}} \sim IV$ and $\dot{Q}^N_{\mathrm{NIS}} \ll \dot{Q}^S_{\mathrm{NIS}}$.

So far, we neglect all self-heating effects both in the normal metal and in the superconductor. To justify the no-self-heating assumption, we check numerically and analytically these self-heating effects. We sketch the analytical arguments in section 6.7 Appendix. Here we state the main results obtained from the thermal model.

Self-heating of the superconductor can take place due to the exponential suppression of thermal conductivity and the weak electron-phonon (*e-ph*) coupling, especially at low temperatures. We find that the superconductor temperature T_S stays below 250 mK in the subgap bias range $|V| \leq \Delta/e$ and does not influence the thermometer reading. In this bias range and at $T_{\mathrm{bath}} = 3\,\mathrm{mK}$, we estimate based on the numerical calculations the temperature of the superconductor $T_S = 145\,\mathrm{mK}$ and the power injected to the superconductor is $IV \approx 90\,\mathrm{fW}$. At the same time, we evaluate the relative change of the slope to be small $|t| \lesssim 5 \cdot 10^{-3}$ at $I \lesssim 1\,\mathrm{nA}$. In conclusion, the temperatures obtained from both methods A and B are affected by less than 0.5 % by self-heating of the superconductor[4]. In addition, the normal metal might get self-heated due to weak electron-phonon coupling and backflow of heat from the superconductor [179]. The influence of the self-heating of the normal metal down to 1 mK temperature affects the temperature obtained from both methods A and B by less than 0.5 % as well, as in the case of self-heating of the superconductor.

6.6 Conclusions

In conclusion, we have demonstrated experimentally the operation of an electronic thermometer based on a single NIS tunnel junction. The thermometer agrees well with the refrigerator thermometer down to about 10 mK and reaches a lowest temperature of 7.3 mK at $T_{\mathrm{bath}} = 3\,\mathrm{mK}$, currently limited by a time-dependent heat leak to the sample stage. We have discussed several possible improvements of the present device and experimental setup. Finally, we have shown that self-heating in the normal metal and in the superconductor on the full *I-V* or its slope is negligible, paving the way for NIS thermometry down to 1 mK if the experimental challenges can be overcome.

[4]The temperature of the superconductor will affect T_N through the dependence of the *I-V* curve on the magnitude of the gap. The geometry of the device can influence the number of quasiparticles and, consequently, the effective temperature of the superconductor.

Acknowledgement

We thank G. Frossati, G. Pickett, V. Shvarts, and M. Steinacher for valuable input. We acknowledge the availability of the facilities and technical support by Otaniemi Research Infrastructure for Micro- and Nanotechnologies (OtaNano). We acknowledge financial support from the European Community FP7 Marie Curie Initial Training Networks Action Q-NET 264034, MICROKELVIN (Project No. 228464), SOLID (Project No. 248629), INFERNOS (Project No. 308850), EMRP (Project No. SIB01-REG2), and the Academy of Finland (Projects No. 284594 and No. 272218). This work is supported by Swiss Nanoscience Institute, NCCR QSIT, Swiss NSF, and an ERC starting grant under agreement No. 207599.

6.7 Appendix

Experimental Techniques

The setup described in Ref. [97] was improved as follows. First, a ceramic chip carrier was replaced by silver epoxy parts which remain metallic to the lowest temperatures, allowing more efficient cooling. Further, the sample – previously mounted openly inside the cold-plate radiation shield together with the nuclear stage – is enclosed in an additional silver shield, sealed with silver paint against the silver epoxy socket, and thermalized to one of the Cu refrigerators, see Fig. 6.4. Finally, each wire is fed into the sample shield through an additional silver epoxy microwave filter. While previously saturating at 10 mK or above [97], metallic CBTs have given temperatures around 7 mK after the improvements [4, 65], comparable to the NIS temperatures presented here.

Estimates of the Subgap Conductance

The Dynes parameter γ can be attributed to the higher-order processes such as Andreev tunneling events. Assuming ballistic transport and an effective area of the conduction

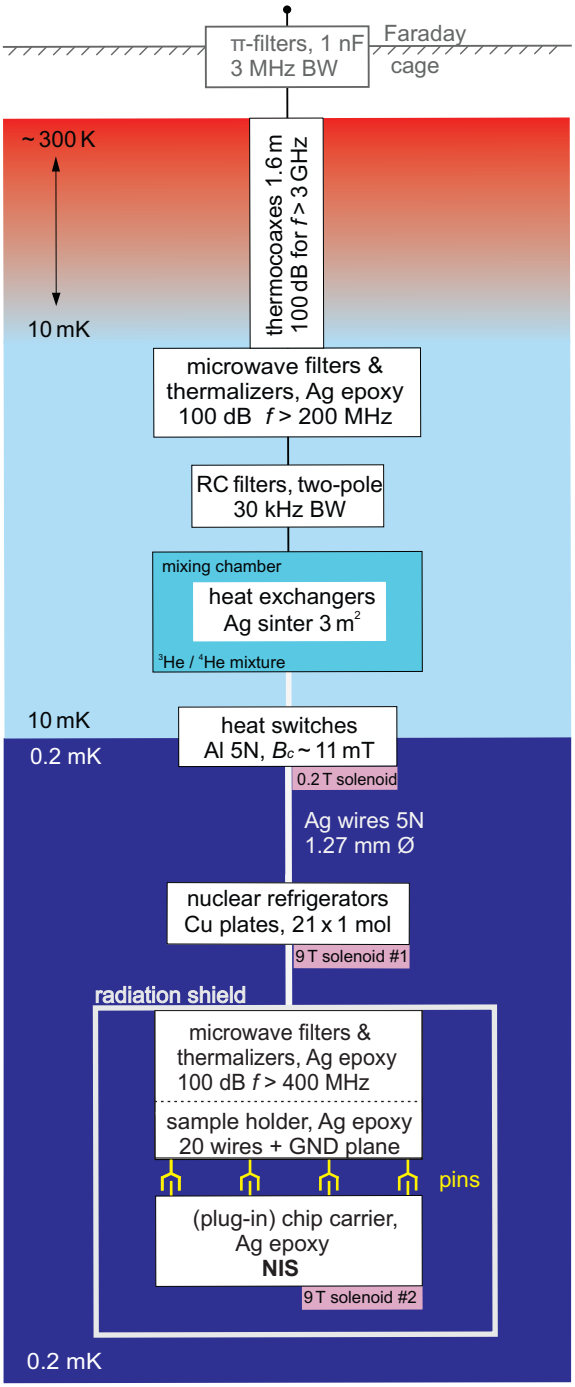

Figure 6.4: Scheme of a dilution unit together with a nuclear stage. Radiation shields (not shown) are attached to the still and cold plate ($\sim 50\,\mathrm{mK}$). The RC filters are $1.6\,\mathrm{k\Omega}/2.2\,\mathrm{nF}$ and $2.4\,\mathrm{k\Omega}/470\,\mathrm{pF}$. The 21 NR plates are $(32 \times 2.5 \times 90)\,\mathrm{mm}^3$ each, amounting to 64 g Cu per plate. The NRs cool as low as 0.2 mK. In the present experiment, the lowest T_{bath} used is 3 mK. Compared to Ref. [97], the improved setup depicted here features a Ag epoxy socket, a Ag epoxy chip carrier, and a second filtering stage with radiation-tight feedthroughs into an additional sample radiation shield. The abbreviations BW, B_c and GND presented in the schematic stand for bandwidth, critical magnetic field and electrical ground, respectively.

channel $A_{ch} = 30\,\mathrm{nm}^2$ [180, 181], a simple estimate of subgap Andreev conductance reads $\sigma_{\mathrm{AR}} = R_K/(8NR_T) = 8.5 \cdot 10^{-5}$ in units of R_T^{-1}, where R_K is the resistance quantum, N is the effective number of conduction channels, $N = A/A_{ch}$, where A is the area of the junction. Alternatively, the estimate based on diffusively enhanced Andreev conductance yields $7.5 \cdot 10^{-5}$ of corresponding dimensionless conductance. These values are of the same order of magnitude as in our experiment ($\gamma = 2.2 \cdot 10^{-5}$) and fall in the range of earlier experiments [168].

Theoretical Estimates for the Relative Deviations of the Present Thermometer

The theoretical deviations of $dV/d(\ln I)$ at $\gamma = 2.2 \cdot 10^{-5}$ numerically calculated from I-V, Eq. (6.1), are rather large, particularly at low temperatures ($\sim 30\,\%$ at 1 mK; see solid blue curve in Figs. 6.1(a) and 6.5). Measuring differential conductance $g = dI/dV$ rather than current I significantly reduces the predicted deviations $t_g = T_N^{slope,g}/T_N - 1$, where $T_N^{slope,g} = [dV/d(\ln g)]e/k_B$. The minimum of these deviations gets broader and potentially reduces measurement noise since it is a lock-in measurement – overall strengthening method B. In Fig. 6.5, we show two sets of curves for t_g (thick purple curves) and t (thin blue curves) from left to right for comparison. Sets are calculated based on the experimental parameters for $\gamma = 2.2 \cdot 10^{-5}$, $\Delta = 200\,\mu\mathrm{eV}$, and $R_T = 7.7\,\mathrm{k}\Omega$. Each set corresponds to the temperatures 1, 3, and 7 mK and is shown as dash-dotted, dashed and solid lines, respectively. Here, the t set is identical to the set with $\gamma = 2.2 \cdot 10^{-5}$ that is shown in Fig. 6.1(a).

Self-Heating of the Superconductor

We study the heat transport in the present geometry (see Fig. 6.2) by a diffusion equation assuming a thermal quasiparticle energy distribution [182, 183]

$$-\nabla\left(\kappa_S \nabla T_S\right) = u_S\,, \tag{6.6}$$

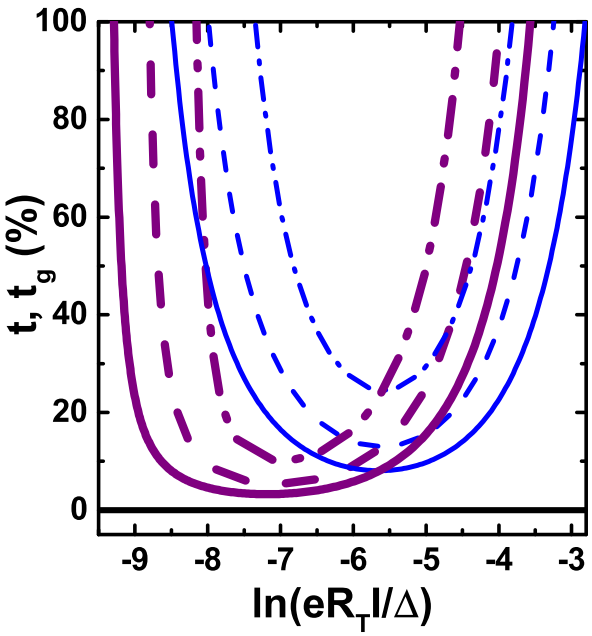

Figure 6.5: The theoretical deviations t and t_g of the thermometer reading using method B based on $I(V)$ and $g(V)$, respectively. These deviations are shown for temperatures 1, 3, and 7 mK as dash-dotted, dashed and solid lines, respectively. Parameters used are $\gamma = 2.2 \cdot 10^{-5}$, $\Delta = 200\,\mu\text{eV}$, and $R_T = 7.7\,\text{k}\Omega$ as in the actual experiment.

where we set a boundary condition near the junction $-\bar{n}_{\text{inner}}\kappa_S \nabla T_S|_{\text{junct}} = \dot{Q}^S_{\text{NIS}}/A$, where $\bar{n}_{\text{inner}}$ is the inner normal to the junction. The thermal conductivity in the superconductor is

$$\kappa_S = \frac{6}{\pi^2}\left(\frac{\Delta}{k_B T_S}\right)^2 \exp\left(\frac{-\Delta}{k_B T_S}\right) L_0 T_S \sigma_{Al}\,, \tag{6.7}$$

where L_0 is the Lorenz number, and $\sigma_{Al} = 3 \cdot 10^7\ (\Omega\text{m})^{-1}$ is the electrical conductivity of the Al film in the normal state [183]. We take into account the T_S dependence of the gap at low temperatures, $\Delta(T_S)/\Delta \simeq 1 - \sqrt{2\pi k_B T_S/\Delta}\exp\left(-\Delta/k_B T_S\right)$. The absorbed heat is given by $u_S = \dot{q}^S_{e-ph} + \dot{q}_{\text{trap}}$. Here, the first term is the electron-phonon power $\dot{q}_{e-ph,S} \simeq \Sigma_{Al}(T_S^5 - T_p^5)\exp\left(-\Delta/k_B T_S\right)$ [184], where $\Sigma_{Al} = 3 \cdot 10^8\,\text{W}\,\text{K}^{-5}\,\text{m}^{-3}$ is the material-dependent electron-phonon coupling constant. The phonon temperature T_p is assumed to be equal to T_{bath}. Because of weak electron-phonon coupling, nearly all the heat is released through the (unbiased) normal-metal shadow (see Fig. 6.6) that acts as a trap for quasiparticles, $\dot{q}_{\text{trap}}$.

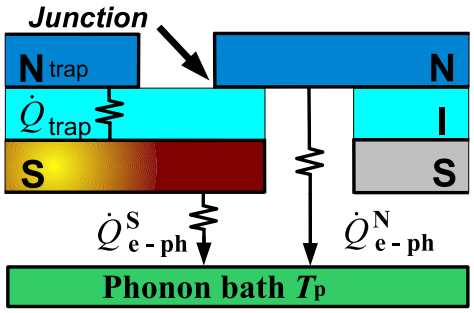

Figure 6.6: Thermal diagram of the NIS thermometer. This schematic does not reflect the real thicknesses of the materials. In this thermal model we assume the normal metal shadow that acts as the trap to be at T_{bath}.

Here, the conductance of the trap per unit area is the same as for the tunnel junction $\sigma_T = 1/(R_T A)$. Therefore, the heat removed per volume by this trap $\dot{q}_{\text{trap}}$ can be calculated using Eq. (6.5) at $V = 0$, $T_N = T_{\text{bath}}$ and substituting R_T by d_S/σ_T. Thus, we derive the temperature of the superconductor T_S from Eq. (6.6) in 2D in polar coordinates using radial approximation for the sample geometry, which can then be written as [183]

$$\sqrt{\frac{2\pi k_B T_S}{\Delta(T_S)}} \exp\left(\frac{-\Delta(T_S)}{k_B T_S}\right) \equiv \alpha \dot{Q}^S_{\text{NIS}} \,. \tag{6.8}$$

Here, we assume $\dot{Q}^S_{\text{NIS}} \approx IV$, and $\alpha = \sqrt{\pi} e^2 G/[d_S \sigma_{Al} \sqrt{2 k_B T_S \Delta^3(T_S)}]$ is a coefficient that depends on T_S and the dimensionless parameter $G = \ln(\lambda/r_0)/\theta \approx [2..3]$ is logarithmically dependent on the sample geometry [183]. Here, λ is the relaxation length of the order of $\sim [10..100]\,\mu\text{m}$, and $r_0 = 2A/(\pi d_N) \simeq 500\,\text{nm}$ is the radius of the contact in the present device. After substitution of all the parameters, we find that the superconductor temperature T_S does not influence the thermometer reading, as $T_S \lesssim 250\,\text{mK}$ in the subgap bias range $|V| \leq \Delta/e$. We estimate T_S to be $\sim 145\,\text{mK}$ in this bias range at $T_{\text{bath}} = 3\,\text{mK}$ corresponding to the power injected to the superconductor as $IV \sim 90\,\text{fW}$, and the quasiparticle density [183] as $n_{qp} = 0.3\,\mu\text{m}^{-3}$. In addition, we evaluate the relative change of the slope to be small $|t| \lesssim 5 \cdot 10^{-3}$ at $I \lesssim 1\,\text{nA}$. In conclusion, the temperatures obtained from both methods A and B are affected by less than 0.5 % by self-heating of the superconductor.

Self-Heating of the Normal Metal

For self-heating of the normal metal, one can solve the diffusion equation (6.6), taking into account the same boundary condition as above with all S indices replaced by N, where $\kappa_N = L_0\sigma_{Cu}T_N$ is the thermal conductivity of the normal metal, and the electrical conductivity of Cu is assumed to be $\sigma_{Cu} = 5{\cdot}10^7\,(\Omega\mathrm{m})^{-1}$ [185]. The heat absorbed in the normal metal is $u_N = \dot{q}^N_{e-ph} + \dot{q}^N_{\mathrm{wire}}$. The heat conduction through the gold bonding wires $\dot{q}^N_{\mathrm{wire}}$ is taken into account only at the point where it is attached to the normal-metal pad, whereas the electron-phonon interaction $\dot{q}^N_{e-ph}$ is effective in the full volume of the normal metal. The volumetric electron-phonon power is $\dot{q}^N_{e-ph} = \Sigma_{Cu}(T_N^5 - T_p^5)$, where $\Sigma_{Cu} = 2\cdot10^9\,\mathrm{W\,K^{-5}\,m^{-3}}$ is the electron-phonon coupling constant of copper. Here, we consider the effect of the heat removed by the bonding wires on temperature only in the normal metal, thus, $\dot{q}^N_{\mathrm{wire}} = L_0\sigma_{Au}(T_N^2 - T^2_{\mathrm{bath}})/2L_{\mathrm{wire}}d_N$. The length of the gold bonding wire is $L_{\mathrm{wire}} \simeq 5\,\mathrm{mm}$ and $\sigma_{Au} = 1.8\cdot10^9\,(\Omega\mathrm{m})^{-1}$ is the electrical conductivity of gold measured at low temperatures. The thermal relaxation length in the normal metal [149] is

$$l_N = \left(T^{p/2-1}_{\mathrm{bath}}\right)^{-1}\sqrt{\frac{\sigma_{Cu}L_0}{2\Sigma_{Cu}}}\,. \tag{6.9}$$

We substitute $p = 5$ and $T_{\mathrm{bath}} = 10\,\mathrm{mK}$ and obtain $l_N = 17.5\,\mathrm{mm}$. Since all the dimensions of the present device are smaller than 1.5 mm, there is only a weak temperature gradient over the normal-metal electrode due to its good heat conduction, and the weak electron-phonon coupling at low temperatures. By solving the heat-balance equation $\dot{Q}^N_{\mathrm{NIS}} = \dot{Q}^N_{e-ph} + \dot{Q}^N_{\mathrm{wire}}$ and assuming no external heat leaks, one can calculate T_N. Here, the heat released through electron-phonon coupling is $\dot{Q}^N_{e-ph} = \Omega_N\dot{q}^N_{e-ph}$, where $\Omega_N = A_Nd_N$ is the volume of the N electrode. The heat released through $N_{\mathrm{wire}} = 2$ bonding wires is $\dot{Q}^N_{\mathrm{wire}} = \dot{q}^N_{\mathrm{wire}}N_{\mathrm{wire}}A_{\mathrm{wire}}d_N$, where its cross-sectional area is $A_{\mathrm{wire}} = \pi r^2_{\mathrm{wire}}$ with a radius $r_{\mathrm{wire}} = 16\,\mu\mathrm{m}$. The temperatures obtained from both methods A and B are affected by less than 0.5 % by self-heating of the nor-

mal metal down to a temperature of 1 mK. In addition, we can evaluate at low temperatures (i.e. $T_N \leq T_S \ll \Delta/k_B$) the maximum cooling at optimum bias voltage $V_{opt} \approx (\Delta - 0.66 k_B T_N)/e$ [149],

$$\dot{Q}^N_{\mathrm{NIS}}(V_{opt}) \approx \frac{\Delta^2}{e^2 R_T}\left[-0.59\left(\frac{k_B T_N}{\Delta}\right)^{3/2} + \sqrt{\frac{2\pi k_B T_S}{\Delta}}\,\exp\left(-\frac{\Delta}{k_B T_S}\right) + \gamma\right] \tag{6.10}$$

to be 90 pW at $T_{\mathrm{bath}} = 1\,\mathrm{mK}$.

7 Adiabatic Nuclear Demagnetization on a Pulse Tube System

Inspired by the progress on cooling nanostructured devices to temperatures below the mixing chamber (MC) temperature of a dilution refrigerator using nuclear refrigerators (NRs) implemented in each separate measurement lead, we started to build a similar AND stage on a cryogen-free system. For all the experiments described in chapters 3 to 5, the time between He transfers (~ 4 days) is severly limiting our scheduling because the AND stage warms up whenever we transfer cryoliquids, in particular liquid N_2. Using a cryogen-free ("dry") system, the time spans for precooling, demagnetization and measurements can be largely extended. Furthermore, the increasing cost of ^{3}He and ^{4}He in recent years boosted the augmented usage of cryogen-free systems that can be run without He liquefaction plant, such that the question arises if ultra-low temperature experiments using AND are also feasible on these systems.

The implementation of a dilution refrigerator (DR) based on a dry cooler (Gifford-McMahon) has been realized decades ago [186], but only recent developments of the pulse tube (PT) cooler [56] achieved heavily decreased vibrations levels [187, 188] and made this combination a success. For AND experiments in particular, the precautions to create a low vibration environment in order to reduce heat leaks are even more severe. Consequently, the realization of a working AND system based on a cryogen-free DR is very challenging and requires a carefully designed system – starting from the laboratory environment down to the nuclear stage and the chip carrier.

Recently, successful AND on a PT system using $PrNi_5$ as refrigerant has been reported by Batey *et al.* [189]. The first article presenting a Cu nuclear stage on a cryogen-free system was published by Todoshchenko *et al.* [190] in 2014.

A typical, commercially available cryogen-free DR utilizes a two-stage pulse tube to generate a temperature of $\sim [3..4]$ K that in a conventional wet system is provided by

the liquid He bath. Since the liquid He bath in the experiment Dewar is completely absent in a dry system, there is no fuel for the 1 K-pot and thus the incoming He gas can not be efficiently precooled to facilitate condensation. This problem was resolved by increasing the condensing pressure (in the early times to 5 bar, nowadays to roughly 2 bar) using a small compressor. In continuous operation of the DR, the gas in the condensing line is efficiently cooled through high-performance heat exchangers and the compressor is not needed anymore.

A further advantage of dry systems is the large experimental space available on all flanges down to the MC, often with a diameter of several hundred millimeters. Whereas in wet systems, the diameter of the insert is constrained by the neck of the Dewar, which influences the rate of liquid He boil-off, this restriction does not apply for dry systems. This facilitates the installation of extensive filtering stages, cryogenic amplifiers or microwave components for sophisticated experiments.

Our AND stage is housed in a LD-400 cryogen-free dilution refrigerator from BlueFors [191] with a cooling power of 415 µW at 100 mK and a base temperature of $T_{\mathrm{base}} \approx 6.5\,\mathrm{mK}$. This commercially available system provides a spring-loaded cold-head to damp vibrations. In addition, the first and second stage of the PT (cooling power: 40 W at 45 K, 1.5 W at 4.2 K [192]) are thermalized to the respective flanges by massive but relatively soft C-shaped Cu braids in order to reduce mechanical coupling. The system further includes a dry magnet system consisting of a 150 mT magnet for the operation of the Al heat switches and two 9 T magnets for the NR stage and the sample, respectively. The magnet assembly weighs approximately 120 kg and is anchored to the second stage of the pulse tube. High-T_c superconducting magnet leads reduce the heat load on the 4 K flange [191]. In our experimental setup, the remote motor is situated on a separate rigid platform, decoupled from the refrigerator and therewith intended to damp the vibrations originating from the PT compressor and remote motor. Systems with a top- or bottom-loaded sample socket present additional challenges we wanted to avoid here. For this reason, the whole magnet assembly has

to be cooled from RT to 4 K in every cooldown, which expands the cooldown time from RT to T_{base} to roughly 100 h.

The refrigerator is placed on a pneumatically damped tripod table ($m \approx 350\,\mathrm{kg}$). The vibrations from the gas handling system are attenuated by a 150 kg concrete block placed on one of the table legs. Moreover, vibrations transduced by the rigid ISO-100 still pumping line are additionally damped by a horizontal and a vertical damping element from VAT.

7.1 Design

This chapter is intended to describe the design and assembly of the NR stage with all its components in detail. The nuclear stage is designed following the approach of the previously tested system in a wet cryostat, as described in chapters 3 to 5 and Refs. [47, 48]: a copper NR is integrated in each of the sample wires, providing efficient thermal contact of the sample to a bath at low mK and potentially even microkelvin temperatures. However, to address the increased vibration levels of a dry system, several features have been adapted in order to facilitate successful AND experiments.

To give the reader a detailed picture of the setup, the entire pathway of an exemplary measurement lead from the RT flange down to the nanostructured sample will be described here. The complete system consists of 16 measurement wires, accompanied by several twisted pair wires used for thermometry. The nuclear stage is shown schematically in Fig. 8.1 on page 113. A similar picture for the prototype stage is presented in Fig. A.1, indicating the thermal resistances involved.

The connection from the RT flange of the refrigerator down to the MC flange is conducted by thermocoax cables with a length of roughly 1.5 m. Since the thermocoax itself acts as a low-pass microwave filter [66], this wiring represents a first albeit very slack filtering stage ($> 100\,\mathrm{dB}$ for $f > 3\,\mathrm{GHz}$). The bundle of thermocoax wires is thermalized at each of the experimental flanges including the MC plate (diameter:

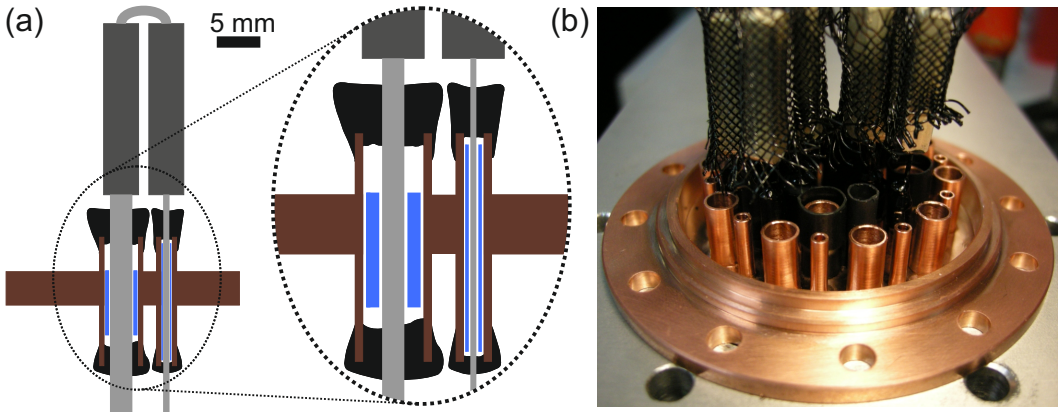

Figure 7.1: The adapted MC bottom piece including 34 feedthroughs and sinters. (a) Schematic describing the super-fluid leak-tight feedthroughs. The Ag wires (light gray) are insulated from the Cu body by PTFE tubes and tape (blue) for the large and small feedthroughs, respectively. Epoxy is poured into cup-shaped molds surrounding the Cu tubes and Ag wires inside and outside the MC. The sinters (dark gray) are additionally insulated using a black netting (not shown in (a)). (b) Photograph of the mixing chamber bottom in an intermediate building state: Bare Cu tubes are visible in front and tubes equipped with shaped heat shrink tubing to pour the epoxy in the cup-like shape depicted in (a) in the middle section. At the back, there are three complete sinter pairs.

290 mm) [191]. Then, by traversing through a home-made Ag epoxy filter [65], the wire enters a radiation-shielded space defined by the MC flange and the MC radiation shield. After passing a two-stage RC filter (2 kΩ / 680 pF, 2 kΩ / 680 pF, $f_{3\mathrm{dB}} = 45$ kHz) mounted on a printed circuit board and bolted to the bottom of the MC flange, it enters the copper MC as a thin Ag wire. The MC has a diameter of 48.5 mm and comprises 34 sintered heat exchangers (2 x 16 for the leads +2 spares), fabricated in-house following a recipe from Ref. [63] using a Ag powder with particle size $\sim$ 150 nm and purity 3N5. Each sinter has dimensions of [4 x 4 x 20] mm^3 and its surface area was measured as $\sim 4.5\,\mathrm{m}^2$ using the BET method [193]. An annealed Ag wire connects two sinters on top to a pair. The thin Ag wire entering the MC is molded in the bottom of one of these two sinters and exits the MC at the bottom of its partner as a massive silver wire, see Fig. 7.1. These silver wires have a diameter of 2.54 mm, a purity of 5N (99.999 %) and were annealed at 800° C for 8 hours, resulting in RRR > 1′500.

It should be mentioned that it is a formidable challenge to accommodate as many sinters on a small volume and making 34 superfluid leak-tight feedthroughs with a

rather large diameter in a (conductive) Cu mixing chamber, in particular because every measurement lead must be electrically isolated from all the others and from ground to enable transport measurements. After several unsuccessful attempts, this was achieved by pouring the epoxy (Stycast 2850) into cup-shaped molds made from heat shrink tubing for every single feedthrough, as indicated in Fig. 7.1. The Cu tube with a total length of 15 mm and wall thickness 0.5 mm are milled out of one massive Cu piece. The Ag wire are partially insulated using PTFE to avoid electrical shorts to the MC body.

The annealed silver wire is then fused into a C-shaped aluminum heat switch (HS) [61]. The HS has a cross-sectional area of $[4\,\mathrm{x}\,3]\,\mathrm{mm}^2$ and an arc length of approximately 22 mm. It has a purity of 5N and was annealed at 480° C for 6 h, resulting in RRR $\approx$ 100. The magnetic field B_{HS} from the HS magnet, which is part of the magnet assembly, is used to switch between the thermally conducting state (Al normal conducting, $B_{\mathrm{HS}} = 15\,\mathrm{mT}$) and the thermally insulating state (Al superconducting, $B_{\mathrm{HS}} = 0$), see chapter 2.1.1. The heat switches are placed on a fixed radius in order to minimize inhomogeneities in magnetic field. Due to poor field canceling, B_{HS} has to be compensated for the stray fields of the demagnetization magnet, particularly during the precooling and demagnetization process. At the bottom end of the C-shaped HS, another annealed silver wire is fused into the aluminum and connects the HS to the Cu plate, the heart of the AND stage.

Small tabs on the upper and the lower end of each copper NR allow for spot-welding of the large-diameter silver wires. Each of the 16 plates measures $[2\mathrm{x}(34\text{ x }1.7\text{ x }120)]\,\mathrm{mm}^3$ and consists of roughly 2 mol of NOSV Cu with a purity of 4N. We doubled the amount of Cu per plate compared to the wet system while at the same time eddy current heating is reduced by spot-welding two half plates at their corners, i.e. reducing the area that is critical for $\dot{Q}_{\mathrm{eddy}}$. The copper has a RRR of 480 and was not annealed, resulting in $\dot{Q}_{\mathrm{eddy}} = 2.8\,\mathrm{nW/mol}$ for $\dot{B} = 1\,\mathrm{T/h}$ calculated using Eq. (2.14). The nuclear stage with a total weight of $\sim 2\,\mathrm{kg}$ is placed in the center of the demagnetization field B,

roughly 460 mm below the MC flange. To prevent displacement of the NR assembly, the plates are rigidly bound together and attached to a Ag support structure using two PTFE screws and dental floss. The support structure is thermalized to the MC flange via annealed silver wires. Electrical and thermal insulation between the NRs is ensured by thin PTFE washers of 6 mm outer diameter, 2.6 mm inner diameter and 0.5 mm thickness. The rigid support structure composed of two Ag rings close to the NR stage and of two standard ETP Cu rings above is a key ingredient to minimize relative vibrations between the magnet and the AND stage. All of the rings are slitted to impede eddy current heating and Au-plated to facilitate thermal anchoring to the MC flange.

Out of the 16 NRs, three are chosen for thermometry purposes. The three electron thermometers, a CMN, a LCMN and the gradiometer of the noise thermometer, which is described in chapter 7.2, are situated in the field-cancelled region next to the heat switches, connected to the three NRs via an annealed Ag wire. Each of these three NRs also features a resistive heater (strain gage, NiCr thin film resistor, 120 Ω) to apply a controlled, additional amount of heat $\dot{Q}$ and therewith facilitate thermometry experiments.

The center of the sample magnet is 300 mm below the center of the demagnetization magnet. To overcome this distance, an annealed Ag wire connects the lower end of the NR to a Ag epoxy (EPO-TEK E4110) filter anchored in a Ag epoxy chip socket [194], which is supported by three Vespel SP-22 rods, see Fig. 7.2. These Ag epoxy filters are a little shorter ($R = 3.5\,\Omega$ at RT, number of windings $N = 400$, RRR ≈ 135) than the ones used at the MC flange. However, these filters are twice as long as the filters used for the sample socket in the wet system. The wire exiting the filter then directly connects to a Au-plated metal pin, providing a platform for an easily removable chip carrier. The resistance of the pin-to-pin press contact was measured to be $\sim 2.6\,\mathrm{m}\Omega$ at RT with a RRR of ~ 3, strongly depending on the strain applied on the contact.

Very similar to the chip socket, also the chip carrier consists of Ag epoxy. The Au-

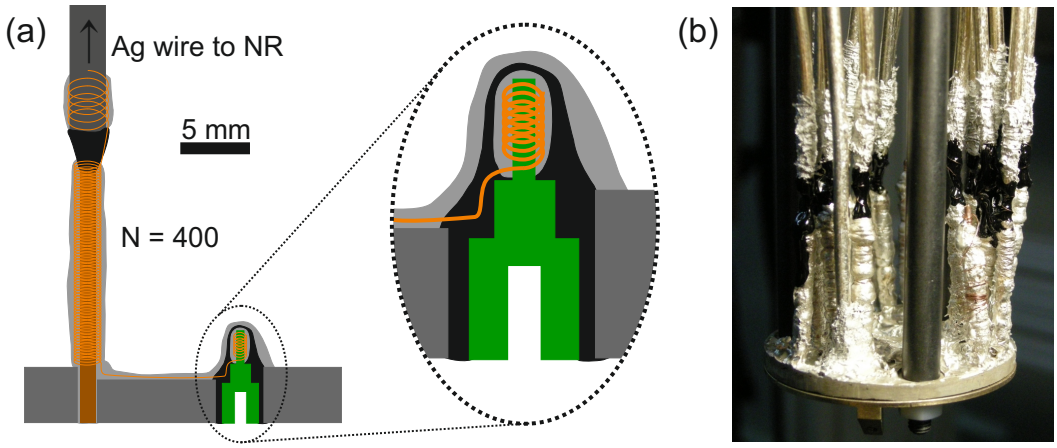

Figure 7.2: Schematic (a) and photograph (b) of the filtered Ag epoxy sample socket in the dry system. The Cu wire (orange) of the Ag epoxy filter (light gray) is stripped on top and wound on the Ag wire which is spot-welded to an NR. To thermalize the filters and the sample socket, one NR is directly connected to the Ag epoxy body (as shown in (b), front left), whereas all other leads are conducted to a Au-plated brass pin (green) inside the Ag epoxy, insulated with tiny amounts of black epoxy (black). In panel (b), one of the three brownish Vespel rods is visible.

plated pins are isolated from the conducting bulk using black epoxy (Stycast 2850). After polishing the pins with sandpaper, the sample is glued to the chip carrier with Ag paint and the sample contacts are wedge-bonded with Au wire ($\varnothing = 32\,\mu m$) directly to the pins. In order to expel electromagnetic radiation, a conical piece of Ag foil is glued with Ag paint to the chip socket, creating a Faraday shield around the sample.

In summary, the design of the dry AND stage follows the idea of the second generation in the wet system, with three major exceptions:

- The thermal conductance between the NR and the MC has been improved by doubling the diameter of the Ag wire as well as the surface area of the sinters per lead. Furthermore, a larger HS cross section is used to increase the efficiency of the precooling process.

- The geometry of the NRs has been adapted to address the increased vibration levels in PT systems compared to wet systems. Here, we use twice the amount of Cu per NR while reducing the eddy currents at the same time, potentially increasing the hold time for long experiments.

- The length of the Ag epoxy filter at the chip socket is doubled with the intention to increase the quality of the radiation shielding around the sample.

However, stronger filtering at the chip socket also increases the thermal resistance between the sample and the AND stage. For 2DEG samples, the ohmic contacts (Schottky barriers of the metal-semiconductor interface) represent the largest electrical resistances and therewith the weakest thermal links to the NR. But for different samples like e.g. NIS devices, where the contact to the electron reservoir is of low resistance, even the finite resistance of the filters and pins can entail a substantial temperature gradient for a given heat leak.

7.2 Magnetic Field Fluctuation Thermometry

In 1928, Johnson and Nyquist published experiment [195] and theory [196], respectively, of the thermal agitation of electrons in a conductor. They both found that the power spectral noise density V^2_{noise} generated by a resistor shows a behavior described by

$$V^2_{\text{noise}} = 4k_B T R \Delta f, \tag{7.1}$$

where k_B is the Boltzmann constant, R the resistance and Δf the measurement bandwidth. From this relation, we see that V^2_{noise} depends linearly on temperature, facilitating the possibility to use the noise as an easy and theoretically even primary thermometer.

As it was discussed in previous chapters, the importance of reducing heat leaks gets increasingly essential when approaching low temperatures. Even tiny heat leaks in the order of nW to pW arising from various sources (see chapter 2.1.4) can give rise to increased temperature readings. Particularly in thermometers, this effect is very undesirable. The problem of Joule heating can be avoided by using passive devices as for example a noise thermometer. Among other realizations of noise thermometry [197],

I would like to review the Magnetic Field Fluctuation Thermometer (MFFT) based on a DC SQUID (Superconducting QUantum Interference Device) [198, 199]. Here, in contrast to current sensing noise thermometry (CSNT, Johnson noise thermometer) [200, 201], the noise sample is not in electrical contact with the input loop of the SQUID: the thermal (Brownian) motion of electrons in a noise sample is picked up inductively by a superconducting coil wound around the noise source. In such a temperature probe, parasitic heat generated by SQUID back-action and thermal conductance through the superconducting wires and shields can theoretically be reduced to several femtowatts for a completely contactless design [202, 203].

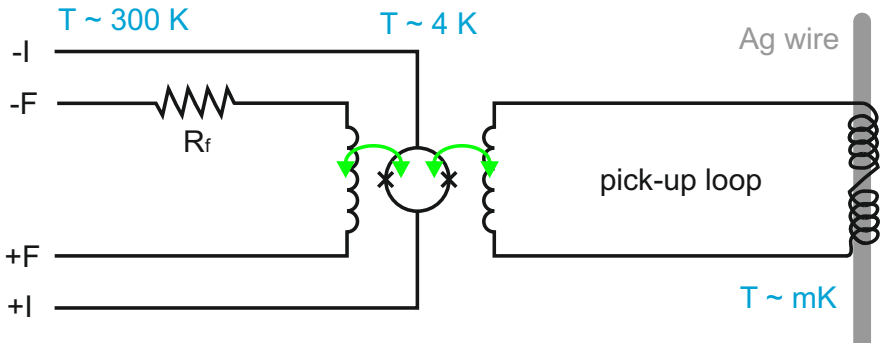

Figure 7.3: Simplified scheme of the MFFT setup. The bias current is fed through the SQUID via terminals +I/-I. The pick-up loop transfers the flux induced by the Brownian motion of the electrons in the Ag wire to the SQUID. In flux-locked loop (FLL) mode, the working point of the SQUID is fixed by canceling any change in flux from the pick-up loop by a matching flux with opposite sign (green arrows) from the feedback circuit (+F/-F). The voltage across the feedback resistor R_f is measured and Fourier transformed to obtain a noise spectrum. The temperature range of every stage of the thermometer is indicated in blue.

The home-built noise thermometer setup used in this experiment is shown schematically in Fig. 7.3. The pick-up loop consists of two coils with 20 windings each and is wound on a large diameter silver wire which is spot-welded to a NR, thus creating a thermal contact between the noise source and the pick-up coils. To eliminate problems arising from static magnetic fields, these two coils are wound non-inductively: the upper one is wound clockwise and the lower one counterclockwise. This “gradiometer” configuration leads to a cancellation of induced voltage noise that is picked up e.g. by mechanical vibrations in an inhomogeneous magnetic field. A schematic of the gradiometer inside

the refrigerator is illustrated in Fig. 8.1 (page 113).

The two coils of the flux transformer pick up the magnetic noise caused by the thermal fluctuations of the electrons in the silver wire. This extremely small noise signal is then amplified by a SQUID, which is bolted to the 4 K-flange, and Fourier transformed at room temperature. To assure an effective electromagnetic coupling between sensor loop and SQUID, the pick-up loop has to be superconducting. For this reason, the coils are wound using 99.8 % Nb wire with a diameter of 100 µm. Because even tiny fluctuations in magnetic field, which can be in the order of the Earth's magnetic field or less, will entail parasitic voltage noise, the sensor as well as the twisted wires to the SQUID have to be shielded very well. Since large magnetic stray fields are present in our experiment setup (up to 50 mT in the path from the gradiometer to the SQUID), a double shield consisting of an inner Nb tube and an outer NbTi tube is used, the latter because of its higher critical field.

To amplify those tiny voltage fluctuations, a commercially available niobium-based DC SQUID with XXF-1 electronics [204] is used as a flux-to-voltage converter: while the SQUID is biased with a current $I_{\mathrm{bias}} \approx 10\,\mu\mathrm{A}$ slightly above its critical current I_c through +I/-I , the working point of the SQUID is fixed by a feedback loop (terminals +F/-F in Fig. 7.3). Therefor the voltage V across the SQUID is amplified, integrated and fed back to the SQUID through the feedback circuit. The intention of this so-called flux-locked loop (FLL) mode is to increase the dynamic range of the SQUID [205]. For the calibration of the working point, we drive a certain amount of flux Φ_a through the SQUID using the feedback circuit and measure the oscillation in V. The steepest slope in the $V - \Phi_a$ curve is then used as a working point because it assures a maximum sensitivity to changes in external flux. In FLL mode, the voltage V_f dropping across the feedback resistor R_f is then directly proportional [205] to the change in flux through the SQUID induced by the Brownian motion of the electrons in the Ag wire. Therefore by measuring a time trace of this signal and subsequent Fourier transformation, a noise spectrum can be acquired.

The spectrum of a noise thermometer consists typically of a constant noise region below a critical frequency f_c, which can be attributed to the constant resistance of high-purity metals below a few kelvin [60]. A theoretical view on capacitive and inductive noise thermometers is given in Ref. [206]. For a flux transformer wound on a rod-shaped noise sample with radius r, the cutoff frequency can be written as [203]

$$f_c \simeq \frac{4.5\rho}{\pi\mu_0 r^2\,\mathrm{RRR}} \tag{7.2}$$

with RT resistivity ρ, vacuum permeability μ_0 and residual resistivity ratio RRR. This allows for adjusting f_c by choosing a noise sample with appropriate ρ, RRR and r [207], as described in more detail in chapter 8. A large f_c (i.e. a broad plateau) also allows for fast measurements, but considering the large time scales involved in AND, we favor a large signal amplitude. For $f > f_c$, the attenuation roughly follows a low-pass filter like behavior (20 dB/dec). However, the exact behavior depends on the geometry of the gradiometer as well as the wiring, because the inductances involved determine the coupling efficiency of the flux transformer into the SQUID. By reason of this major complication, we follow the approach of Ref. [208] and operate the MFFT as a secondary thermometer by acquiring a reference noise level $S_0(T_{\mathrm{ref}})$ at a known temperature T_{ref}, often before condensing the mixture between 3.5 and 4.2 K. In order to get reasonable fits, we have to eliminate noise peaks arising from electromagnetic interferences (EMI) from our spectra, because the temperature-independent noise spoils the performance of our thermometer, which relies on the thermal noise. To clean our spectra, we first fit a polynomial of 10^{th} order to the FFT spectrum. In a second step, all noise peaks extending more than 1.3 times the standard deviation over the polynomial fit are cut out of the spectrum. This cleaned spectrum is then fitted with the low-pass-like equation

$$S_\Phi(f, T_{\mathrm{noise}}) = \frac{S_0(T_{\mathrm{noise}})}{\sqrt{1 + \left(\frac{f}{f_c}\right)^2}}\,. \tag{7.3}$$

For the reference spectrum, $S_0(T_{\mathrm{noise}})$ and f_c are fit parameters. From this fit, we extract $f_c = 7.5\,\mathrm{Hz}$ and a corresponding $S_0(T_{\mathrm{noise}}) = S_0(T_{\mathrm{ref}} = 3.98\,\mathrm{K}) = 8'457 \pm 77\,\mu\Phi_0^2/\mathrm{Hz}$ for our noise thermometer setup, see Fig. 7.4. Along with the reference spectrum, we plot two other exemplary spectra at $T_{\mathrm{Cu}} = 98\,\mathrm{mK}$ (green trace) and $T_{\mathrm{Cu}} = 7.3\,\mathrm{mK}$ (blue trace), where f_c is fixed to the value found for the reference spectrum and $S_0(T_{\mathrm{noise}})$ remains the only fit parameter. Since we perform a "magnitude square" Fourier transform, we obtain $\mu\Phi_0^2/\mathrm{Hz}$ (or V^2/Hz before multiplying with the voltage-flux transfer coefficient) and thus a linear scaling of temperature with the voltage noise density. The temperature T_{noise} for a given measured noise amplitude $S_0(T_{\mathrm{noise}})$ is then defined as

$$T_{\mathrm{noise}} = \frac{S_0(T_{\mathrm{noise}})}{S_0(T_{\mathrm{ref}})}\, T_{\mathrm{ref}}\,. \tag{7.4}$$

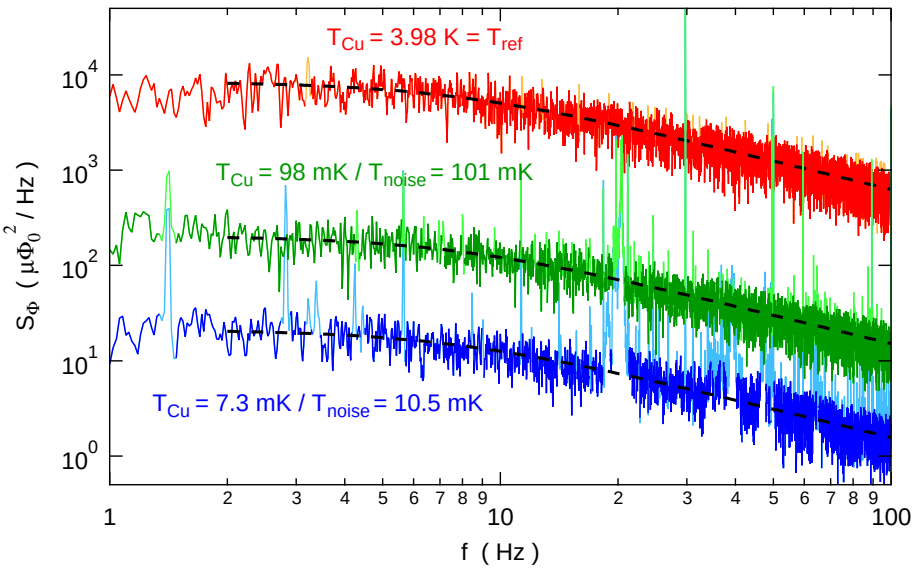

Figure 7.4: Exemplary noise spectra at three different NR temperatures $T_{Cu} = 3.98\,\mathrm{K}$ (reference), 98 mK and 7.3 mK from top to bottom. Noise peaks arising from EMI interferences are cut (original data: orange / cleaned: red, analogously light-green / green, light-blue / blue) by fitting a polynomial (see text) before fitting the data using Eq. (7.3) with fixed $f_c = 7.5\,\mathrm{Hz}$ (black dotted lines). From the fit parameter $S_0(T_{\mathrm{noise}})$, we calculate noise temperatures of 101 mK and 10.5 mK, respectively, using Eq. (7.4) with $T_{\mathrm{ref}} = 3.98\,\mathrm{K}$.

Similar to the vibration spectrum in Fig. 7.8 (see page 106), the resonances of the PT

remote motor appear in the electrical noise at low temperatures, see Fig. 7.4. In general, the EMI noise peaks become more visible with decreasing temperature, because the environmental noise gets comparable to the noise picked up by the flux transformer.

The performance of the MFFT is shown in Fig. 8.3 (page 117) by plotting the extracted T_{noise} versus the temperature of the nuclear stage T_{Cu} in a range of [0.7..200] mK. 700 µK is currently the lowest temperature reading of our MFFT, possibly limited by the influence of excess EMI noise or a residual heat leak. By taking $T_{\mathrm{ref}} \approx 4\,\mathrm{K}$. into consideration, the MFFT provides a reliable reading over roughly three orders of magnitude.

To reduce effects from EMI, we plan to additionally shield the cryocable connecting the SQUID to the room temperature electronics and probably reinforce the shielding for the superconducting twisted wires between the gradiometer and the SQUID. However, the long distance between the gradiometer and the SQUID complicates shielding and thermalization of the wires.

7.3 Performance

Figure 7.5 compares the precooling of the dry and the wet system. After the field was ramped to $B_i = 9\,\mathrm{T}$, the NR stage in the dry system cools from 35 mK to 17.9 mK within $t_1 = 10\,\mathrm{h}$ and to 12.6 mK within $t_2 = 40\,\mathrm{h}$. Compared to the wet system ($T_e(t_1) = 20.1\,\mathrm{mK}$, $T_e(t_2) = 13.6\,\mathrm{mK}$), the efforts of increasing the thermal conductance between NR and MC show a clearly increased efficiency of the precooling process despite doubling the amount of Cu per wire. The total amount of copper in the NR assembly is almost 1.5 times larger in the dry system (16 x 2 mol, amounting to $\sim 1.98\,\mathrm{kg}$) compared to the wet system (21 x 1 mol, amounting to $\sim 1.33\,\mathrm{kg}$).

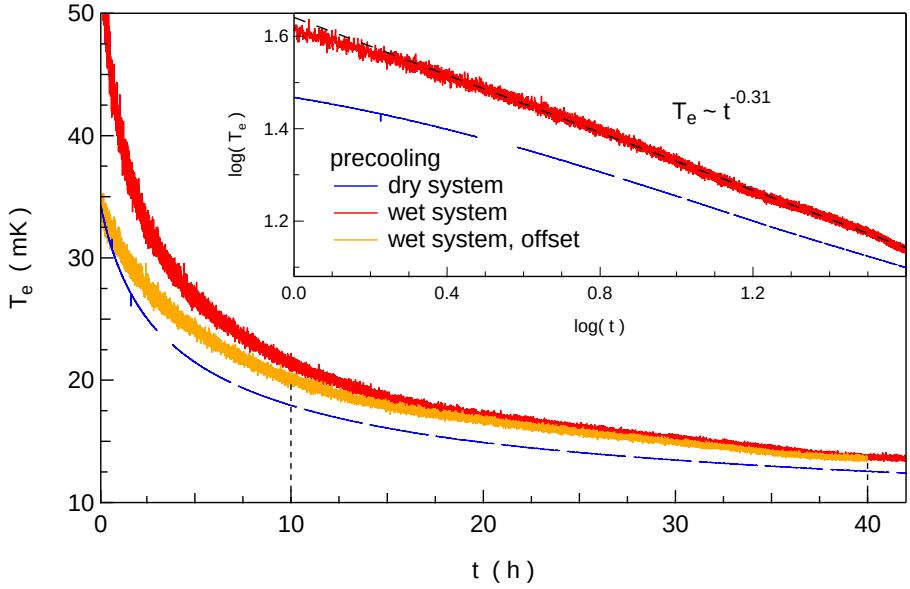

Figure 7.5: Comparison of the precooling process in the dry and the wet system. The blue trace shows a typical precooling in the dry system measured with a CMN thermometer, where the gaps arise from MFFT measurements. The red curve represents the precooling in the wet system, the orange trace is offset in time (−2 h) for a proper comparison of the cooling power. *Inset:* Log-log representation of the same data.

An exemplary AND run is shown in Fig. 7.6 including demagnetization in panel (a) and warmup in panel (b). While the field is ramped down from $B_i = 9\,\mathrm{T}$ to $B_f = 1\,\mathrm{T}$, the LCMN and the CMN thermometer cool from $T_i = 12.9\,\mathrm{mK}$ and 12.3 mK, respectively, to roughly 3.4 mK and 4.3 mK. The MFFT is not measured while the AND field is ramped because the working point can not be locked. As soon as we reach B_f, we apply a finite heating power of $\dot{Q} = 50\,\mathrm{nW/mol}$ to each of the three NRs to which the thermometers are connected using strain gages, following the warm-up method discussed in chapter 2.3. We extract the final temperatures at the end of the AND process for the LCMN, the CMN and the MFFT, respectively, as $T_{e,f} = 1.79\,\mathrm{mK}$ / 1.88 mK / 1.67 mK. The heat leaks extracted from the slope of the linear fits (solid lines in Fig. 7.6(b)) agree within 10 % with the applied heat.

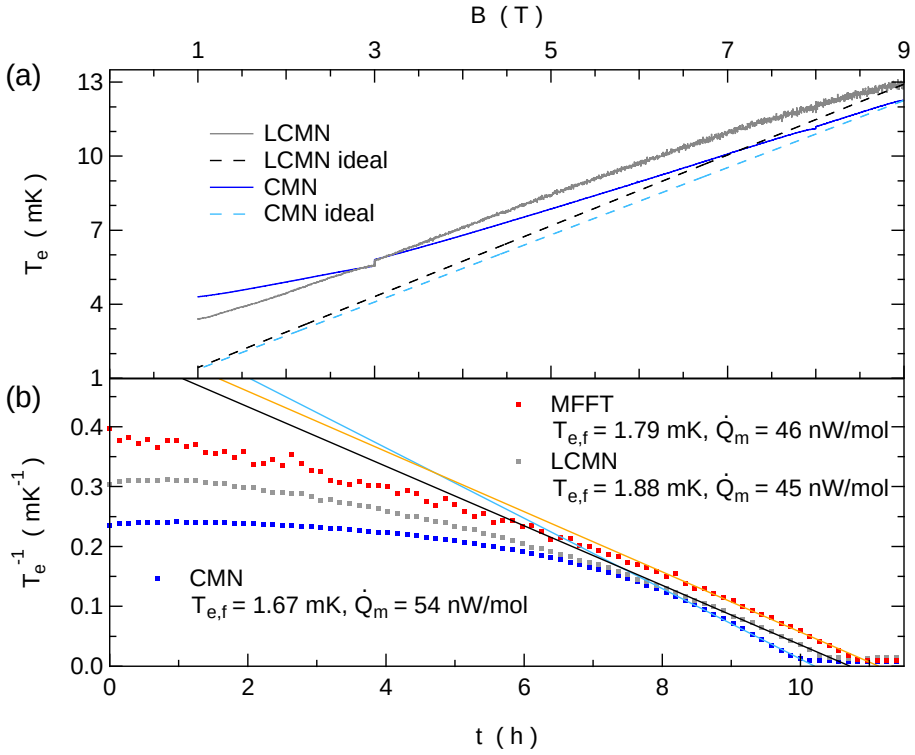

Figure 7.6: AND run of the Cu stage in the dry system with a CMN (blue), a LCMN (gray) and the MFFT (red). (a) Demagnetization from $B_i = 9\,\mathrm{T}$ to $B_f = 1\,\mathrm{T}$. The cooling at 8 and 3 T arises from 30 min breaks where $\dot{B} = 0$. The dotted lines indicate ideal adiabatic cooling, i.e. an efficiency of $\xi = 100\,\%$. (b) After the demagnetization stops, a heat of $\dot{Q}_m = 50\,\mathrm{nW/mol}$ is immediately applied on each of the three thermometer NRs using strain gages. Using Eq. (2.27) we perform linear fits to the data (solid lines) in a regime of [6..50] mK for the MFFT and [8..50] mK for the LCMN and CMN. For the MFFT, the LCMN and the CMN, respectively, we extract $T_{e,f} = 1.79\,\mathrm{mK}$ / $1.88\,\mathrm{mK}$ / $1.67\,\mathrm{mK}$ and $\xi = 81\,\%$ / $76\,\%$ / $82\,\%$.

Since the warm-up time is inversely proportional to the applied heat, we can estimate that the warm-up times would be roughly a factor of 10 larger for our residual heat leak, which is in the order of [3..5] nW/mol (see Fig. 7.7). The hold time below 4 mK at $B_f = 1\,\mathrm{T}$ is therefore [2..3] days, if no additional heat is applied, and the bath temperatures are still sufficiently low for many experiments. Although the values for the residual heat leak are far from the state-of-the-art values of 5 pW/mol [64], they allow for AND experiments and hold times below 1 mK of roughly 1 day for $B_f = 0.2\,\mathrm{T}$ and $T_f \approx 300\,\mu\mathrm{K}$, see Fig. 8.4 on page 120.

Another method to extract heat leaks without the need to perform a complete AND

is shown in Fig. 7.7. After the NRs were precooled in a static magnetic field B, the HS are opened and the electron temperature in the NRs starts to increase due to a finite heat leak. Since the signal amplitude is much smaller for the LCMN, the noise is clearly increased as compared to the CMN. As indicated by Eq. (2.24), the warm-up time is proportional to B_f^2. The equilibrium temperature, where the heat leak equals the heat flow through the heat switch, is $\sim 50\,\mathrm{mK}$ for the CMN as well as for the LCMN. The heat leaks from both sensors extracted from the linear fits (black dashed lines) at different B are consistently around $4\,\mathrm{nW/mol}$. As opposed to the LCMN, the CMN reading does not follow the linear fits down to the lowest temperatures which indicates the beginning of the saturation regime.

In contrast to the warm-up after demagnetization, where the support structure is most of the time much warmer than the NR stage ($T_{\mathrm{sup}} \approx T_{\mathrm{MC}} > T_{Cu}$), the situation is opposite here ($T_{\mathrm{sup}} \lesssim T_{Cu}$). This could lead to a higher heat leak for the measurement after AND, depending on the fitting range (i.e. a change of the slope in T_e^{-1} versus t). Such a deviation was never observed in our measurements, speaking in favor for the thermal insulation between the NR stage and the support structure. This means that another source must contribute significantly to the heat leak, e.g. heat release, radiation or finite thermal conductance through the heat switches due to flux tubes.

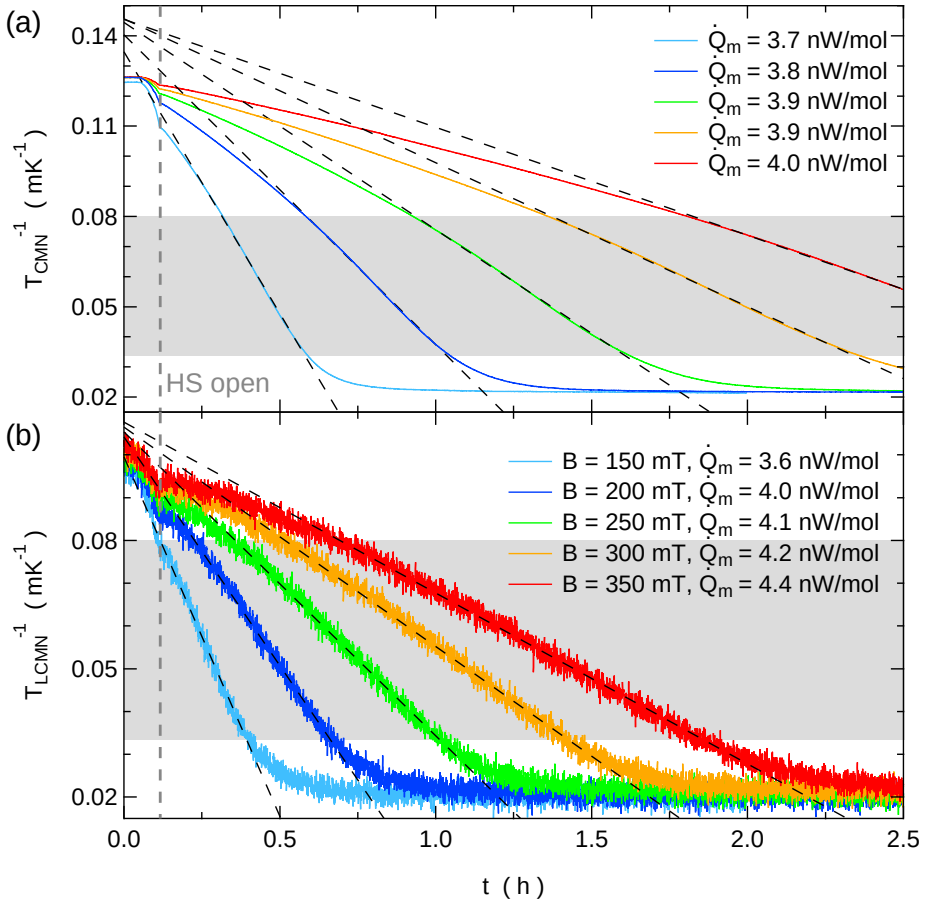

Figure 7.7: Inverse electron temperature versus time for a heat leak measurement at different magnetic fields B from 150 mT to 350 mT. Two different thermometers mounted on two separate NRs are used: (a) CMN and (b) LCMN. The precooling temperatures (at $t = 0$) are roughly 2 mK higher for the LCMN independent of the field, most likely due to a calibration issue. The vertical, gray dotted line at $t = 420\,\mathrm{s} \approx 0.12\,\mathrm{h}$ depicts the end of the heat switch opening process. Linear fits to the data are shown as black dotted lines – the fitting range (gray shaded) is [12.5..30] mK. Using Eq. (2.27), the slopes of the linear fits reveal heat leaks that are consistently in the range of $\dot{Q}_m = 4\,\mathrm{nW/mol}$.

The heat leaks extracted here are considerably larger as compared to the wet system, where we found $\dot{Q}_m \lesssim 1\,\mathrm{nW/mol}$ [47]. Possible reasons will be outlined in the following paragraphs.

As discussed in detail above, the increased vibration level of a PT system could lead to higher heat leaks, either through eddy current heating in finite B or through frictional heating. Figure 7.8 compares the vibration levels of the dry (blue/red trace) and the wet (green trace) system, measured on top of the RT flange for both setups. The

wet system employs a sand box and a concrete block, through which all the lines from the gas handling system (GHS) pass. The only vibration source directly on the pneumatically damped table arises from the boiling nitrogen and helium baths inside the Dewar. In the dry system, all GHS lines run through a concrete block as well and the remote motor of the PT compressor is situated on a rigid platform, separated from the table. However, floating the table of the dry system *increases* the vibration levels substantially (see red trace in Fig. 7.8). In this situation, the flexible tube connecting the remote motor and the PT cold head is "breathing" in the frequency of the remote motor rotation (1.4 Hz) and therewith rocking the table. Furthermore, the He gas inside the PT is compressing and expanding ($p_{\mathrm{low}} \approx 7.5\,\mathrm{bar}$ to $p_{\mathrm{high}} \approx 20\,\mathrm{bar}$), which also leads to mechanical vibrations. For this reason, the dry system is operated with non-floating table, if not stated otherwise. In contrast, floating the table clearly reduces the vibrations in the wet system, especially for $f > 5\,\mathrm{Hz}$ (green trace in Fig. 7.8 – data with non-floating table not shown).

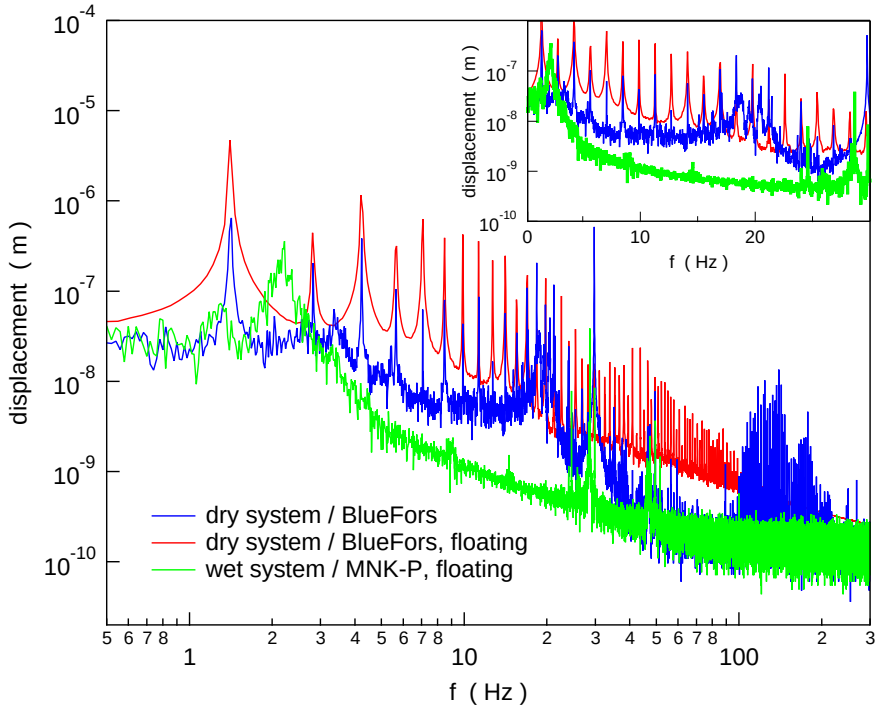

Figure 7.8: Vibration spectra from the dry setup with static table (BlueFors, blue) and floating table (red) as well as the second generation setup in the wet cryostat (green, table floating) on a log-log scale, acquired with a JRS Vibration Analyser. The displacement is increased in the dry setup in the frequency range of $3 - 40\,\mathrm{Hz}$ despite all the efforts to damp vibrations originating from the pulse tube and the gas handling system. Floating the table massively increases the whole vibration spectra. The peaks at $\sim [20..30]\,\mathrm{Hz}$ arise from the scroll pumps that are present in both setups. *Inset:* Zoom in to the low frequency region on a log-linear scale. The resonance at 1.4 Hz and its harmonics are evident, originating from the remote motor.

We emphasize that even sub-nanowatt heat leaks can substantially increase the sample temperature above the NR temperature due to the finite thermal conductance from the sample to the NR. For the dry and the wet setup, we observe a time-dependent heat leak in the temperature readings right after cooldown. However, we are able to measure temperatures in nanostructured samples in the order of 5 mK on the wet system [47] whereas we are currently limited to $[12..15]\,\mathrm{mK}$ in the dry system. Since the lowest temperatures in the NRs through AND are clearly below 1 mK for both systems, the reason for the saturation of the device temperatures has to be a combination of the increased heat leak and the decreased thermal conductance between sample and NR stage, possibly caused by the slightly larger resistance of the longer Ag epoxy filters.

Figure 7.9 shows a measurement of a linear CBT array mounted on a Tufnol-based chip carrier in the sample socket described at the end of chapter 7.1. In this version of the chip carrier, the sample sits on a piece of Au-plated Ag foil which is glued with silver paint to one of the Ag wires connected to an NR. Previous measurements on a Ag epoxy chip carrier produced similar results. The CBT device has a linear configuration and consists of 4 islands in series (i.e. 8 junctions), featuring enlarged cooling fins (volume $\Omega = 40'000\,\mu m^3$ as compared to $\sim 300\,\mu m^3$ for the 2D arrays used in chapter 3). The resistance of each junction is roughly $20\,k\Omega$.

To extract temperatures, we use the δg method at zero voltage bias V_{SD} described in chapter 3 to avoid overheating. The insets of Fig. 7.9 show the temperature evolution on the time scale of hours (left inset) and days (right inset) after cooldown to $T \approx 7\,mK$. In the right inset, we additionally plot two RuO_2 resistors that are glued to two contacts each on the same chip carrier as the CBT array. All of those sensors demonstrate a clear cooling over a time span of days or even weeks.

The saturation temperatures at the end of a long cooldown (~ 6 weeks) are reasonably close to T_{base} for the RuO_2 resistors, but as high as $14\,mK$ for the CBT array. Furthermore, the CBT saturation temperature did not decrease after AND. Similar behavior was found for an NIS sample on the Ag epoxy chip carrier. In the wet system, an NIS and a CBT sample similar to the ones used here were cooled to $T_{NIS} = 7.3\,mK$ (see chapter 6) or below [47] and $T_{CBT} = 6.8\,mK$ [47], respectively, after the Macor sample stage (including socket and carrier – measurements presented in chapters 3 and ref-sec:paperDOT) was replaced by a filtered Ag epoxy sample stage (chapters 5 and 6).

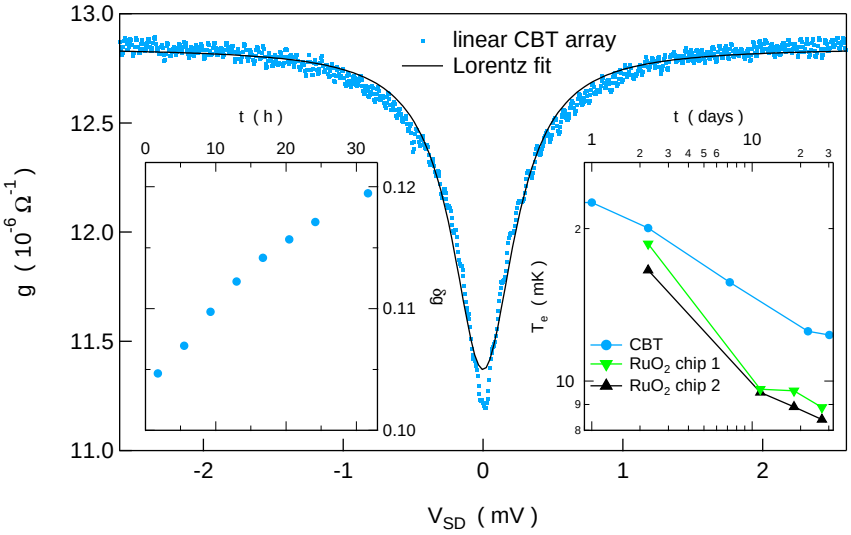

Figure 7.9: CBT measurement at $T_{\mathrm{base}} = 6.5\,\mathrm{mK}$ with $V_{\mathrm{AC}} = 10\,\mu\mathrm{V}$ along with a Lorentz-fit (black line) which indicates overheating at finite bias voltage V_{SD}. The two insets illustrate a decrease of the lowest measured temperatures as a function of time. *Left inset:* Relative depth of the conductance dip $\delta g = 1 - g_{0,\mathrm{min}}/g_T$ versus time t, where $g_{0,\mathrm{min}}$ is the conductance in the dip and g_T is the large-bias conductance. δg can be directly converted to temperature using Eq. (3.1) and $E_C = 17\,\mathrm{mK}$ for this device, avoiding Joule heating in the CBT. In the 32 hours depicted here, the CBT cools from 25 to 22 mK. *Right inset:* Temperature versus time t on a log-log scale of the CBT and two RuO_2 chip thermometers (green and black markers) mounted on the Ag epoxy chip carrier. Lines between points are a guide for the eye. All sensors show a clear cooling over a time span of weeks, indicating a time-dependent heat leak.

As compared to the wet system, the time scales indicated by the right inset of Fig. 7.9 are much longer and the final temperature is much higher for the dry system. These observations suggest two possible scenarios. First, the epoxy used for the chip socket and carrier in the dry system seems to indicate a larger heat release. We used the same kind of epoxy resins (EPO-TEK E4110 and Stycast 2850) although from different batches, but the amount of both, Ag and black epoxy, is a little larger for the dry system. Secondly, the attempt to intensify the filtering stage between the NR and the sample is detrimental to the thermal coupling.

Recently, we found evidence for long time constants in a fractional quantum Hall sample in the wet system. The width of a Reentrant Integer Quantum Hall State (RIQHS), which can be used as a phenomenological thermometer scaling inversely with temperature [28], increases over $2-3$ days right after cooldown, see Ref. [67] for more details.

8 Nuclear Demagnetization on a Pulse Tube Platform for Nanoelectronics

D. Maradan, M. Palma, L. Casparis, T.-M. Liu, D. M. Zumbühl

Department of Physics, University of Basel, CH-4056 Basel, Switzerland

Abstract

We present a parallel network of 16 nuclear refrigerators mounted on a cryogen-free dilution refrigerator setup aimed to cool nanoelectronic devices to sub-millikelvin temperatures. The lowest temperature of the nuclear stage is 280 µK in a final field of 0.2 T and the residual heat leaks are in the order of 4 nW/mol. A home-built noise thermometer measured with a DC SQUID is used to characterize the performance of the nuclear stage together with various other thermometers. The SQUID, mounted on the quasi-4 K flange, inductively picks up the Brownian motion of electrons in a Ag wire which is thermalized to one of the nuclear refrigerators. The lowest temperature measured with the noise thermometer is 0.74 mK, currently limited by either experimental excess noise or a residual heat leak to the sensor.

This chapter is prepared for publication.

8.1 Introduction

As thermal excitations represent an ubiquitous energy scale in solid state systems, advancing to lower temperatures might open up the discovery of precedently unknown physical phenomena like fragile fractional quantum Hall states [7] and electron-mediated nuclear phase transitions both in 2D [79, 80] and 1D [4] systems. In many laboratories, the sample is only weakly coupled to the coldest spot of the refrigerator, resulting in sample temperatures up to one order of magnitude larger than the base temperature of the dilution refrigerator.

A promising approach to overcome this large temperature gradient is to use well-thermalized measurement leads with a special focus on efficient thermalization and extensive filtering [65]. Even lower temperatures can be reached by equipping a dilution refrigerator with an adiabatic nuclear demagnetization (AND) stage [41, 69]. Recent developments in pulse tube systems allow for AND experiments on cryogen-free platforms due to decreased vibration levels [189]. The implementation of an AND system on a pulse tube system has two major advantages compared to a conventional AND system: the experiment is independent of He liquefaction facilities and, because there are no He transfers needed, the precooling time as well as the experiment time (with the AND system in its "cold state") can be extended. Although still challenging, first operative systems have been implemented lately, using both $PrNi_5$ [201] and Cu [190] as a nuclear refrigerant.

In this article, we present a Cu-based AND stage on a cryogen-free system with 16 electronically separated nuclear refrigerators (NRs), aimed to cool nanostructured devices. Since cooling through the electron-phonon interaction is strongly suppressed at low millikelvin temperatures, this configuration allows us to cool samples through the conduction electrons [97].

Particularly in AND experiments, thermometry is crucial and can be very delicate due to the low temperature. The most prominent difficulty is the heat generated in sensors

due to their active (driven) nature, e.g. in susceptibility (paramagnetic salt) thermometers or resistors. Passive devices as for example noise thermometers [197] circumvent this problem, employing the fluctuation-dissipation theorem (Johnson-Nyquist noise) to link the measured noise to temperature. Whereas current-noise thermometers are acquiring the thermal noise current of a resistor [200, 201, 209], inductive noise thermometry can be completely contactless [202], as it has been shown for a magnetic field fluctuation thermometer [198, 208]. Thereby a superconducting coil picks up the magnetic flux noise generated by the thermal (Brownian) motion of electrons in a noise sample. A low-noise amplifier, e.g. a SQUID, is then used to enlarge the signal. In such a temperature sensor, parasitic heat generated by SQUID backaction and thermal conductance through the superconducting wires and shields can be significantly reduced [202, 203].

8.2 Nuclear Refrigerator Network on a Cryogen-Free Platform

Following the scheme of a parallel nuclear refrigerator network presented in Ref. [69], the design of the previously presented system was adapted to meet the demands of a cryogen-free setup [191] (see Fig. 8.1) and equipped with a magnetic field fluctuation thermometer. The measurement leads are filtered by lossy thermocoax [66] from room temperature to the mixing chamber (MC) flange of the dilution refrigerator. Additional filtering is achieved by home-built Ag-epoxy filters [65] and double-stage RC filters bolted to the MC flange. Each of the 16 leads is thermalized inside the Cu MC using two Ag powder sinters, electrically isolated from the environment. After exiting the MC as an annealed high-purity Ag wire (radius $r = 1.27\,\mathrm{mm}$, residual resistivity ratio (RRR) > 1200), every measurement lead passes through an Al heat switch with fused joints [61] and connects to a copper plate (the NR). At the bottom of each NR, another annealed Ag wire continues to the Ag epoxy chip socket, providing a platform for nanostructured samples on an easily exchangeable chip carrier, see Fig. 8.1.

Therefore each lead provides a thermally highly conductive but electronically isolated path from the sample to the MC or NR, respectively, depending on the state of the heat switches. Magnetic fields up to 9 T can be separately applied to both, the AND stage and the sample.

The Al heat switches and three thermometers are positioned in a region of cancelled magnetic field between the MC and the NR: a Cerium Magnesium Nitrate (CMN) thermometer and a LCMN (CMN diluted with Lanthanum) thermometer as well as a noise thermometer are connected to three separate NRs with massive Ag wires. All secondary thermometers are calibrated against a RuO_2 resistor on the MC flange which was calibrated using a fixed-point device. A finite stray field in the nominally cancelled region and the magnetic field of 15 mT needed to drive the Al switches normal-conducting necessitate the use of double-shielding by Nb and NbTi tubes for all temperature sensors.

AND experiments are very susceptible to heat leaks, because the cooling power is limited due to the finite number of polarized nuclear spins. Especially heat generated through eddy currents $\dot{Q}_{\mathrm{eddy}}$ can degrade the AND performance as there is a large amount of highly conducting material in large magnetic fields. We differentiate between the intrinsic heat leak $\dot{Q}_0$, which can arise from thermal radiation, rf heating through the leads or thermal conduction from higher temperature parts, and $\dot{Q}_{\mathrm{eddy}}$. Eddy current heating arises from both, nuclear demagnetization $\dot{Q}_{\mathrm{ramp}} \propto \dot{B}^2 = (dB/dt)^2$ and vibrations in a nonhomogeneous magnetic field $\dot{Q}_{\mathrm{vib}} \propto (dB/dt)^2 = [(dB/d\vec{r})(d\vec{r}/dt)]^2$.

Both the sensitivity to vibrations and the lower precooling temperatures needed to polarize a reasonable fraction of the Cu nuclei make AND on pulse tube system with a Cu stage more challenging than with a $PrNi_5$ stage. However, Cu enables lower final temperatures T_f by demagnetizing to smaller final fields B_f.

Although there are no mechanically moving parts in state-of-the-art pulse tubes, vibrations caused by high-pressure gas oscillations and the compressor package are transduced to the refrigerator. Despite significant progress in recent years, cryogen-free

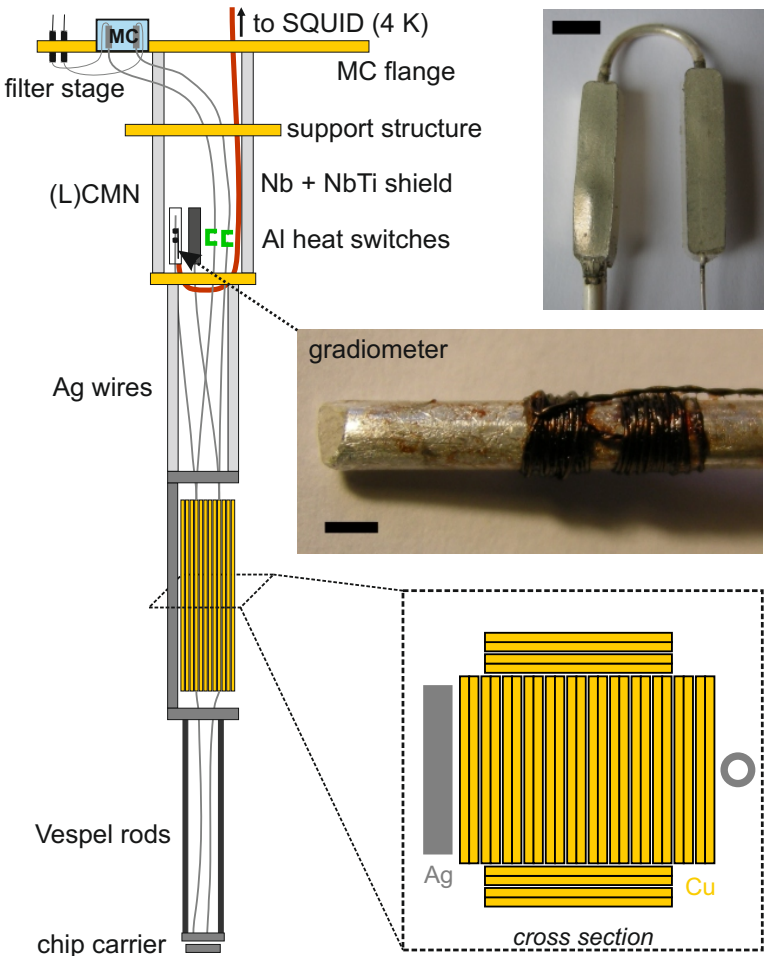

Figure 8.1: Schematic of the nuclear demagnetization stage. The measurement leads are thermalized with Ag powder sinters (*picture top right*, scale bar: 5 mm) in the mixing chamber (MC, blue) and pass through C-shaped Al heat switches (green) to the Cu plates. The gradiometer of the noise thermometer as well as the (L)CMN thermometers are positioned in a region of cancelled magnetic field between the MC and the NR stage. The gradiometer is double-shielded by a Nb and a NbTi tube (red). *Middle right inset:* Photograph of the gradiometer pick-up coil made from Nb wire with 100 µm diameter. The 2x 20 windings are wound in a gradiometer configuration on a high-purity silver wire which is spot-welded to a NR. Scale bar: 2 mm. *Lower inset:* Schematic cross section through the network of 16 parallel NRs.

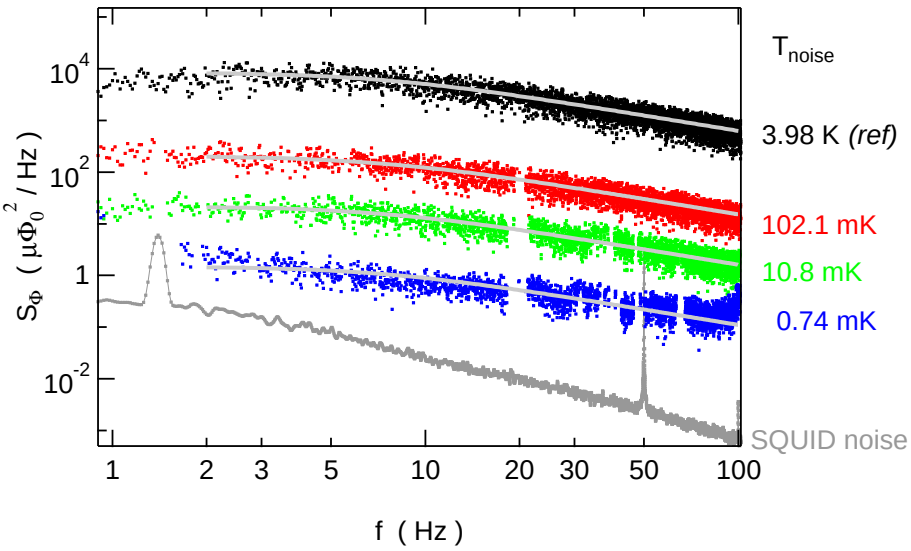

Figure 8.2: Power spectral density S_Φ of the Fourier-transformed thermal noise picked up by the gradiometer at different NR temperatures. The gray solid lines are fits using Eq. (8.1) which are converted to T_{noise} as described in the text using the reference spectrum at $T_{\mathrm{ref}} = 3.98\,\mathrm{K}$. At lower temperatures, the EMI effects get more pronounced as the excess noise becomes comparable with the signal amplitude of the thermal noise.

systems tend to have drastically increased vibration levels compared to standard systems (i.e. Dewars with cryoliquids). To account for these challenges, special care was taken on (i) damping all connections to the fridge and (ii) specific changes in the design of the nuclear stage. The latter include a rigid support structure and spacers between MC-shield / still-shield / magnet bore as well as an adapted geometry of the NRs: compared to the wet system version [97], we decreased the area critical for eddy current heating $\dot{Q}_{\mathrm{eddy}}$ and simultaneously increased the amount of Cu per plate by spot-welding two half-plates at the corners (see Fig. 8.1 middle inset). Each of the 16 Cu plates consists of $\sim 2\,\mathrm{mol}$ of Cu (2x[34 x 1.7 x 120] mm^3). Further, the area of the Ag-sinters in the MC as well as the radius of the Ag wires is doubled, since these thermal resistances have been identified as possible bottle necks regarding precooling temperature and time.

We note that cooling typical solid state samples through the leads is often compromised by the need of extensive shielding and filtering, which is crucial to minimize the heat leak through rf radiation. For this scenario, the importance of small heat leaks and high

thermal conductances becomes obvious by looking at a simplified example: assuming a heat leak of $\dot{Q} = 100\,\mathrm{pW}$, an electron temperature in the NR of $T_{Cu} = 1\,\mathrm{mK}$ and a thermal link via an electrical resistance of $10\,\mathrm{m\Omega}$, the temperature of the sample is $T_s = 9\,\mathrm{mK}$. This upper-bound estimate relies purely on Wiedemann-Franz cooling through conduction electrons, neglecting electron-phonon coupling since this contribution is very small.

8.3 Noise Thermometry

Here, a magnetic field fluctuation thermometer is employed in its secondary mode by using the spectral noise amplitude at a given temperature T_{ref} as a reference. The spectrum of a noise thermometer consists typically of a constant noise region $S_0(T)$ in the low frequency range (see Fig. 8.2) which can be attributed to the constant resistivity of high-purity metals below a few kelvin [60]. This plateau ends at a cut-off frequency f_c due to the Skin effect. For a rod-shaped sample, $f_c = 4.5\rho/(\pi\mu_0 r^2)$ with low temperature resistivity $\rho = \rho_{\mathrm{RT}}/\mathrm{RRR}$ and vacuum permeability μ_0 [203]. Thus, f_c can be engineered by choosing a noise sample with appropriate ρ and r [207]. Depending on the application, the sensor should be chosen such that the noise amplitude is large (small ρ) and a broad plateau to decrease the data acquisition time (large ρ) [203]. In consideration of the long timescales involved in AND, our main focus is a large signal amplitude and therewith a low ρ, which additionally facilitates thermal coupling to the NR. The attenuation behavior of the power spectral noise density for $f > f_c$ depends on the exact sensor geometry and the inductances involved.

To avoid effects from homogeneous magnetic fields, the pick-up coil is wound in a gradiometer geometry with 2x 20 windings on a high-purity Ag wire with $r = 1.27\,\mathrm{mm}$, which is spot-welded to the NR. The gradiometer shown in Fig. 8.1 is connected by a 70 cm long section of twisted Nb wires to the SQUID, which is anchored to the quasi-4 K-flange of the refrigerator. The twisted Nb wires are double-shielded with a Nb and NbTi tube.

By mounting the SQUID at 4 K we avoid low-frequency excess flux noise [210] which can arise at sub-K temperatures. The DC-SQUID is operated in flux-locked loop mode with XXF-1 electronics [204], including a second order Bessel-type low-pass filter ($f_{3\mathrm{dB}} = 10\,\mathrm{kHz}$). After a RT voltage preamplifier with another low-pass filter ($f_{3\mathrm{dB}} = 1\,\mathrm{kHz}$), the signal is acquired with a digital analog converter and Fourier-transformed.

Some exemplary noise spectra at different NR electron temperatures T_{Cu} are shown in Fig. 8.2. According to Nyquist's theorem, the power spectral noise density S_Φ is directly proportional to temperature. Every measurement consists of 10 real-time noise traces with 50 s duration each, which are averaged after Fourier transformation. At low T, the peaks arising from electromagnetic interference (EMI) become more visible due to the smaller noise signal amplitudes. To eliminate experimental excess noise from EMI, we fit every spectrum first with a polynomial of 10^{th} order and eliminate all peaks extending more than 1.3 times the standard deviation over the polynomial fit from the spectrum. In a second step, we use a simple low-pass like formula to fit our data:

$$S_\Phi(f, T_{\mathrm{noise}}) = \frac{S_0(T_{\mathrm{noise}})}{\sqrt{1 + \left(\frac{f}{f_c}\right)^2}}\,. \tag{8.1}$$

Although a detailed discussion of this experimental scheme can be found in Ref. [206], this simple analysis is sufficient for our application. After fitting Eq. (8.1) to our reference spectrum and thereby extracting the parameters f_c and $S_0(T_{\mathrm{noise}})$ with $T_{\mathrm{noise}} = T_{\mathrm{ref}} = 3.98\,\mathrm{K}$, we use $S_0(T_{\mathrm{noise}})$ as the only fit parameter and convert the low-frequency noise amplitude into temperature using $T_{\mathrm{noise}} = T_{\mathrm{ref}}\, S_0(T_{\mathrm{noise}})/S_0(T_{\mathrm{ref}})$. The cut-off frequency of $f_c = 7.5\,\mathrm{Hz}$ extracted from our reference noise spectrum corresponds to a realistic RRR ~ 1800 of the annealed silver wire.

In Fig. 8.3, we plot the temperature of the noise thermometer T_{noise} versus the NR temperature T_{Cu}, where the red markers are measured by heating the dilution refrigerator (with heat switches normal-conducting) and blue markers are measured from

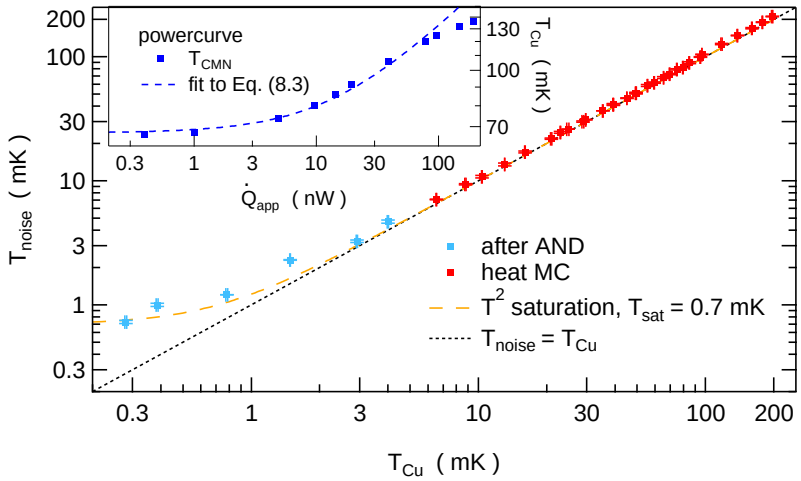

Figure 8.3: Temperature measured by the noise thermometer T_{noise} versus temperature of the nuclear stage T_{Cu}. T_{Cu} is measured with a calibrated RuO_2 resistor in the MC (red markers), while for temperatures below 7 mK (light blue markers), it is extracted from warm-ups after AND (see text and Fig. 8.4(a)). The black dotted line represents $T_{\mathrm{noise}} = T_{Cu}$. A deviation from the dotted line becomes apparent at $T_{\mathrm{noise}} \approx 5\,\mathrm{mK}$. The green dashed line represents the saturation behavior following a T^2 law, see Eq. (8.2). *Inset:* Power curve with Al switches open. The heat $\dot{Q}_{\mathrm{app}}$ is applied to a NR plate and its temperature is measured with the CMN thermometer (blue dots). The dashed line is a fit to Eq. (8.3) which allows us to extract $\dot{Q}_0 = 7\,\mathrm{nW/mol}$.

AND runs to different final fields B_f (see next section). Using the reference noise level $S_0(T_{\mathrm{ref}} = 3.98\,\mathrm{K})$, good agreement is found with T_{Cu} between [5..200] mK. Below $\sim 5\,\mathrm{mK}$, T_{noise} starts to deviate and saturates at 740 µK for our lowest T_{Cu} of 280 µK. The saturation follows a quadratic dependence like

$$T_{\mathrm{noise}} = \sqrt{T_{Cu}^2 + T_{\mathrm{sat}}^2} \tag{8.2}$$

with T_{sat} chosen empirically as 0.7 mK, indicated by the green dotted line in Fig. 8.3. This saturation is caused by either experimental excess noise or a heat leak impinging on the MFFT sensor.

8.4 Nuclear Refrigerator Performance

First, we use a power curve [41, 69] to measure the parasitic heat leak to the NR and therewith characterize the Al heat switches. The inset of Fig. 8.3 shows the NR temperature T_{Cu} (blue dots) measured with the CMN thermometer as a function of applied power $\dot{Q}_{\mathrm{app}}$ at $B = 0$ with the Al heat switches in their open state. In an equilibrium situation, $\dot{Q}_{\mathrm{app}}$ is drained by the MC, where the superconducting Al switches act as the primary thermal impedance. At low temperatures, the thermal conductance is dominated by phonon-dislocation scattering processes [45, 211], which obey the relation

$$\dot{Q}_{\mathrm{app}} = nA\left(T_{Cu}^3 - T_{\mathrm{MC}}^3\right) - \dot{Q}_0\,, \tag{8.3}$$

where $n = 1.95\,\mathrm{mol}$ is the amount of Cu per plate, A is a prefactor and $\dot{Q}_0$ is the intrinsic heat leak to the NR at $B = 0$. Fitting our data with Eq. (8.3), we extract $\dot{Q}_0 = 7\,\mathrm{nW/mol}$ for the NR plate with the CMN, which is in good agreement with the heat leaks measured at finite B, see Fig. 8.4 below. For $T_e > 120\,\mathrm{mK}$, parallel channels of heat flow become accessible, leading to a deviation from theory.

Next, we look at a typical demagnetization run which is started by ramping the field to $B_i = 9\,\mathrm{T}$ and precooling the NRs through the Al heat switches in their closed (normal-conducting) state. The NR's electron temperature T_{Cu} decreases from 40 mK to $T_i \simeq 11\,\mathrm{mK}$ within 40 h. Then, the heat switches are opened and B is ramped to 1 T with 1 T/h and subsequently to $B_f = 0.2\,\mathrm{T}$ with 0.5 T/h. We observe a saturation for all our temperature sensors towards the end of the AND process. A possible reason for the CMN saturation could be magnetic ordering (Curie-Weiss, expected $T_c \simeq 2\,\mathrm{mK}$ [45]), while the saturation of the noise thermometer could be caused by external noise sources or due to a heat leak. Therefore, T_{Cu} is extracted using the warm-up method [45, 69] (blue markers in Fig. 8.3): under a certain molar heat load $\dot{Q}$, the inverse electron temperature T_e^{-1} decreases linearly in time t:

$$T_e^{-1}(t) = T_{\mathrm{ex}}^{-1} - t\left(\frac{\lambda_n B_f^2}{\mu_0 \dot{Q}} + K\right)^{-1}, \tag{8.4}$$

where λ_n and K are the molar nuclear Curie constant and the Korringa constant for Cu [41], respectively. The electron temperature at the end of AND T_{ex} is extrapolated by fitting a line in a temperature range of [6..20] mK, where $T_e^{-1}(t)$ shows the expected linear behavior, see Fig. 8.4(a). Here we assume that the copper plate warms up "completely", i.e. $1/T_e(t \to \infty) \to 0$. The linear fit will then reveal $\dot{Q}$ as well as the final temperature after demagnetization $T_f = T_{ex}$.

The determination of T_f at the end of the demagnetization run allows us to define an efficiency of the AND process: $\xi = (T_i/T_f)/(B_i/B_f)$. Heat leaks of different nature decrease the efficiency during the demagnetization run, making the process nonadiabatic. Due to a reasonably low heat leak for a pulse tube system, we are able to cool electrons in the NR to $T_f = 280\,\mu\mathrm{K}$ for $B_f = 0.2\,\mathrm{T}$, similar to a comparable system in the previously described setup [97]. Typical values for a cooling cycle as described above are $\dot{Q} \approx 4\,\mathrm{nW/mol}$ and $\xi \approx 70\,\%$. These numbers may vary between different NRs.

Since the AND process is very time-consuming, we present a faster method to extract the heat leak $\dot{Q}$ in Fig. 8.4(b): by precooling at a fixed B, the inverse electron temperature can be measured as a function of time after opening the heat switches. The heat leaks we extract with this method at $B = 0.75\,\mathrm{T}$ are roughly consistent with the ones from the warm-up method.

When repeating this procedure for different B, one would expect a quadratic dependence of $\dot{Q}(B)$ assuming that vibrations cause eddy current heating via relative displacement between NR and magnet, assuming $\dot{B} \propto B$ and thus $\dot{Q}_{\mathrm{vib}} \propto B^2(d\vec{r}/dt)^2$. Contrary to these expectations, such behavior is not observed, as shown in the inset of Fig. 8.4(b). Therefore it is likely that vibrations are not the source of these heat leaks at $B \leq 1\,\mathrm{T}$. The rather large loss in efficiency during the demagnetization process is caused

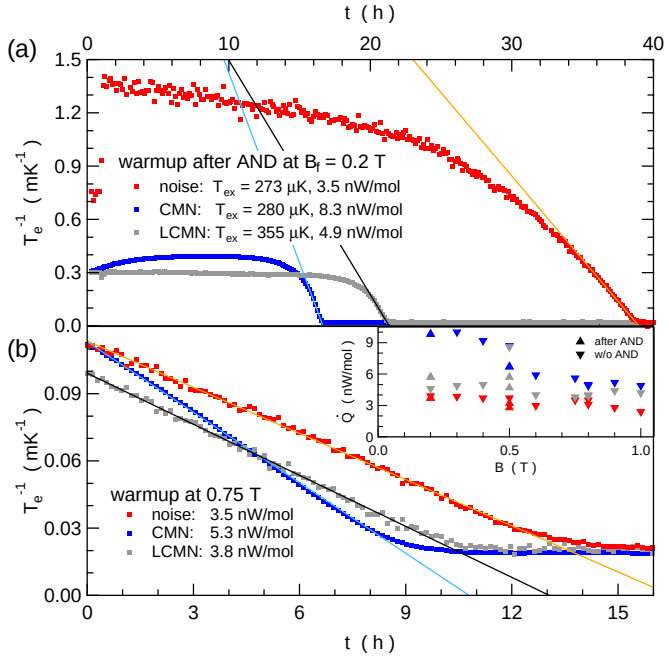

Figure 8.4: Two methods to extract the heat leak $\dot{Q}$ to the nuclear stage per mol of Cu using Eq. (8.4): (a) Inverse electron temperature T_e^{-1} of three thermometers versus time after demagnetizing to $B_f = 0.2\,\mathrm{T}$. Due to the saturation of all sensors, we fit in the temperature range of $[6..50]\,\mathrm{mK}$, where the sensors read correctly. The linear fits (solid lines) reveal extrapolated electron temperatures T_{ex} (and heat leaks) of $273\,/\,280\,/\,355\,\mu\mathrm{K}$ ($\dot{Q} = 3.5\,/\,8.3\,/\,4.9\,\mathrm{nW/mol}$) for the noise thermometer / CMN / LCMN, respectively. (b) T_e^{-1} of the same thermometers versus time after opening the heat switches at $B = 0.75\,\mathrm{T}$, resulting in $\dot{Q} = 3.5\,/\,5.3\,/\,3.8\,\mathrm{nW/mol}$ for the noise thermometer / CMN / LCMN, respectively. *Inset:* $\dot{Q}$ at different B, measured with the methods described in panel (a) (depicted by ▲) and (b) (▼), respectively.

by a substantial heat leak $\langle \dot{Q} \rangle$ of unknown origin. This finding can be reproduced with simulations where we have to assume $\langle \dot{Q} \rangle \approx [30..60]\,\mathrm{nW/mol}$ to match T_f. The heat leak $\dot{Q}_{\mathrm{eddy}}$ calculated from the geometry of one NR plate for $\dot{B} = 1\,\mathrm{T/h}$ is a factor of [10..20] smaller, and measurements at static B reveal $\dot{Q} = (\dot{Q}_{\mathrm{vib}} + \dot{Q}_0) < 10\,\mathrm{nW}$, as shown above. However, we can not exclude vibrations caused by relative displacement between the magnet and the NRs as an additional heat source at large B.

8.5 Conclusions

In summary, we have implemented a parallel network of 16 electronically separated NRs on a cryogen-free platform. These 16 plates are part of the measurement leads and can be used to cool nanostructured samples below the base temperature of the dilution refrigerator. The nuclear stage is equipped with a magnetic field fluctuation thermometer, showing good agreement with the NR temperatures T_{Cu} down to 5 mK. After AND to $B_f = 0.2\,\mathrm{T}$, the lowest temperature reading is limited to 0.74 mK, although the NR temperature extracted with the warm-up method indicates electron temperatures as low as $T_f = 280\,\mu\mathrm{K}$. The reason of the saturation might be either a residual heat leak at the MFFT sensor or experimental excess noise. The heat leaks measured on the NRs are in the order of 4 nW/mol and allow the AND stage to stay below 1 mK for one day. Higher B_f allow for even longer hold times, still supplying reasonably low bath temperatures for many nanoelectronic experiments.

Acknowledgement

We would like to thank H. J. Barthelmess, R. Blaauwgeers, M. Steinacher and P. Vorselman for useful input and discussions. The work shop team of S. Martin is acknowledged for technical support. This work was supported by EU-FP7 MICROKELVIN network.

9 Conclusion & Outlook

In the course of this thesis, a parallel network of nuclear refrigerators was implemented first in a wet and then in a dry system, intended to cool nanostructured samples to millikelvin temperatures and below. The new concept targets to use the conduction electrons, which couple strongly to the nuclei in the NRs, to cool the devices and thereby circumvents the problem of the weak coupling of a solid to liquid helium due to the increasing Kapitza resistance.

9.1 Wet Adiabatic Nuclear Demagnetization Setup

Chapters 3 to 6 describe experiments on an AND stage with 21 NRs, bolted to a dilution refrigerator in a Dewar with cryoliquids. The heat leak to the NR was measured as $\dot{Q}_0 \leq 1\,\mathrm{nW/mol}$, which allows the AND stage to stay below 1 mK for 50 h and below 2 mK for roughly 1 week [47]. Using this setup, we demonstrated a deviation from electron-phonon cooling at low millikelvin temperatures using metallic Coulomb blockade thermometers (CBTs). This alteration is a first evidence that our attempt to cool the devices using the electronic degree of freedom was feasible. In a next step, we investigated surface-gated quantum dots in a GaAs/AlGaAs 2DEG operated in deep Coulomb blockade. By measuring the width of the Fermi-Dirac distribution of the electron reservoirs, these devices can be employed as electron thermometers. Due the requirement of an energetically sharp dot level compared to the thermal broadening of the leads, we examined both, quantum dots in direct transport and with adjacent charge sensing dots. This thermometer works between [20..120] mK and saturates at roughly 10 mK. Close to the saturation T, it is very sensitive to changes of the electronic environment, i.e. charge switches. We speculate that intrinsic charge fluctuations in the wafer might pose a limit for the lowest temperatures measured. However, other possibilities like a finite heat leak in combination with the moderate thermal coupling through the ohmic contacts, even if they are of low resistance, can not be excluded.

After replacing the Macor chip socket and carrier (described in Ref. [48]) with a version made from Ag epoxy, where every lead is additionally filtered, we planned to investigate fragile fractional quantum Hall states in a high-mobility wafer, e.g. the elusive $\nu = 5/2$ state and other states with low energy gaps. In the course of these measurements, we found quantized longitudinal conductance R_{xx} in the integer quantum Hall effect which can be attributed to a large density gradient across the 2DEG. This gradient also affects the gap of fractional quantum Hall states, thus questioning the use of R_{xx} (ρ_{xx}) as the predominant probe of quantum Hall physics.

In a further thermometry experiment, we measured electron temperatures of $\sim 7\,\mathrm{mK}$ using a device with a normal metal / insulator / superconductor (NIS) tunnel junction. The extreme sensitivity to magnetic fields in the order of a few Gauss is currently not understood. We suspect that the saturation at 7 mK is caused by a heat leak, potentially from the chip carrier, because the thermal model suggests that the overheating in the superconductor does not affect the temperature reading.

The common denominator of CBTs, quantum dots, NIS devices and other on-chip electron thermometers is the fact that they measure the temperature by probing the thermal smearing of the Fermi-Dirac distribution in an electron reservoir. During our measurements, we became aware of the extreme sensitivity of those thermometers to experimental noise. We suppose that this kind of noise does not heat up our devices directly by heat dissipation, but the voltage noise can broaden the Fermi-Dirac distribution through fluctuations in the reservoir's chemical potential. Thus, for a measurement acquisition rate slower than these fluctuations, the Fermi-Dirac distribution will appear broadened and reveal increased temperatures. From the convolution of a Lorentzian line shape (as it is used for primary thermometry with a CBT device) with a Gaussian voltage noise distribution, Ref. [47] infers that these broadening effects can become crucial for $T < 10\,\mathrm{mK}$, assuming a realistic voltage noise of $V_{\mathrm{rms}} = 1\,\mu\mathrm{V}$ (see Fig. 5.10 in [47]). Besides finite amounts of heat release and heat leaks from other sources, this eventually poses a further serious obstacle in reaching sub-millikelvin temperatures.

9.2 Cryogen-Free Adiabatic Nuclear Demagnetization Setup

Similar progress was made on a "dry" system operated with a two-stage pulse tube, where we successfully implemented an AND stage consisting of 16 nuclear refrigerators (NRs), reaching temperatures as low as 280 µK. The residual heat leak on the NR was measured as 4 nW/mol, allowing hold times below 1 mK of about 1 day. However, a substantial heat leak on the sample stage prevents us to reach sample electron temperatures below $T_e \approx 15$ mK. The reason for this is potentially heat release from the epoxy used in the chip socket and chip carrier combined with the thermal coupling to the NR that has been weakened compared to the wet system for the benefit of stronger filtering.

The MFFT shows good agreement with other thermometers in a range of [5..200] mK, while it is calibrated at a reference temperature of roughly 4 K. At present, we observe a saturation at 0.7 mK which might arise from residual thermal conductance through the superconducting shields or from experimental excess noise. Bringing the SQUID closer to the gradiometer coil would decrease the thermal gradient along the superconducting shield and thus reduce the heat leak. At the same time, though, this could lead to excess low-frequency flux noise scaling with $1/f^{\alpha}$ where $0.58 < \alpha < 0.80$ [210]. How this additional flux noise will affect the thermal noise at the lowest temperatures has not been tested yet in our MFFT setup.

In general, the problem of heat release from the chip socket and carrier has to be addressed. As a first step, a new sample stage including socket and chip carrier is currently implemented in the dry system. It is made from sapphire (crystalline Al_2O_3) and lacks the additional filtering stage to reinforce the thermal coupling to the NRs. Another possible bottleneck regarding thermal conductance are the press contacts of the Au-plated pins. The problem is that wire-bonding on a sample holder mounted permanently on the refrigerator is not feasible. Therefore the press contacts are indispensable.

To further reduce the noise level generated by the pulse tube compressor and remote motor, one could install a rigid clamp right next to the cold head of the pulse tube. The remote motor, which sits on a rigid platform in the current setup, should then be allowed to vibrate, e.g. by placing it loosely on a foam. In this situation, the breathing of the tube that connects the remote motor with the cold head would potentially transduce vibrations mostly to the motor and not to the table.

9.3 General Prospects

Currently, we investigate the low temperature behavior of reentrant integer quantum Hall states [28] in the wet system, which reveal long time constants (in the order of several days) to equilibrate the sample to T_{base} after cooldown [67]. This indicates a significant amount of heat release, potentially arising from the epoxy of the chip socket and carrier. Once we have wafers with improved quality at hand and better control of the influence of the fabrication process on the 2DEG mobility, the low temperatures will be beneficial for different experiments like $\nu = 5/2$ statistics using interferometers [128–130] or antidots [212–214]. Recently proposed theories of the quantum Hall effect using a "strip of stripes" model [215] or helical nuclear spin order [216] could also be explored experimentally. Furthermore, an experimental evidence for the electron-mediated nuclear ferromagnetic phase transition in two dimensions [79, 80] is still lacking. Another unresolved question is if the electron phase coherence time saturates at the lowest temperatures [101] or not [217]. Using devices with open quantum dots in our setup, we could extend the investigated temperature range.

For the measurements on NIS devices, future experiments could include the use of a second ground plane on top in combination with the backplane as well as an intensified filtering stage to further reduce the Dynes parameter γ. In addition, the normal-metal side of the samples should be bonded by multiple Au wires to enhance the thermal contact to the cold bath.

Another interesting approach would be to measure the quantum dots again with the

new chip socket and chip carrier, be it in the wet or the dry system. This could potentially lead to lower temperatures, pushing the frontier slowly but steadily close to the sub-millikelvin regime. Such low electron temperatures in a 2DEG structure might then facilitate to investigate different kind of effects, e.g. comparing noise from different sources as it has been recently done in optically active quantum dots [113]. Furthermore, the study of backaction effects of a charge sensor to the quantum dot [218, 219] will also benefit from low reservoir temperatures. A better understanding of this phenomenon would be relevant for the design and operation of spin and charge qubits [111]. Last but not least, the investigation of correlated many body states like the Kondo effect and higher order manifestions [35, 220] would profit from electron temperatures in the low millikelvin regime.

A Method for Cooling Nanostructures to Microkelvin Temperatures

A. C. Clark*, K. K. Schwarzwälder*, T. Bandi, D. Maradan, D. M. Zumbühl

Department of Physics, University of Basel, CH-4056 Basel, Switzerland

Abstract

We propose a new scheme aimed at cooling nanostructures to microkelvin temperatures, based on the well established technique of adiabatic nuclear demagnetization: we attach each device measurement lead to an individual nuclear refrigerator, allowing efficient thermal contact to a microkelvin bath. On a prototype consisting of a parallel network of nuclear refrigerators, temperatures of $\sim 1\,\mathrm{mK}$ simultaneously on ten measurement leads have been reached upon demagnetization, thus completing the first steps toward ultracold nanostructures.

* These authors contributed equally to this work.

This chapter was published in *Rev. Sci. Instrum.* **81**, 103904 (2010).

Introduction

The ability to reach low millikelvin or even microkelvin temperatures in nanoscale samples would open up the possibility to discover new physics in a variety of systems. For example, an intriguing nuclear spin ferromagnetic phase transition in a GaAs interacting 2D electron gas (2DEG) has been predicted [79, 80] to occur around $\sim 1\,\mathrm{mK}$ at $B = 0$, constituting a novel type of correlated state. Nuclear spin fluctuations would be fully suppressed in this ferromagnetic phase, eliminating the main source of decoherence for GaAs spin qubits [3]. Further, full thermodynamic nuclear polarization is possible [221] at temperatures $T \lesssim 1\,\mathrm{mK}$ in an external magnetic field of $B \sim 10\,\mathrm{T}$. Other systems benefiting from ultralow temperatures include fractional quantum Hall states with small gaps [7, 29], in particular the $\nu = 5/2$ state [95], which is currently considered for topological quantum computation [81, 124].

The majority of quantum transport experiments to date, such as those in GaAs 2DEGs or any other nanoelectronic devices on insulating substrates, have been carried out at electron temperatures T_e significantly greater than that of the host ^{3}He/^{4}He dilution refrigerator (DR). Since only metals provide significant thermal conduction at temperatures well below 1 K [45, 55], nanostructures are thermally connected to and cooled by the DR primarily through their electrical leads. Since these leads need to be electrically isolated, some insulator will still inhibit efficient cooling. The main challenges for cooling such samples below 1 mK include overcoming poor thermal coupling between electrons in the leads and the refrigerator [35, 96], providing sufficient attenuation of high frequency radiation, and reducing low frequency interference such as ground loops. To our knowledge, the minimum temperature reported is 4 mK, with sintered silver heat exchangers attached to sample wires in a ^{3}He cell [7, 29]. Similarly, Pomeranchuck cooling [45] with sinters on each sample wire could reach temperatures $\sim 1\,\mathrm{mK}$.

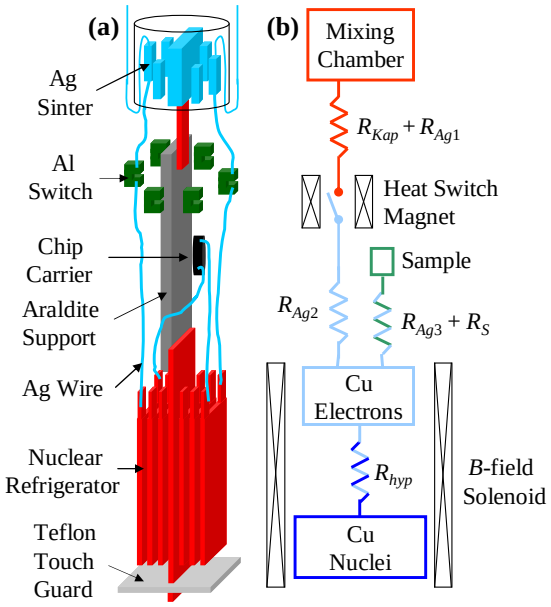

Figure A.1: (a) Schematic of parallel nuclear refrigerator network (not to scale). Only six NRs are shown for simplicity. The Cu pieces are $(20 \times 2 \times 100)\,\mathrm{mm}^3$ and positioned approximately 350 mm below the bottom of the MC. (b) Cooling scheme, with different colors denoting potentially different temperatures under steady state conditions.

Here we present a new method intended to cool nanostructures into the microkelvin regime. We propose to adapt the very well established technique of nuclear adiabatic demagnetization to the specific needs of nanoscale samples: every sample wire passes through its own, separate nuclear refrigerator (NR) (see Fig. A.1), ensuring excellent thermal contact even at microkelvin temperatures between the sample and the NR while keeping all wires electrically isolated from one another, as required for measurements. With this method, nanostructures can in principle be cooled to less than 100 µK, which would be a reduction in temperature by more than two orders of magnitude compared with common $T_e \gtrsim 10\,\mathrm{mK}$. Further, we have designed, built, and tested a prototype refrigerator that is based on this proposal. We present evidence for achieving $\sim 1\,\mathrm{mK}$ in ten NRs simultaneously, thus completing the first steps towards microkelvin nanostructures.

Nuclear adiabatic demagnetization is the most widely used technique available today for ultralow temperature experiments in condensed matter [41, 45, 55]. The lowest temperatures reported are $\sim 1\,\mu\mathrm{K}$ for electrons in platinum [39] and $\sim 300\,\mathrm{pK}$ for

nuclear spins in rhodium [40, 222] – among the lowest temperatures achieved in any laboratory. It is a single shot method consisting of three steps. First, a suitable metal with nonzero nuclear spin (the NR) is precooled with a DR in a large magnetic field B_i to a temperature $T_i \sim 10\,\mathrm{mK}$, generating as large a thermodynamic nuclear spin polarization as possible. Second, thermal contact between the DR and NR is cut off by a superconducting heat switch and the B-field is adiabatically reduced by a large factor, e.g. $x = B_i/B_f \sim 100$. Ideally (with perfect adiabaticity), the nuclei are cooled by the same factor such that $T_f = T_i/x$. Finally, experiments are performed at microkelvin temperatures for a finite time, typically days or even weeks. The heat leaking into the system plays an important role since it increases T_e in the NRs above the nuclear spin temperature and is absorbed by the nuclei until the polarization is lost and the NRs heat up to or above DR temperatures.

We propose to cool nanostructures to microkelvin temperatures using a parallel network of NRs. Each NR constitutes part of the electrical connection from room temperature down to the sample. Semiconductors and insulators, commonly used in nanosamples, are not practical as NRs since it is difficult to sufficiently precool their nuclei. Still, one might consider as NRs devices with large conducting regions containing nuclear spins, such as GaAs 2DEGs with a highly doped, metallic back gate (or similar). However, their nuclear heat capacity would be drained all too quickly given realistic heat leaks and 2DEG sizes. Therefore, our strategy is to incorporate the most widely used material for NRs: Cu, an excellent conductor with nuclear spin 3/2. In this system the nuclear hyperfine interaction couples the nuclei at temperature T_f to the electrons at temperature T_e with a characteristic nuclear spin relaxation time τ_1 that obeys the Korringa law [45, 55], $K = T_e\tau_1 \approx 1\,\mathrm{K\,s}$. The effective thermal equilibration time is reduced from τ_1 by the very large ratio of nuclear and electronic heat capacities [64], resulting in strong, fast coupling even at $T_e < 100\,\mu\mathrm{K}$. However, conducting sample sections may be thermally isolated from other degrees of freedom at low enough temperatures.

Nuclear refrigerator network

We now turn to the discussion of the prototype NR network (see Fig. A.1). Each NR consists of a Cu plate situated in the center of a demagnetizing field, connected with high conductivity wires on one side to a home built chip carrier made from 2850 FT Stycast epoxy, and on the other side through a heat switch [61] to the mixing chamber (MC) of a DR. Twelve parallel NRs are tied to a sacrificial NR with dental floss, using small teflon spacers ensuring electrical (and thermal) isolation, giving a total of 13 NRs. The sacrificial Cu piece is glued into an araldite beam extending from the MC. A teflon touch guard is positioned at the bottom of the sacrificial piece to prevent the NRs from contacting the 50 mK shield of the DR. The shield serves two purposes: to reduce black-body radiation from higher temperature stages of the cryostat and to protect from stray radio-frequency (rf) noise sources.

To ensure proper operation of the NRs, we note some important details. Each measurement wire begins with 1.6 m of lossy thermocoax [66] extending from room temperature down to the MC cold finger. It then passes through a silver epoxy microwave filter [65] and is transferred to a bare Ag wire that is fed directly into the plastic MC. These two filtering steps are important for minimizing the rf noise dropping across the device. For efficient thermalization of the Cu during precooling the thermal resistance between the NR and MC must be minimized. We therefore use annealed, high purity Ag wire with 1.27 mm diameter and residual resistivity ratio ≥ 1500, which are spot welded to the Cu pieces and, in the MC, sintered to Ag nanoparticles (yielding surface areas of $\sim 3\,\mathrm{m}^2$ per wire used to overcome the Kapitza resistance R_{Kap}). The heat switches are "C"-shaped pieces of annealed, high purity Al fused to the Ag wires on both ends. The small critical field of 10 mT allows easy switching with a home built magnet. The ratio of thermal conductivities in the closed state (Al normal) to the open state (Al superconducting) exceeds 10^4 below 20 mK. Al pieces are placed carefully to minimize differences in the stray B-field from the solenoid, adding additional complexity for a network of NRs.

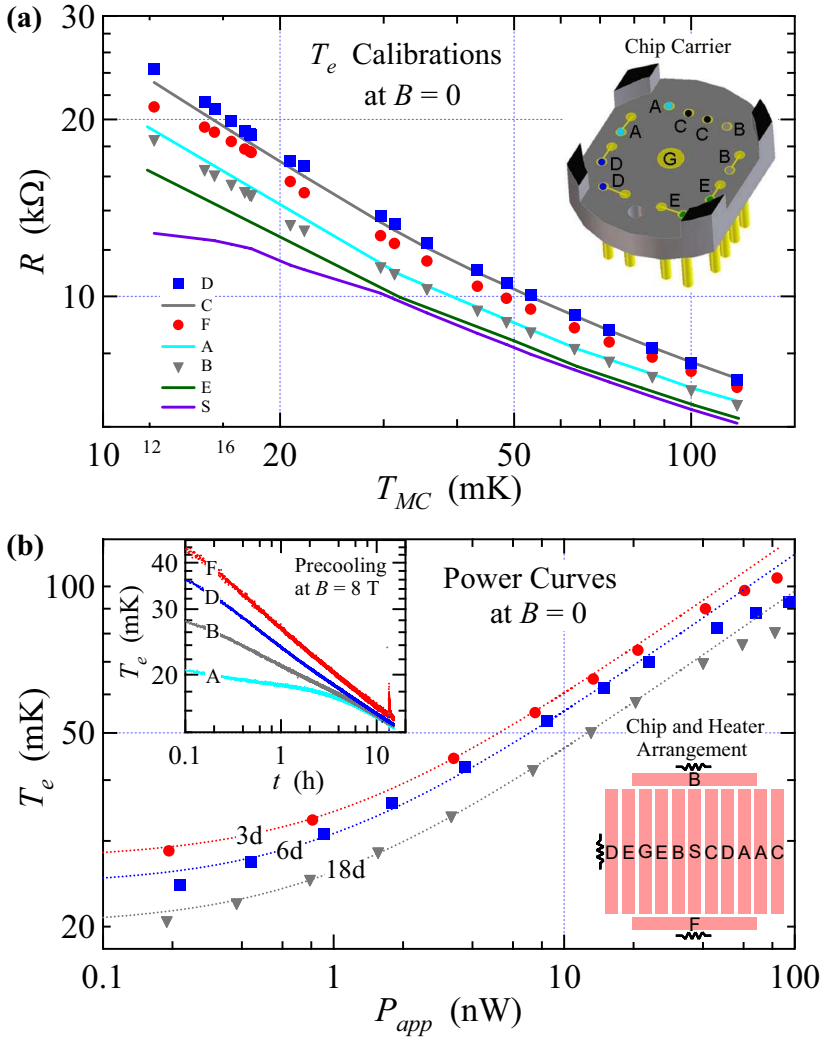

Figure A.2: (a) Resistance of RuO_2 chips as a function of T_{MC}. *Inset:* Chip carrier. It is 20 mm across from one flat to the other. The bond pads are polished Ag wires, 1.27 mm in diameter. (b) Power curves with Al switches open measured 3, 6 and 18 days after cooling down, shown for chips F (circles), D (squares) and B (triangles), respectively. Dashed lines are theory (see text). *Left inset:* T_e versus time during precooling ($B = 8$ T). *Right inset:* Arrangement of Cu plates in the NR stack.

The entire stage is removable at a plastic cone seal at the MC, allowing samples to be directly wire bonded to polished Ag wires. Probably the weakest thermal/electrical link between the device and the NR occurs at the Schottky barriers of the metal-semiconductor contacts, integrated on chip. In steady state, parasitic heat leaking into the device will equal the heat leaving it through its thermal links to the NRs, setting the lowest achievable temperature. Metallic nanostructures will benefit from comparatively higher conductivity metal-metal contacts.

Thermometry and heat leaks

Characterization of the NRs has been carried out by monitoring T_e of the various Cu plates. Five RuO_2 chip resistors, labeled A-E, were mounted on the chip carrier (see Fig. A.2(a) inset) and electrically connected[5] to 10 of the 13 NRs, with each chip using a pair of NRs as its leads. The resistance reading in these cases reflects an average temperature of each pair. Two more chips, F and S, were directly mounted onto individual NRs (S on the sacrificial Cu plate), with the second contact of each electrically connected to – but thermally isolated from – the outside world by a bare NbTi superconducting wire. The final plate was left unmonitored, serving as electrical ground (G) for chip capacitors across A and B. It is well known that RuO_2 thermometers can suffer from rather long time constants[6] and saturate below 10 mK. However, in the demagnetized state we can extrapolate the NR temperatures below 10 mK based on warm-up curves, as will be described below.

We first calibrate the RuO_2 thermometers between 12 and 120 mK. Figure A.2(a) shows the resistance of the seven RuO_2 chips at $B = 0$ as a function of mixing chamber temperature T_{MC} with Al switches closed. T_{MC} was measured by a cerium magnesium nitrate (CMN) thermometer bolted to the MC cold finger. Before measuring each data point, an appropriate amount of time for thermalization was allowed. There is no apparent saturation down to $T_{MC} = 12$ mK for thermometers A-F, which all exhibit qualitatively the same temperature dependence. Moreover, on two separate cooldowns a second CMN was mounted directly onto one of the NRs[7] (first A, then F), verifying that T_e measured by the RuO_2 chips is indeed equal to T_{MC}. We therefore use the data in Fig. A.2(a) as electron temperature calibrations for NRs A-F. The sacrificial plate thermometer S displays some saturation for $T_{MC} \leq 30$ mK, presumably due to a heat

[5]The (superconducting) tin on the pads of the RuO_2 chips was removed. Contact was made using Ag epoxy.

[6]The total thermal equilibration times for the chips are 20 min at 30 mK, 120 min at 15 mK and > 4 h at 5 mK.

[7]The NR was able to cool the CMN to ≤ 3 mK. However, a heat leak of > 20 nW was detected from the thermometer, severely limiting the NR performance.

leak. Upon ramping the magnet to $B = 8\,\mathrm{T}$, the massive nuclear heat of magnetization significantly elevates the NR temperatures (varying somewhat for individual plates depending on stray B-field conditions at the corresponding heat switches), but they cool within 15 h to $T_i = T_e \leq 15\,\mathrm{mK}$ (see Fig. A.2(b), left inset).

Next, we measure the parasitic heat leak to the NRs. Figure A.2(b) shows the NR temperature T_e as a function of applied power at $B = 0$ and with the Al switches open. The heat flowing into the Cu is ultimately drained away by the MC, with the superconducting Al piece as the primary impedance. Its thermal conductance is dominated at low temperature by phonon-dislocation scattering processes, obeying the relation [45, 211] $P_{\mathrm{app}} = nA(T_e^3 - T_{\mathrm{MC}}^3) - P_0$, where P_{app} is the applied power, $n = 0.57\,\mathrm{mol}$ of Cu, A is a prefactor and P_0 is the intrinsic heat leak to the NR. For $T_e > 70\,\mathrm{mK}$, parallel channels of heat flow become accessible[8]. Fits (dashed curves) are in very good agreement with the data and allow us to extract P_0, which improved over time as indicated by the decrease in T_e (true for *all* chips A-F) as $P_{\mathrm{app}} \to 0$ in the power curves obtained 3, 6 and 18 days after cooling down (top to bottom curves). We conclude that the typical intrinsic heat leak to the NR stage at $B = 0$ is $P_0/n \lesssim 1\,\mathrm{nW\,mol^{-1}}$, sufficiently low but clearly above the state of the art value [64] of $< 5\,\mathrm{pW\,mol^{-1}}$. We note that the average heat leak measured at $B = 2\,\mathrm{T}$ is $\sim 7\,\mathrm{nW\,mol^{-1}}$, which is most likely from eddy currents in the Cu pieces generated by small vibrations in the nonuniform B-field.

Performance

Given a heat leak sufficiently low for nuclear cooling, we now evaluate the demagnetization process itself, starting from $T_i = 15\,\mathrm{mK}$ and $B_i = 8\,\mathrm{T}$. The inset of Fig. A.3 shows the resistance of several chips during a series of ramps from $8\,\mathrm{T} \to 1\,\mathrm{T}$ with open heat switches. The B-field is decreased linearly in time using three sequential ramps at $1\,\mathrm{T\,h^{-1}}$ from $8\,\mathrm{T} \to 4\,\mathrm{T}$ and at $0.5\,\mathrm{T\,h^{-1}}$ from $4\,\mathrm{T} \to 2\,\mathrm{T}$ and $2\,\mathrm{T} \to B_f = 1\,\mathrm{T}$.

[8] Heat conduction by free electrons becomes larger than phonons near 70 mK. Also, there will be some heat flow through the teflon spacers between NRs at high T_e.

R values increase upon demagnetization, clearly indicating cooling. They continue to increase (at fixed values of 4 and 2 T) between each B-field ramp and in fact do so more quickly, reflecting both a thermal lag between the chips and Cu plates as well as a sensitivity to ramp rate. If enough time is allowed after reaching 1 T, R increases further by 5 to 10 kΩ for chips A-E (not shown). Chip F warms up near the end of the demagnetization, while S is nearly constant. The apparently higher heat load on F seems to be associated with vibrations[9]. However, its performance improves for lower precooling temperatures. For S, the lack of cooling *and* warming suggest that thermal contact to the environment remains significant.

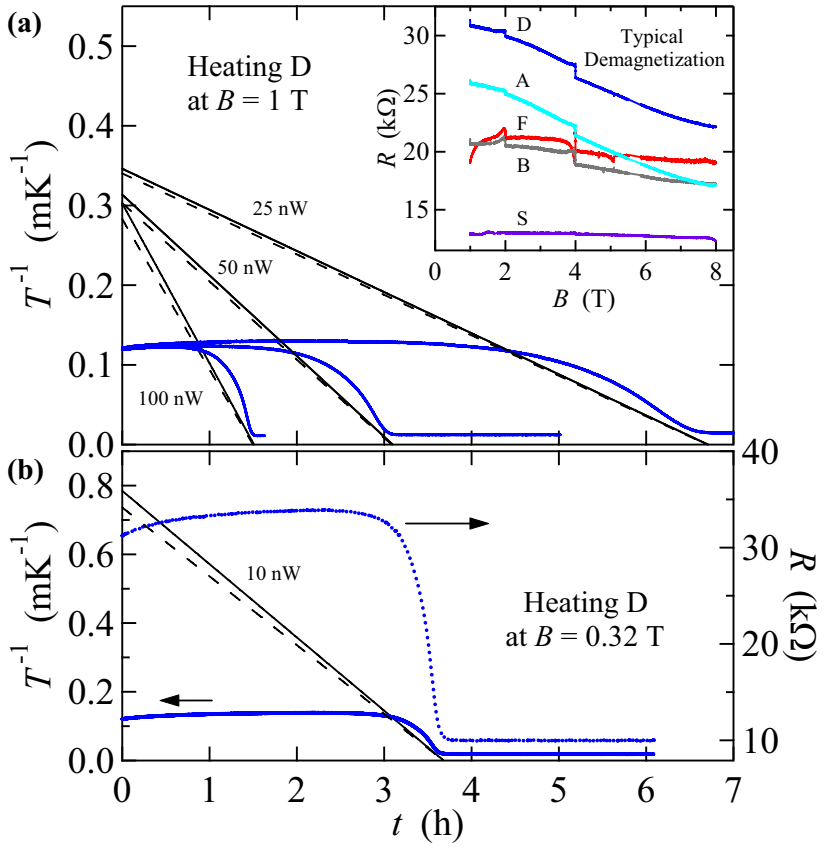

Figure A.3: (a) Systematic heating tests for chip D after demagnetization. Measured T_e^{-1} (blue curves) and theory for T_f^{-1} (solid lines) and T_e^{-1} (dashed lines) versus t for the applied powers indicated. *Inset:* Cooling of chips during demagnetization. R of thermometer D is plotted against the right axis for comparison in (b).

We extract T_f and T_e ($\gtrsim T_f$) of the NRs reached after demagnetizing to B_f by recording

[9]When the cryostat is tapped we observe larger warming spikes for F than the other chips (e.g. the dip in resistance near $B = 4$ T in Fig. A.3(a) inset).

the time t necessary for a Cu plate to "completely" ($T_e^{-1} \rightarrow 0$) warm up under an applied power, using $t = n\Lambda B_f^2/(P_{\rm app}T_f)$ and $T_e{=}T_f(1 + KP_{\rm app}/n\Lambda B_f^2)$, where Λ is the nuclear Curie constant for Cu [45, 64]. In Fig. A.3(a), we plot time traces of T_e^{-1} for chip D (not calibrated above $0.08\,{\rm mK}^{-1} = 12.5\,{\rm mK}$) for $P_{\rm app} = 25$, 50 and 100 nW. The other thermometers give consistent results, except for F, which appears to heat up during demagnetization. Due to poor internal thermalization T_e^{-1} increases for the first several hours despite the influx of heat, only showing significant signs of warming once the Cu is hotter than $\sim 10\,{\rm mK}$. Since the temperature gradient between the chip and NR will vanish at $T_f^{-1} = T_e^{-1} = 0$, we fix this point of the theoretical T^{-1} curves (solid and dashed lines) and extrapolate back to $t = 0$. As expected, larger $P_{\rm app}$ results in faster warm-up times. With this, we obtain $T_f(0) = 3.0 \pm 0.3\,{\rm mK}$ for all three $P_{\rm app}$, demonstrating the reliability of achieving a particular minimum temperature for a set of demagnetization parameters. The uncertainty in $T_f(0)$ is dominated by the inhomogeneity of B_f. We note that in the temperature range explored here, $T_e(0) \approx T_f(0)$ before the power is turned on since $P_0 \ll P_{\rm app}$.

The final test from the present work (see Fig. A.3(b)) is a demagnetization from 8 T $\rightarrow$ 0.32 T starting at 13.3 mK and cooling to 1.2 ± 0.1 mK (extracted using the method described above), demonstrating a reduction in temperature upon demagnetization by a factor of 10. The other chips perform similar to D, thus substantiating the overall cooling scheme proposed here for reaching submillikelvin temperatures on multiple measurement leads.

Ideally, T_i of the Cu nuclei will be reduced by the same factor x as the B-field. To characterize the demagnetization process we introduce the efficiency $\xi_{B_f} = T_i/T_f \div B_i/B_f$ and find $\xi_{4\,T} = 88 \pm 3\,\%$, $\xi_{2\,T} = 80 \pm 3\,\%$, $\xi_{1\,T} = 63 \pm 3\,\%$ and $\xi_{0.3\,T} = 42 \pm 2\,\%$. $\xi < 100\,\%$ signifies nonadiabadicity, which becomes worse at lower magnetic field due to the smaller heat capacity of the nuclei (proportional to B_f^2). The dominant loss mechanism has been identified as a heat leak due to sweeping the B-field. We determined the magnitude to be $\sim 20\,{\rm nW}$ ($> 35\,{\rm nW\,mol^{-1}}$) at $1\,{\rm T\,h^{-1}}$ and $\sim 10\,{\rm nW}$

($> 18\,\mathrm{nW\,mol^{-1}}$) at $0.5\,\mathrm{T\,h^{-1}}$, which are 20 and 40 times greater than expected from a simple calculation of eddy currents [45]. The cause of the heat leak is presently unclear and under investigation.

Conclusions

In conclusion, we have laid out a method that enables the direct and simultaneous cooling of the electrical leads to a nanoscale device. Its strength is that it short circuits the two main bottlenecks of cooling electrons: thermal boundary resistance and electron-phonon coupling. We have addressed the technical challenges of constructing a parallel NR network, yielding a prototype that achieves a base temperature of $\sim 1\,\mathrm{mK}$. Future efforts will reduce the intrinsic heat leak and address the presently low efficiency (securing temperatures well within the microkelvin regime), further demonstrate ultralow temperatures directly in nanoscale devices and add an independently controllable magnetic field for the sample.

Acknowledgement

We thank G. R. Pickett, R. P. Haley, M. Paalanen, R. Blaauwgeers, G. Frossati and A. de Waard for their advice. This work was supported by the Swiss Nanoscience Institute, Swiss NSF, ERC Starting Grant and EU-FP7 MICROKELVIN network.

B AND Simulation

Source code for WaveMetrics IGOR Pro, written and run on version 6.3.

```
function initANDsim() //generate waves etc.
make/O/N=500000 testTn,testTnid,testTe,testB,testBramprate,testQdotB,
      testtimeh,testTeeffi,testTneffi,testCn
make/O/N=3 Bpoints,Bramp
Bpoints[0]=9;Bpoints[1]=1;Bpoints[2]=0.2
Bramp[0]=1;Bramp[1]=0.5;Bramp[2]=NaN
rebuild_GraphANDsim()
testANDsimExt(50e-9,4e-9)
end


function testANDsimExt(Qdyn,Qstat) //with varying Bdot and Qdot: heat leaks
   in [nW], temperatures are [K], ramp rates [T/h]
variable Qdyn,Qstat
variable Bi,Bf
variable Tpc=0.012
variable wlimit=0.1 //wlimit in [K] prints the warmup-time in the legends
   after which Te and Tn reach wlimit (wlimit>Tpc)
variable/G tmax
wave testTn,testTnid,testTe,testB,testBramprate,testQdotB,testtimeh,
      testTeeffi,testTneffi,testCn,Bpoints

wavestats/Q Bpoints
Bi=V_max
Bf=V_min

variable method=2
//parameters of doBandQ: "method"/"max heat leak Qmax"/"intrinsic heat leak
   while demagging Q0"
doBandQ(method,Qdyn,0) //while demagging: (1) with fixed heat leak
                //  (2) with max heat leak for max ramp rate
                //  (3) with heat leak calc. with eddy current formula
testQdotB[tmax,dimsize(testQdotB,0)]=Qstat
testTnid=Tpc*(testB[p]/Bi)

//artificial heat pulse
variable dopulse=0
if(dopulse==1)
variable timeset=5.5 //hours after demag finished
variable duration=900 //in [s]
variable Qstatpulse=100e-9
Findlevel testtimeh,timeset
testQdotB[V_LevelX,V_LevelX+duration]=Qstatpulse
endif

//temperature of nuclei while demagging
```

```
testTn[0]=Tpc
variable i,Tact,Tpre
Tpre=testTn[0]
for(i=1;i<=tmax;i+=1)
Tact=Tpre+testQdotB[i]*1/giveCn(testB[i-1],Tpre)-
      Tpre/testB[i]*testBramprate[i]/3600
testTn[i]=Tact
Tpre=Tact
endfor

//temperature of electrons while demagging
testTe[0,tmax]=testTn[p]*(1+1.2*testQdotB[p]/(3.22e-6*testB[p]^2))

//temperature of nuclei while warmup
Tpre=testTn[tmax-1]
for(i=tmax;i<=dimsize(testTn,0);i+=1)
Tact=Tpre+testQdotB[i]*1/giveCn(testB[i-1],Tpre)
testTn[i]=Tact
Tpre=Tact
endfor

//temperature of electrons while warmup
testTe[tmax,dimsize(testTe,0)]=testTn[p]*(1+1.2*testQdotB[p]/
      (3.22e-6*testB[p]^2))

//print warmup time in the legend
Findlevel/Q testTn,wlimit
string labelTnwarmup="t\B(T = "+num2str(wlimit*1000)+" mK)\M =
   "+num2str(round((testtimeh[V_levelX])*10)/10)+" h"

//avoid infinity and flash back to negative numbers
wavestats/Q testTe;testTe[V_maxloc,dimsize(testTe,0)]=NaN
wavestats/Q testTn;testTn[V_maxloc,dimsize(testTn,0)]=NaN

//calculate efficiencies and nuclear heat capacity
testTneffi=(Tpc*(testB[p]/Bi))/testTn[p]
testTeeffi=(Tpc*(testB[p]/Bi))/testTe[p]
testCn=giveCn(testB[p],testTn[p])

//update legend
DoWindow/F GraphANDsim
string Bopt
if(method==1)
   Bopt=", B\Bf,opt\M = "+num2str(round((1.2*Qdyn/3.22e-6)^0.5*1000)/1)+" mT"
else
   Bopt=""
endif

string labell="testANDsimExt:\rB\Bi\M = "+num2str(Bi)+" T, B\Bf\M =
   "+num2str(Bf)+" T, Q\Bdot,dyn\M = "+num2str(Qdyn*1e9)+" nW/mol,
```

```
    Q\Bdot,stat\M = "+num2str(Qstat*1e9)+" nW/mol\r"
labell=labell+"T\Bn,f\M = "+num2str(round(testTn[tmax-1]*1e6)/1e0)+"
    \F'Symbol'm\F'Arial'K, T\Be,f\M =
    "+num2str(round(testTe[tmax-1]*1e6)/1e0)+"
    \F'Symbol'm\F'Arial'K"+Bopt+"\r"
labell=labell+"warm-up: "+labelTnwarmup+"\r\\s(testTnid)
    T\Bn,ideal\M\t\\s(testTn) T\Bn\M\t\\s(testTe)
    T\Be\M\refficiency:\t\\s(testTneffi) nuclei\t\\s(testTeeffi) electron"
Legend/C/N=text0/J labell

//scale graph axes
Findlevel/Q testTn,0.02 //cut-off for T to rescale x-axis
SetAxis bottom *,round(testtimeh[V_levelX]+1)
SetAxis left 0,(Tpc+0.001)
SetAxis right 0,1.01
end


function giveCe(T)
variable T
variable Ce
Ce=0.691e-3*T
return Ce
end


function giveCn(B,T)
variable B,T
variable Cn
Cn=3.22e-6*(B/T)^2
return Cn
end


function doBandQ(method,Qmax,Q0)
variable method,Qmax,Q0
wave testBramprate,testtimeh,testB,testQdotB,Bpoints,Bramp
variable Bi=9
variable Bf=0.0
variable Bdot=1
variable/G tmax
variable,i,deltaB
variable ww=1.7e-3
variable dd=34e-3
variable hh=120e-3
variable RRR=500
variable nmol=1.95
variable prefac=(dd^2/16*
    (ww/dd)^2/(1+(ww/dd)^2))*(ww*dd*hh)/(17e-9/RRR)*2/nmol
tmax=0
```

```
testBramprate=0
for(i=0;i<(dimsize(Bpoints,0)-1);i+=1)
    testBramprate[tmax,tmax+(Bpoints[i]-Bpoints[i+1])/Bramp[i]*3600]=Bramp[i]
    tmax=tmax+(Bpoints[i]-Bpoints[i+1])/Bramp[i]*3600
endfor

testtimeh=(p-tmax)/3600
wavestats/Q Bpoints
testB=V_min

wavestats/Q Bramp

for(i=0;i<tmax;i+=1)
   if(i==0)
      testB[i]=Bpoints[0]
   else
      testB[i]=testB[i-1]-1/3600*testBramprate[i]
   endif

   if(method==1)   //version 1: with fixed heat leak
         testQdotB[i]=Qmax+Q0
      elseif(method==2) //version 2: with max heat leak Qmax for max ramp
          rate
      testQdotB[i]=Qmax*(testBramprate[i]/V_max)^2+Q0
   else            //version 3: with heat leak calculated with eddy current
       formula
      testQdotB[i]=prefac*(testBramprate[i]/3600)^2+Q0
   endif
endfor
end


function rebuild_GraphANDsim()
   PauseUpdate; Silent 1
   Display /W=(6,42.5,629.25,503) testTn vs testtimeh
   AppendToGraph testTe vs testtimeh
   AppendToGraph testTnid vs testtimeh
   AppendToGraph/R testTeeffi vs testtimeh
   AppendToGraph/R testTneffi vs testtimeh
   ModifyGraph lSize(testTn)=2
   ModifyGraph lStyle(testTeeffi)=3,lStyle(testTneffi)=3
   ModifyGraph
       rgb(testTn)=(0,65280,0),rgb(testTe)=(0,0,0),rgb(testTnid)=(0,0,65280)
   ModifyGraph rgb(testTeeffi)=(0,0,0),rgb(testTneffi)=(0,65280,0)
   ModifyGraph tick=2
   ModifyGraph zero(bottom)=9
   ModifyGraph mirror(bottom)=1
   ModifyGraph minor(bottom)=1
   ModifyGraph standoff=0
   ModifyGraph axThick=0.5
```

```
ModifyGraph prescaleExp(left)=3,prescaleExp(right)=2
ModifyGraph btLen=4
ModifyGraph btThick=0.5
ModifyGraph stLen=2
ModifyGraph stThick=0.5
ModifyGraph ttThick=0.5
ModifyGraph ftThick=0.5
ModifyGraph manTick(left)={0,2,0,0},manMinor(left)={3,2}
ModifyGraph manTick(right)={0,20,0,0},manMinor(right)={3,2}
Label left "T ( mK )"
Label bottom "t ( h )"
Label right "efficiency ( % )"
SetAxis left 0,0.013
SetAxis bottom -8.8,95
SetAxis right 0,1.01
ShowInfo
Legend/C/N=text0/J/A=MC/X=14.15/Y=32.18 "testANDsim:\rB\\Bi\\M = 9 T,
    B\\Bf\\M = 0.2 T, Q\\Bdot,dyn\\M = 50 nW/mol, Q\\Bdot,stat\\M = 1
    nW/mol"
AppendText "T\\Bn,f\\M = 372 \\F'Symbol'm\\F'Arial'K, T\\Be,f\\M = 545
    \\F'Symbol'm\\F'Arial'K, B\\Bf,opt\\M = 137 mT\rwarm-up: t\\B(T = 100
    mK)\\M = 95.9 h"
AppendText "\\s(testTnid) T\\Bn,ideal\\M\t\\s(testTn)
    T\\Bn\\M\t\\s(testTe) T\\Be\\M\refficiency:\t\\s(testTneffi)
    nuclei\t\\s(testTeeffi) electron"
DoWindow/C GraphANDsim

PauseUpdate; Silent 1   // building window...
Display /W=(640.5,42.5,1035,338.75) testQdotb vs testtimeh
AppendToGraph/R testB vs testtimeh
AppendToGraph/R=R2 testCn vs testtimeh
ModifyGraph margin(right)=85
ModifyGraph rgb(testB)=(39168,39168,39168),rgb(testCn)=(0,0,65280)
ModifyGraph tick=2
ModifyGraph mirror(bottom)=1
ModifyGraph minor(left)=1,minor(right)=1,minor(R2)=1
ModifyGraph sep(bottom)=15,sep(right)=1
ModifyGraph standoff=0
ModifyGraph axRGB(right)=(39168,39168,39168),axRGB(R2)=(0,0,65280)
ModifyGraph tlblRGB(right)=(39168,39168,39168),tlblRGB(R2)=(0,0,65280)
ModifyGraph alblRGB(right)=(39168,39168,39168),alblRGB(R2)=(0,0,65280)
ModifyGraph lblPos(right)=24,lblPos(R2)=38
ModifyGraph lblLatPos(right)=2
ModifyGraph prescaleExp(left)=9
ModifyGraph btLen=4
ModifyGraph btThick=0.5
ModifyGraph stLen=2
ModifyGraph stThick=0.5
ModifyGraph ttThick=0.5
ModifyGraph ftThick=0.5
```

```
   ModifyGraph freePos(R2)=29
   ModifyGraph manTick(right)={0,2,0,0},manMinor(right)={3,2}
   Label left "Q\\Bdot\\M ( nW )"
   Label bottom "t ( h )"
   Label right "B\\BAND\\M ( T )"
   Label R2 "C\\Bn\\M ( J/K )"
   SetAxis left 0,*
   SetAxis right 0,*
   SetAxis R2 0,*
   Legend/C/N=text0/J/F=0/A=MC/X=11.23/Y=24.20 "\\s(testQdotb) heat leak
      Q\\Bdot\\M\r\\s(testB) demag field B\\BAND\\M\r\\s(testCn) nuclear
      heat capacity C\\Bn\\M"
   DoWindow/C GraphANDsimAdd

   Edit/W=(639.75,366.5,888,502.25) Bpoints,Bramp
   ModifyTable format(Point)=1
   DoWindow/C tableBparam
End
```

References

[1] E. Schrödinger. *What Is Life?* (Cambridge University Press, 1944).

[2] W. Kohn. *An essay on condensed matter physics in the twentieth century.* Rev. Mod. Phys. **71**, 59 (1999).

[3] R. Hanson, L. P. Kouwenhoven, J. R. Petta, S. Tarucha, and L. M. K. Vandersypen. *Spins in few-electron quantum dots.* Rev. Mod. Phys. **79**, 1217 (2007).

[4] C. P. Scheller, T.-M. Liu, G. Barak, A. Yacoby, L. N. Pfeiffer, K. W. West, and D. M. Zumbühl. *Evidence for Helical Nuclear Spin Order in GaAs Quantum Wires.* Phys. Rev. Lett. **112**, 066801 (2014).

[5] B. Braunecker, P. Simon, and D. Loss. *Nuclear magnetism and electron order in interacting one-dimensional conductors.* Phys. Rev. B **80**, 165119 (2009).

[6] B. Braunecker, G. I. Japaridze, J. Klinovaja, and D. Loss. *Spin-selective Peierls transition in interacting one-dimensional conductors with spin-orbit interaction.* Phys. Rev. B **82**, 045127 (2010).

[7] W. Pan, J.-S. Xia, V. Shvarts, D. E. Adams, H. L. Stormer, D. C. Tsui, L. N. Pfeiffer, K. W. Baldwin, and K. W. West. *Exact Quantization of the Even-Denominator Fractional Quantum Hall State at $\nu = 5/2$ Landau Level Filling Factor.* Phys. Rev. Lett. **83**, 3530 (1999).

[8] J. P. Eisenstein, K. B. Cooper, L. N. Pfeiffer, and K. W. West. *Insulating and Fractional Quantum Hall States in the First Excited Landau Level.* Phys. Rev. Lett. **88**, 076801 (2002).

[9] G. A. Csáthy, J. S. Xia, C. L. Vicente, E. D. Adams, N. S. Sullivan, H. L. Stormer, D. C. Tsui, L. N. Pfeiffer, and K. W. West. *Tilt-Induced Localization and Delocalization in the Second Landau Level.* Phys. Rev. Lett. **94**, 146801 (2005).

[10] A. Kumar, G. A. Csáthy, M. J. Manfra, L. N. Pfeiffer, and K. W. West. *Nonconventional Odd-Denominator Fractional Quantum Hall States in the Second Landau Level.* Phys. Rev. Lett. **105**, 246808 (2010).

[11] W. Pan, K. W. Baldwin, K. W. West, L. N. Pfeiffer, and D. C. Tsui. *Fractional quantum Hall effect at Landau level filling $\nu = 4/11$.* Phys. Rev. B **91**, 041301 (2015).

[12] N. Samkharadze, I. Arnold, L. N. Pfeiffer, K. W. West, and G. A. Csáthy. *Observation of incompressibility at $\nu = 4/11$ and $\nu = 5/13$.* Phys. Rev. B **91**, 081109 (2015).

[13] J. K. Jain. *Composite-fermion approach for the fractional quantum Hall effect.* Phys. Rev. Lett. **63**, 199 (1989).

[14] K. S. Novoselov, A. K. Geim, S. V. Morozov, D. Jiang, M. I. Katsnelson, I. V. Grigorieva, S. V. Dubonos, and A. A. Firsov. *Two-dimensional gas of massless Dirac fermions in graphene.* Nature **438**, 197 (2005).

[15] Y. Zhang, Y.-W. Tan, H. L. Stormer, and P. Kim. *Experimental observation of the quantum Hall effect and Berry's phase in graphene.* Nature **438**, 201 (2005).

[16] E. Majorana. *Teoria simmetrica dell'elettrone e del positrone.* Il Nuovo Cimento **14**, 171 (1937).

[17] V. Mourik, K. Zuo, S. M. Frolov, S. R. Plissard, E. P. A. M. Bakkers, and L. P. Kouwenhoven. *Signatures of Majorana Fermions in Hybrid Superconductor-Semiconductor Nanowire Devices.* Science **336**, 1003 (2012).

[18] K. von Klitzing, G. Dorda, and M. Pepper. *New Method for High-Accuracy Determination of the Fine-Structure Constant Based on Quantized Hall Resistance.* Phys. Rev. Lett. **45**, 494 (1980).

[19] D. C. Tsui, H. L. Stormer, and A. C. Gossard. *Two-Dimensional Magnetotransport in the Extreme Quantum Limit.* Phys. Rev. Lett. **48**, 1559 (1982).

[20] N. Read. *Topological phases and quasiparticle braiding.* Physics Today **65**, 38 (2012).

[21] F. Wilczek. *Quantum Mechanics of Fractional-Spin Particles.* Phys. Rev. Lett. **49**, 957 (1982).

[22] G. Moore and N. Read. *Nonabelions in the fractional quantum Hall effect.* Nucl. Phys. B **360**, 362 (1991).

[23] S. Das Sarma, M. Freedman, and C. Nayak. *Topologically Protected Qubits from a Possible Non-Abelian Fractional Quantum Hall State.* Phys. Rev. Lett. **94**, 166802 (2005).

[24] I. P. Radu, J. B. Miller, C. M. Marcus, M. A. Kastner, L. N. Pfeiffer, and K. W. West. *Quasi-Particle Properties from Tunneling in the $\nu = 5/2$ Fractional Quantum Hall State.* Science **320**, 899 (2008).

[25] W. Li, G. A. Csáthy, D. C. Tsui, L. N. Pfeiffer, and K. W. West. *Scaling and Universality of Integer Quantum Hall Plateau-to-Plateau Transitions.* Phys. Rev. Lett. **94**, 206807 (2005).

[26] J. D. Watson, S. Mondal, G. A. Csáthy, M. J. Manfra, E. H. Hwang, S. Das Sarma, L. N. Pfeiffer, and K. W. West. *Scattering mechanisms in a high-mobility low-density carbon-doped (100) GaAs two-dimensional hole system.* Phys. Rev. B **83**, 241305 (2011).

[27] N. Deng, G. C. Gardner, S. Mondal, E. Kleinbaum, M. J. Manfra, and G. A. Csáthy. *$\nu = 5/2$ Fractional Quantum Hall State in the Presence of Alloy Disorder.* Phys. Rev. Lett. **112**, 116804 (2014).

[28] N. Deng, A. Kumar, M. J. Manfra, L. N. Pfeiffer, K. W. West, and G. A. Csáthy. *Collective Nature of the Reentrant Integer Quantum Hall States in the Second Landau Level.* Phys. Rev. Lett. **108**, 086803 (2012).

[29] J.-S. Xia, E. D. Adams, V. Shvarts, W. Pan, H. L. Stormer, and D. C. Tsui. *Ultra-low-temperature cooling of two-dimensional electron gas.* Physica B **280**, 491 (2000).

[30] J. S. Xia, W. Pan, C. L. Vicente, E. D. Adams, N. S. Sullivan, H. L. Stormer, D. C. Tsui, L. N. Pfeiffer, K. W. Baldwin, and K. W. West. *Electron Correlation in the Second Landau Level: A Competition Between Many Nearly Degenerate Quantum Phases.* Phys. Rev. Lett. **93**, 176809 (2004).

[31] W. Pan, J. Xia, H. Stormer, D. Tsui, C. Vicente, E. Adams, N. Sullivan, L. Pfeiffer, K. Baldwin, and K. West. *Experimental studies of the fractional quantum Hall effect in the first excited Landau level.* Phys. Rev. B **77**, 075307 (2008).

[32] A. Bid, N. Ofek, H. Inoue, M. Heiblum, C. L. Kane, V. Umansky, and D. Mahalu. *Observation of neutral modes in the fractional quantum Hall regime.* Nature **466**, 585 (2010).

[33] N. Samkharadze, A. Kumar, M. J. Manfra, L. N. Pfeiffer, K. W. West, and G. A. Csáthy. *Integrated electronic transport and thermometry at milliKelvin temperatures and in strong magnetic fields.* Rev. Sci. Instrum. **82**, 053902 (2011).

[34] D. T. McClure, W. Chang, C. M. Marcus, L. N. Pfeiffer, and K. W. West. *Fabry-Perot Interferometry with Fractional Charges.* Phys. Rev. Lett. **108**, 256804 (2012).

[35] R. M. Potok, I. G. Rau, H. Shtrikman, Y. Oreg, and D. Goldhaber-Gordon. *Observation of the two-channel Kondo effect.* Nature **446**, 167 (2007).

[36] I. Karakurt, V. J. Goldman, J. Liu, and A. Zaslavsky. *Absence of Compressible Edge Channel Rings in Quantum Antidots.* Phys. Rev. Lett. **87**, 146801 (2001).

[37] H. Inoue, A. Grivnin, N. Ofek, I. Neder, M. Heiblum, V. Umansky, and D. Mahalu. *Charge Fractionalization in the Integer Quantum Hall Effect.* Phys. Rev. Lett. **112**, 166801 (2014).

[38] H. Inoue, A. Grivnin, Y. Ronen, M. Heiblum, V. Umansky, and D. Mahalu. *Proliferation of neutral modes in fractional quantum Hall states.* Nat. Commun. **5**, 4067 (2014).

[39] W. Wendler, T. Herrmannsdörfer, S. Rehmann, and F. Pobell. *Electronic and nuclear magnetism in PtFex at milli-, and nanokelvin temperatures.* Europhys. Lett. **38**, 619 (1997).

[40] T. A. Knuuttila, J. T. Tuoriniemi, K. Lefmann, K. I. Juntunen, F. B. Rasmussen, and K. K. Nummila. *Polarized Nuclei in Normal and Superconducting Rhodium.* J. Low Temp. Phys. **123**, 65 (2001).

[41] G. R. Pickett. *Microkelvin physics.* Rep. Prog. Phys. **51**, 1295 (1988).

[42] R. C. Richardson and E. N. Smith. *Experimental Techniques in Condensed Matter Physics at Low Temperatures* (Westview Press, 1998).

[43] G. K. White and P. J. Meeson. *Experimental Techniques in Low-Temperature Physics* (Oxford University Press, 2002), 4th Edition.

[44] C. Enss and S. Hunklinger. *Low-Temperature Physics* (Springer, Berlin, 2005).

[45] F. Pobell. *Matter and Methods at Low Temperatures* (Springer, Berlin, 2007).

[46] G. Ventura and L. Risegari. *The Art of Cryogenics – Low Temperature Experimental Techniques* (Elsevier Ltd., 2008), 1st Edition.

[47] L. Casparis. *Ultra-Low Electron Temperatures in Nanostructured Samples.* PhD Thesis, Department of Physics, University of Basel, Switzerland (2014).

[48] D. Maradan. *Parallel Nuclear Refrigerators for Cooling Nanoscale Samples to Microkelvin Temperatures.* Master's Thesis, Department of Physics, University of Basel, Switzerland (2010).

[49] H. London, G. R. Clarke, and E. Mendoza. *Osmotic Pressure of ^{3}He in Liquid ^{4}He, with Proposals for a Refrigerator to Work below 1°K.* Phys. Rev. **128**, 1992 (1962).

[50] G. A. Vermeulen and G. Frossati. *Powerful dilution refrigerator for use in the study of polarized liquid ^{3}He and nuclear cooling.* Cryogenics **27**, 139 (1987).

[51] D. J. Cousins, S. N. Fisher, A. M. Guénault, R. P. Haley, I. E. Miller, G. R. Pickett, G. N. Plenderleith, P. Skyba, P. Y. A. Thibault, and M. G. Ward. *An Advanced Dilution Refrigerator Designed for the New Lancaster Microkelvin Facility.* J. Low Temp. Phys. **114**, 547 (1999).

[52] N. Kurti and F. Simon. *Experiments at Very Low Temperatures Obtained by the Magnetic Method. I. The Production of the Low Temperatures.* Proc. R. Soc. A **149**, 152 (1935).

[53] N. Kurti, F. N. H. Robinson, F. Simon, and D. A. Spohr. *Nuclear Cooling.* Nature **178**, 450 (1956).

[54] D. H. Nguyen, A. Sidorenko, M. Müller, S. Paschen, A. Waard, and G. Frossati. *The Vienna Nuclear Demagnetization Refrigerator.* Journal of Physics: Conference Series **400**, 052024 (2012).

[55] O. V. Lounasmaa. *Experimental Principles and Methods Below 1 K* (Academic Press, London, 1974).

[56] J. W. Ekin. *Experimental Techniques for Low-Temperature Measurements* (Oxford University Press, 2006).

[57] J. Pekola, R. Schoelkopf, and J. Ullom. *Cryogenics on a chip.* Physics Today **57**, 41 (2004).

[58] V. Venkatachalam, S. Hart, L. Pfeiffer, K. West, and A. Yacoby. *Local thermometry of neutral modes on the quantum Hall edge.* Nat. Phys. **8**, 676 (2012).

[59] N. W. Ashcroft and N. D. Mermin. *Solid State Physics* (Cengage Learning, 1976), 1st Edition.

[60] M. Khoshenevisan, W. Pratt, P. Schroeder, and S. Steenwyk. *Low-temperature resistivity and thermoelectric ratio of copper and gold.* Phys. Rev. B **19**, 3873 (1979).

[61] N. S. Lawson. *A simple heat switch for use at millikelvin temperatures.* Cryogenics **22**, 667 (1982).

[62] G. Frossati. *Experimental techniques: Methods for cooling below 300 mK.* J. Low Temp. Phys. **87**, 595 (1992).

[63] T. Bandi. *Ultra-low Electron Temperatures in 2D Electron Gases – by efficient silver sinter heat exchangers.* Master's Thesis, Department of Physics, University of Basel, Switzerland (2009).

[64] G. R. Pickett. *Cooling metals to the microkelvin regime, then and now.* Physica B **280**, 467 (2000).

[65] C. P. Scheller, S. Heizmann, K. Bedner, D. Giss, M. Meschke, D. M. Zumbühl, J. D. Zimmerman, and A. C. Gossard. *Silver-epoxy microwave filters and thermalizers for millikelvin experiments.* Appl. Phys. Lett. **104**, 211106 (2014).

[66] A. B. Zorin. *The thermocoax cable as the microwave frequency filter for single electron circuits.* Rev. Sci. Instrum. **66**, 4296 (1995).

[67] L. Conrad. *Quantum Hall Thermometry Down to Millikelvin Temperatures.* Master's Thesis, Department of Physics, University of Basel, Switzerland (2015).

[68] L. Greuter. *Fabrication and Characterization of Ohmic Contacts.* Project Thesis, Department of Physics, University of Basel, Switzerland (2009).

[69] A. C. Clark, K. K. Schwarzwälder, T. Bandi, D. Maradan, and D. M. Zumbühl. *Method for cooling nanostructures to microkelvin temperatures.* Rev. Sci. Instrum. **81**, 103904 (2010).

[70] W. Yao, T. A. Knuuttila, K. K. Nummila, J. E. Martikainen, A. S. Oja, and O. V. Lounasmaa. *A Versatile Nuclear Demagnetization Cryostat for Ultralow Temperature Research.* J. Low Temp. Phys. **120**, 121 (2000).

[71] C. Kittel. *Introduction to Solid State Physics* (John Wiley & Sons, 1996), 7th Edition.

[72] M. T. Huiku and M. T. Loponen. *Observation of a Magnetic Phase Transition in the Nuclear Spin System of Metallic Copper at Nanokelvin Temperatures.* Phys. Rev. Lett. **49**, 1288 (1982).

[73] M. Martinez, F. Alessandria, C. Arnaboldi, M. Barucci, C. Bucci, G. Frossati, A. Nucciotti, D. Schaeffer, M. Sisti, A. de Waard, and A. Woodcraft. *Progress on the CUORE Cryogenic System.* AIP Conf. Proc. **1185**, 693 (2009).

[74] M. Kubota, H. R. Folle, C. Buchal, R. M. Mueller, and F. Pobell. *Nuclear susceptibility and thermodynamic analysis of the nuclear specific heat of $PrNi_5$.* Physica B+C **108**, 1093 (1981).

[75] M. Assig, M. Etzkorn, A. Enders, W. Stiepany, C. R. Ast, and K. Kern. *A 10 mK scanning tunneling microscope operating in ultra high vacuum and high magnetic fields.* Rev. Sci. Instrum. **84**, 033903 (2013).

[76] V. Shvarts. Private communication (2011).

[77] R. Mitchell, A. D. Eastop, E. Faraj, and J. R. Hook. *The specific heat capacity and thermal conductivity of normal liquid ^3He.* J. Low Temp. Phys. **64**, 43 (1986).

[78] D. Paulson, M. Krusius, J. Wheatley, R. Safrata, M. Koláč, T. Těthal, K. Svec, and J. Matas. *Magnetic thermometry to below one millikelvin with lanthanum-diluted cerium magnesium nitrate.* J. Low Temp. Phys. **34**, 63 (1979).

[79] P. Simon and D. Loss. *Nuclear Spin Ferromagnetic Phase Transition in an Interacting Two Dimensional Electron Gas.* Phys. Rev. Lett. **98**, 156401 (2007).

[80] P. Simon, B. Braunecker, and D. Loss. *Magnetic ordering of nuclear spins in an interacting two-dimensional electron gas.* Phys. Rev. B **77**, 045108 (2008).

[81] C. Nayak, S. H. Simon, A. Stern, M. Freedman, and S. Das Sarma. *Non-Abelian anyons and topological quantum computation.* Rev. Mod. Phys. **80**, 1083 (2008).

[82] A. Stern. *Non-Abelian states of matter.* Nature **464**, 187 (2010).

[83] J. Huang, J.-S. Xia, D. C. Tsui, L. N. Pfeiffer, and K. W. West. *Disappearance of Metal-Like Behavior in GaAs Two-Dimensional Holes below 30 mK.* Phys. Rev. Lett. **98**, 226801 (2007).

[84] L. Spietz, R. J. Schoelkopf, and P. Pari. *Shot noise thermometry down to 10 mK.* Appl. Phys. Lett. **89**, 183123 (2006).

[85] J. P. Pekola, K. P. Hirvi, J. P. Kauppinen, and M. A. Paalanen. *Thermometry by Arrays of Tunnel Junctions.* Phys. Rev. Lett. **73**, 2903 (1994).

[86] M. Meschke, J. Engert, D. Heyer, and J. P. Pekola. *Comparison of Coulomb Blockade Thermometers with the International Temperature Scale PLTS-2000.* Int. J. Thermophys. **32**, 1378 (2011).

[87] M. Meschke, J. P. Pekola, F. Gay, R. E. Rapp, and H. Godfrin. *Electron Thermalization in Metallic Islands Probed by Coulomb Blockade Thermometry.* J. Low Temp. Phys. **134**, 1119 (2004).

[88] H. van Houten, C. W. J. Beenakker, and A. A. M. Staring. *Coulomb Blockade Oscillations in Semiconductor Nanostructures* (Published in Single Charge Tunneling, edited by H. Grabert and M. H. Devoret, NATO ASI Series B294, Plenum, New York, 1992).

[89] M. A. Kastner. *The single-electron transistor*. Rev. Mod. Phys. **64**, 849 (1992).

[90] L. P. Kouwenhoven, C. M. Marcus, P. L. McEuen, S. Tarucha, R. M. Westervelt, and N. S. Wingreen. *Electron transport in quantum dots*, volume 345 (Proceedings of the NATO Advanced Study Institute on Mesoscopic Electron Transport, Springer, 1996).

[91] D. Loss and D. P. DiVincenzo. *Quantum computation with quantum dots*. Phys. Rev. A **57**, 120 (1998).

[92] C. Jayaprakash, H. R. Krishna-murthy, and J. W. Wilkins. *Two-Impurity Kondo Problem*. Phys. Rev. Lett. **47**, 737 (1981).

[93] P. Nozières and A. Blandin. *Kondo effect in real metals*. J. Phys. France **41**, 193 (1980).

[94] A. Zawadowski. *Kondo-like State in a Simple Model for Metallic Glasses*. Phys. Rev. Lett. **45**, 211 (1980).

[95] R. Willett, J. P. Eisenstein, H. L. Stormer, D. C. Tsui, A. C. Gossard, and J. H. English. *Observation of an even-denominator quantum number in the fractional quantum Hall effect*. Phys. Rev. Lett. **59**, 1776 (1987).

[96] Y. C. Chung, M. Heiblum, and V. Umansky. *Scattering of Bunched Fractionally Charged Quasiparticles*. Phys. Rev. Lett. **91**, 216804 (2003).

[97] L. Casparis, M. Meschke, D. Maradan, A. C. Clark, C. P. Scheller, K. K. Schwarzwälder, J. P. Pekola, and D. M. Zumbühl. *Metallic Coulomb blockade thermometry down to 10 mK and below*. Rev. Sci. Instrum. **83**, 083903 (2012).

[98] A. Rossi, T. Ferrus, and D. A. Williams. *Electron temperature in electrically isolated Si double quantum dots*. Appl. Phys. Lett. **100**, 133503 (2012).

[99] A. Mavalankar, S. J. Chorley, J. Griffiths, G. A. C. Jones, I. Farrer, D. A. Ritchie, and C. G. Smith. *A non-invasive electron thermometer based on charge sensing of a quantum dot*. Appl. Phys. Lett. **103**, 133116 (2013).

[100] P. Torresani, M. J. Martínez-Pérez, S. Gasparinetti, J. Renard, G. Biasiol, L. Sorba, F. Giazotto, and S. De Franceschi. *Nongalvanic primary thermometry of a two-dimensional electron gas*. Phys. Rev. B **88**, 245304 (2013).

[101] A. G. Huibers, J. A. Folk, S. R. Patel, C. M. Marcus, C. I. Duruöz, and J. S. Harris. *Low-Temperature Saturation of the Dephasing Time and Effects of Microwave Radiation on Open Quantum Dots*. Phys. Rev. Lett. **83**, 5090 (1999).

[102] C. Altimiras, H. le Sueur, U. Gennser, A. Cavanna, D. Mailly, and F. Pierre. *Non-equilibrium edge-channel spectroscopy in the integer quantum Hall regime.* Nat. Phys. **6**, 34 (2010).

[103] O. E. Dial, M. D. Shulman, S. P. Harvey, H. Bluhm, V. Umansky, and A. Yacoby. *Charge Noise Spectroscopy Using Coherent Exchange Oscillations in a Singlet-Triplet Qubit.* Phys. Rev. Lett. **110**, 146804 (2013).

[104] A. K. M. Wennberg, S. N. Ytterboe, C. M. Gould, H. M. Bozler, J. Klem, and H. Morkoç. *Electron heating in a multiple-quantum-well structure below 1 K.* Phys. Rev. B **34**, 4409 (1986).

[105] P. L. Gammel, D. J. Bishop, J. P. Eisenstein, J. H. English, A. C. Gossard, R. Ruel, and H. L. Stormer. *Ultralow-temperature behavior of the $\nu = 5/2$ fractional quantum Hall effect.* Phys. Rev. B **38**, 10128 (1988).

[106] H. L. Edwards, Q. Niu, and A. L. de Lozanne. *A quantum-dot refrigerator.* Appl. Phys. Lett. **63**, 1815 (1993).

[107] M. Field, C. G. Smith, M. Pepper, D. A. Ritchie, J. E. F. Frost, G. A. C. Jones, and D. G. Hasko. *Measurements of Coulomb blockade with a noninvasive voltage probe.* Phys. Rev. Lett. **70**, 1311 (1993).

[108] J. M. Elzerman, R. Hanson, J. S. Greidanus, L. H. Willems van Beveren, S. De Franceschi, L. M. K. Vandersypen, S. Tarucha, and L. P. Kouwenhoven. *Few-electron quantum dot circuit with integrated charge read out.* Phys. Rev. B **67**, 161308 (2003).

[109] L. DiCarlo, H. J. Lynch, A. C. Johnson, L. I. Childress, K. Crockett, C. M. Marcus, M. P. Hanson, and A. C. Gossard. *Differential Charge Sensing and Charge Delocalization in a Tunable Double Quantum Dot.* Phys. Rev. Lett. **92**, 226801 (2004).

[110] S. Gasparinetti, M. J. Martínez-Pérez, S. de Franceschi, J. P. Pekola, and F. Giazotto. *Nongalvanic thermometry for ultracold two-dimensional electron domains.* J. Appl. Phys. **100**, 253502 (2012).

[111] G. Granger, D. Taubert, C. E. Young, L. Gaudreau, A. Kam, S. A. Studenikin, P. Zawadzki, D. Harbusch, D. Schuh, W. Wegscheider, Z. R. Wasilewski, A. A. Clerk, S. Ludwig, and A. S. Sachrajda. *Quantum interference and phonon-mediated back-action in lateral quantum-dot circuits.* Nat. Phys. **8**, 522 (2012).

[112] W. G. van der Wiel, S. De Franceschi, J. M. Elzerman, T. Fujisawa, S. Tarucha, and L. P. Kouwenhoven. *Electron transport through double quantum dots.* Rev. Mod. Phys. **75**, 1 (2002).

[113] A. V. Kuhlmann, J. Houel, A. Ludwig, L. Greuter, D. Reuter, A. D. Wieck, M. Poggio, and R. J. Warburton. *Charge noise and spin noise in a semiconductor quantum device.* Nat. Phys. **9**, 570 (2013).

[114] S. Amasha, K. MacLean, I. P. Radu, D. M. Zumbühl, M. A. Kastner, M. P. Hanson, and A. C. Gossard. *Electrical Control of Spin Relaxation in a Quantum Dot.* Phys. Rev. Lett. **100**, 046803 (2008).

[115] M. Ciorga, A. S. Sachrajda, P. Hawrylak, C. Gould, P. Zawadzki, S. Jullian, Y. Feng, and Z. Wasilewski. *Addition spectrum of a lateral dot from Coulomb and spin-blockade spectroscopy.* Phys. Rev. B **61**, R16315 (2000).

[116] M. Pioro-Ladrière, J. H. Davies, A. R. Long, A. S. Sachrajda, L. Gaudreau, P. Zawadzki, J. Lapointe, J. Gupta, Z. Wasilewski, and S. Studenikin. *Origin of switching noise in GaAs/AlGaAs lateral gated devices.* Phys. Rev. B **72**, 115331 (2005).

[117] C. Buizert, F. H. L. Koppens, M. Pioro-Ladrière, H.-P. Tranitz, I. T. Vink, S. Tarucha, W. Wegscheider, and L. M. K. Vandersypen. *In-situ Reduction of Charge Noise in GaAs/$Al_xGa_{1-x}As$ Schottky-Gated Devices.* Phys. Rev. Lett. **101**, 226603 (2008).

[118] C. Barthel, M. Kjærgaard, J. Medford, M. Stopa, C. M. Marcus, M. P. Hanson, and A. C. Gossard. *Fast sensing of double-dot charge arrangement and spin state with a radio-frequency sensor quantum dot.* Phys. Rev. B **81**, 161308 (2010).

[119] D. Paget, G. Lampel, B. Sapoval, and V. I. Safarov. *Low field electron-nuclear spin coupling in gallium arsenide under optical pumping conditions.* Phys. Rev. B **15**, 5780 (1977).

[120] W. A. Coish and D. Loss. *Hyperfine interaction in a quantum dot: Non-Markovian electron spin dynamics.* Phys. Rev. B **70**, 195340 (2004).

[121] R. H. Morf. *Transition from Quantum Hall to Compressible States in the Second Landau Level: New Light on the* $= 5/2$ *Enigma.* Phys. Rev. Lett. **80**, 1505 (1998).

[122] R. Morf, N. d'Ambrumenil, and S. Das Sarma. *Excitation gaps in fractional quantum Hall states: An exact diagonalization study.* Phys. Rev. B **66**, 075408 (2002).

[123] J. P. Eisenstein, R. Willett, H. L. Stormer, D. C. Tsui, A. C. Gossard, and J. H. English. *Collapse of the even-denominator fractional quantum Hall effect in tilted fields.* Phys. Rev. Lett. **61**, 997 (1988).

[124] A. Y. Kitaev. *Fault-tolerant quantum computation by anyons.* Ann. Phys. **303**, 2 (2003).

[125] A. Y. Kitaev. *Anyons in an exactly solved model and beyond.* Ann. Phys. **321**, 2 (2006).

[126] M. Dolev, M. Heiblum, V. Umansky, A. Stern, and D. Mahalu. *Observation of a quarter of an electron charge at the* $\nu = 5/2$ *quantum Hall state.* Nature **452**, 829 (2008).

[127] J. B. Miller, I. P. Radu, D. M. Zumbühl, E. M. Levenson-Falk, M. A. Kastner, C. M. Marcus, L. N. Pfeiffer, and K. W. West. *Fractional quantum Hall effect in a quantum point contact at filling fraction 5/2.* Nat. Phys. **3**, 561 (2007).

[128] R. L. Willett, L. N. Pfeiffer, and K. W. West. *Measurement of filling factor 5/2 quasiparticle interference with observation of charge $e/4$ and $e/2$ period oscillations.* Proc. Natl. Acad. Sci. U.S.A. **106**, 8853 (2009).

[129] R. L. Willett, L. N. Pfeiffer, and K. W. West. *Alternation and interchange of $e/4$ and $e/2$ period interference oscillations consistent with filling factor 5/2 non-Abelian quasiparticles.* Phys. Rev. B **82**, 205301 (2010).

[130] R. L. Willett, C. Nayak, K. Shtengel, L. N. Pfeiffer, and K. W. West. *Magnetic-Field-Tuned Aharonov-Bohm Oscillations and Evidence for Non-Abelian Anyons at $\nu = 5/2$.* Phys. Rev. Lett. **111**, 186401 (2013).

[131] L. Tiemann, G. Gamez, N. Kumada, and K. Muraki. *Unraveling the Spin Polarization of the $\nu = 5/2$ Fractional Quantum Hall State.* Science **335**, 828 (2012).

[132] H. Choi, W. Kang, S. Das Sarma, L. Pfeiffer, and K. West. *Activation gaps of fractional quantum Hall effect in the second Landau level.* Phys. Rev. B **77**, 081301(R) (2008).

[133] J. Nuebler, V. Umansky, R. Morf, M. Heiblum, K. von Klitzing, and J. Smet. *Density dependence of the $\nu = 5/2$ energy gap: Experiment and theory.* Phys. Rev. B **81**, 035316 (2010).

[134] G. Gamez and K. Muraki. *$\nu = 5/2$ fractional quantum Hall state in low-mobility electron systems: Different roles of disorder.* Phys. Rev. B **88**, 075308 (2013).

[135] C. Dean, B. Piot, P. Hayden, S. Das Sarma, G. Gervais, L. Pfeiffer, and K. West. *Intrinsic Gap of the $\nu = 5/2$ Fractional Quantum Hall State.* Phys. Rev. Lett. **100**, 146803 (2008).

[136] W. Pan, J. S. Xia, H. L. Stormer, D. C. Tsui, C. L. Vicente, E. D. Adams, N. S. Sullivan, L. N. Pfeiffer, K. W. Baldwin, and K. W. West. *Low temperature electronic transports in the presence of a density gradient.* Solid State Commun. **140**, 88 (2006).

[137] W. Pan, J. Xia, H. Stormer, D. Tsui, C. Vicente, E. Adams, N. Sullivan, L. Pfeiffer, K. Baldwin, and K. West. *Quantization of the Diagonal Resistance: Density Gradients and the Empirical Resistance Rule in a 2D System.* Phys. Rev. Lett. **95**, 066808 (2005).

[138] D. Maradan, L. Casparis, T.-M. Liu, D. E. F. Biesinger, C. P. Scheller, D. M. Zumbühl, J. D. Zimmerman, and A. C. Gossard. *GaAs Quantum Dot Thermometry Using Direct Transport and Charge Sensing.* J. Low Temp. Phys. **175**, 784 (2014).

[139] D. A. Syphers and P. J. Stiles. *Contiguous two-dimensional regions in the quantized Hall regime.* Phys. Rev. B **32**, 6620 (1985).

[140] S. Washburn, A. B. Fowler, H. Schmid, and D. Kern. *Quantized Hall effect in the presence of backscattering.* Phys. Rev. Lett. **61**, 2801 (1988).

[141] R. J. Haug, A. H. MacDonald, P. Streda, and K. von Klitzing. *Quantized Multichannel Magnetotransport through a Barrier in Two Dimensions.* Phys. Rev. Lett. **61**, 2797 (1988).

[142] A. M. Chang and J. E. Cunningham. *Transport evidence for phase separation into spatial regions of different fractional quantum Hall fluids near the boundary of a two-dimensional electron gas.* Phys. Rev. Lett. **69**, 2114 (1992).

[143] B. I. Halperin. *Quantized Hall conductance, current-carrying edge states, and the existence of extended states in a two-dimensional disordered potential.* Phys. Rev. B **25**, 2185 (1982).

[144] M. Büttiker. *Absence of backscattering in the quantum Hall effect in multiprobe conductors.* Phys. Rev. B **38**, 9375 (1988).

[145] R. Ilan, N. Cooper, and A. Stern. *Longitudinal resistance of a quantum Hall system with a density gradient.* Phys. Rev. B **73**, 235333 (2006).

[146] E. M. Kendirlik, S. Sirt, S. B. Kalkan, W. Dietsche, W. Wegscheider, S. Ludwig, and A. Siddiki. *Anomalous resistance overshoot in the integer quantum Hall effect.* Sci. Rep. **3**, 3133 (2013).

[147] F. Fischer. *Growth and Electronic Properties of Two-Dimensional Systems on (110) Oriented GaAs.* PhD Thesis, Fakultät für Physik, Technische Universität München, Walter Schottky Institut, Germany (2004).

[148] F. Fischer, M. Grayson, E. Schuberth, D. Schuh, M. Bichler, and G. Abstreiter. *New anisotropic behavior of quantum Hall resistance in (110) GaAs heterostructures at mK temperatures and fractional filling factors.* Physica E **22**, 108 (2004).

[149] F. Giazotto, T. T. Heikkilä, A. Luukanen, A. M. Savin, and J. P. Pekola. *Opportunities for mesoscopics in thermometry and refrigeration: Physics and applications.* Rev. Mod. Phys. **78**, 217 (2006).

[150] S. Gasparinetti, F. Deon, G. Biasiol, L. Sorba, F. Beltram, and F. Giazotto. *Probing the local temperature of a two-dimensional electron gas microdomain with a quantum dot: Measurement of electron-phonon interaction.* Phys. Rev. B **83**, 201306 (2011).

[151] M. Nahum and J. M. Martinis. *Ultrasensitive-hot-electron microbolometer.* Appl. Phys. Lett. **63**, 3075 (1993).

[152] M. Nahum, T. M. Eiles, and J. M. Martinis. *Electronic microrefrigerator based on a normal - insulator - superconductor tunnel junction.* Appl. Phys. Lett. **65**, 3123 (1994).

[153] A. V. Feshchenko, J. V. Koski, and J. P. Pekola. *Experimental realization of a Coulomb blockade refrigerator.* Phys. Rev. B **90**, 201407(R) (2014).

[154] A. M. Clark, A. Williams, S. T. Ruggiero, M. L. van den Berg, and J. N. Ullom. *Practical electron-tunneling refrigerator.* Appl. Phys. Lett. **84**, 625 (2004).

[155] N. A. Miller, G. C. O'Neil, J. A. Beall, G. C. Hilton, K. D. Irwin, D. R. Schmidt, L. R. Vale, and J. N. Ullom. *High resolution x-ray transition-edge sensor cooled by tunnel junction refrigerators.* Appl. Phys. Lett. **92**, 163501 (2008).

[156] P. Dubos, H. Courtois, B. Pannetier, F. K. Wilhelm, A. D. Zaikin, and G. Schön. *Josephson critical current in a long mesoscopic S-N-S junction.* Phys. Rev. B **63**, 064502 (2001).

[157] L. Spietz, K. W. Lehnert, I. Siddiqi, and R. J. Schoelkopf. *Primary Electronic Thermometry Using the Shot Noise of a Tunnel Junction.* Science **300**, 1929 (2003).

[158] L. Spietz. *The Shot Noise Thermometer.* PhD Thesis, Yale University, Connecticut, United States (2006).

[159] G. Frossati. *Obtaining ultralow temperatures by dilution of ^{3}He into ^{4}He.* Journal de Physique Colloques **39**, 1578 (1978).

[160] M. M. Leivo, J. P. Pekola, and D. V. Averin. *Efficient Peltier refrigeration by a pair of normal metal/insulator/superconductor junctions.* Appl. Phys. Lett. **68**, 1996 (1996).

[161] P. A. Fisher, J. N. Ullom, and M. Nahum. *High-power on-chip microrefrigerator based on a normal-metal/insulator/superconductor tunnel junction.* Appl. Phys. Lett. **74**, 2705 (1999).

[162] J. T. Muhonen, M. Meschke, and J. P. Pekola. *Micrometre-scale refrigerators.* Rep. Prog. Phys. **75**, 046501 (2012).

[163] H. Paik, D. I. Schuster, L. S. Bishop, G. Kirchmair, G. Catelani, A. P. Sears, B. R. Johnson, M. J. Reagor, L. Frunzio, L. I. Glazman, S. M. Girvin, M. H. Devoret, and R. J. Schoelkopf. *Observation of High Coherence in Josephson Junction Qubits Measured in a Three-Dimensional Circuit QED Architecture.* Phys. Rev. Lett. **107**, 240501 (2011).

[164] M. Tinkham. *Introduction to superconductivity* (Dover, New York, 1996), 2$^{\text{nd}}$ Edition.

[165] J. P. Pekola, V. F. Maisi, S. Kafanov, N. Chekurov, A. Kemppinen, Y. A. Pashkin, O.-P. Saira, M. Möttönen, and J. S. Tsai. *Environment-Assisted Tunneling as an Origin of the Dynes Density of States.* Phys. Rev. Lett. **105**, 026803 (2010).

[166] R. C. Dynes, V. Narayanamurti, and J. P. Garno. *Direct Measurement of Quasiparticle-Lifetime Broadening in a Strong-Coupled Superconductor.* Phys. Rev. Lett. **41**, 1509 (1978).

[167] H. Courtois, S. Rajauria, P. Gandit, F. W. J. Hekking, and B. Pannetier. *Inherent Thermometry in a Hybrid Superconducting Tunnel Junction.* J. Low Temp. Phys. **153**, 325 (2008).

[168] T. Greibe, M. P. V. Stenberg, C. M. Wilson, T. Bauch, V. S. Shumeiko, and P. Delsing. *Are "Pinholes" the Cause of Excess Current in Superconducting Tunnel Junctions? A Study of Andreev Current in Highly Resistive Junctions.* Phys. Rev. Lett. **106**, 097001 (2011).

[169] H. Jung, Y. Kim, K. Jung, H. Im, Y. A. Pashkin, O. Astafiev, Y. Nakamura, H. Lee, Y. Miyamoto, and J. S. Tsai. *Potential barrier modification and interface states formation in metal-oxide-metal tunnel junctions.* Phys. Rev. B **80**, 125413 (2009).

[170] M. R. Nevala, S. Chaudhuri, J. Halkosaari, J. T. Karvonen, and I. J. Maasilta. *Sub-micron normal-metal/insulator/superconductor tunnel junction thermometer and cooler using Nb.* Appl. Phys. Lett. **101**, 112601 (2012).

[171] S. Chaudhuri, M. R. Nevala, and I. J. Maasilta. *Niobium nitride-based normal metal-insulator-superconductor tunnel junction microthermometer.* Appl. Phys. Lett. **102**, 132601 (2013).

[172] D. J. van Woerkom, A. Geresdi, and L. P. Kouwenhoven. *One minute parity lifetime of a NbTiN Cooper-pair transistor.* Nat. Phys. **11**, 547 (2015).

[173] H. Q. Nguyen, M. Meschke, H. Courtois, and J. P. Pekola. *Sub-50 mK electronic cooling with large-area superconducting tunnel junctions.* Phys. Rev. Appl. **2**, 054001 (2014).

[174] O.-P. Saira, A. Kemppinen, V. F. Maisi, and J. P. Pekola. *Vanishing quasiparticle density in a hybrid Al/Cu/Al single-electron transistor.* Phys. Rev. B **85**, 012504 (2012).

[175] J. M. Hergenrother, J. G. Lu, M. T. Tuominen, D. C. Ralph, and M. Tinkham. *Photon-activated switch behavior in the single-electron transistor with a superconducting island.* Phys. Rev. B **51**, 9407 (1995).

[176] F. W. J. Hekking and Y. V. Nazarov. *Subgap conductivity of a superconductor–normal-metal tunnel interface.* Phys. Rev. B **49**, 6847 (1994).

[177] T. A. Fulton and G. J. Dolan. *Observation of single-electron charging effects in small tunnel junctions.* Phys. Rev. Lett. **59**, 109 (1987).

[178] M. Steinacher. Low Noise/High Stability I to V converter SP893, Electronics Lab, Physics Department, University of Basel, Switzerland.

[179] J. Jochum, C. Mears, S. Golwala, B. Sadoulet, J. P. Castle, M. F. Cunningham, O. B. Drury, M. Frank, S. E. Labov, F. P. Lipschultz, H. Netel, and B. Neuhauser. *Modeling the power flow in normal conductor-insulator-superconductor junctions.* J. Appl. Phys. **83**, 3217 (1998).

[180] V. F. Maisi, O.-P. Saira, Y. A. Pashkin, J. S. Tsai, D. V. Averin, and J. P. Pekola. *Real-Time Observation of Discrete Andreev Tunneling Events.* Phys. Rev. Lett. **106**, 217003 (2011).

[181] T. Aref, V. F. Maisi, M. V. Gustafsson, P. Delsing, and J. P. Pekola. *Andreev tunneling in charge pumping with SINIS turnstiles.* Europhys. Lett. **96**, 37008 (2011).

[182] P. J. de Visser, J. J. A. Baselmans, P. Diener, S. J. C. Yates, A. Endo, and T. M. Klapwijk. *Number Fluctuations of Sparse Quasiparticles in a Superconductor.* Phys. Rev. Lett. **106**, 167004 (2011).

[183] H. S. Knowles, V. F. Maisi, and J. P. Pekola. *Probing quasiparticle excitations in a hybrid single electron transistor.* Appl. Phys. Lett. **100**, 262601 (2012).

[184] A. V. Timofeev, C. P. Garcia, N. B. Kopnin, A. M. Savin, M. Meschke, F. Giazotto, and J. P. Pekola. *Recombination-Limited Energy Relaxation in a Bardeen-Cooper-Schrieffer Superconductor.* Phys. Rev. Lett. **102**, 017003 (2009).

[185] J. P. Pekola, A. J. Manninen, M. M. Leivo, K. Arutyunov, J. K. Suoknuuti, T. I. Suppula, and B. Collaudin. *Microrefrigeration by quasiparticle tunnelling in NIS and SIS junctions.* Physica B **280**, 485 (2000).

[186] K. Uhlig and W. Hehn. *^{3}He/^{4}He dilution refrigerator combined with Gifford-McMahon cooler.* Cryogenics **34**, 587 (1994).

[187] K. Uhlig. *^{3}He/^{4}He dilution refrigerator with pulse-tube refrigerator precooling.* Cryogenics **42**, 73 (2002).

[188] M. Pelliccione, A. Sciambi, J. Bartel, A. J. Keller, and D. Goldhaber-Gordon. *Design of a scanning gate microscope for mesoscopic electron systems in a cryogen-free dilution refrigerator.* Rev. Sci. Instrum. **84** (2013).

[189] G. Batey, A. Casey, M. N. Cuthbert, A. J. Matthews, J. Saunders, and A. Shibahara. *A microkelvin cryogen-free experimental platform with integrated noise thermometry.* New J. Phys. **15**, 113034 (2013).

[190] I. Todoshchenko, J.-P. Kaikkonen, R. Blaauwgeers, P. J. Hakonen, and A. Savin. *Dry demagnetization cryostat for sub-millikelvin helium experiments: Refrigeration and thermometry.* Rev. Sci. Instrum. **85**, 085106 (2014).

[191] BlueFors Cryogenics Oy Ltd., Helsinki, Finland.

[192] Cryomech Inc., Syracuse, USA.

[193] S. Brunauer, P. H. Emmett, and E. Teller. *Adsorption of Gases in Multimolecular Layers.* J. Am. Chem. Soc. **60**, 309 (1938).

[194] S. Hess. *Microkelvin Chip Carrier.* Project Thesis, Department of Physics, University of Basel, Switzerland (2012).

[195] J. B. Johnson. *Thermal Agitation of Electricity in Conductors.* Phys. Rev. **32**, 97 (1928).

[196] H. Nyquist. *Thermal Agitation of Electric Charge in Conductors.* Phys. Rev. **32**, 110 (1928).

[197] D. R. White, R. Galleano, A. Actis, H. Brixy, M. De Groot, J. Dubbeldam, A. L. Reesink, F. Edler, H. Sakurai, R. L. Shepard, and J. C. Gallop. *The status of Johnson noise thermometry.* Metrologia **33**, 325 (1996).

[198] J. Engert, J. Beyer, D. Drung, A. Kirste, and M. Peters. *A Noise Thermometer for Practical Thermometry at Low Temperatures.* Int. J. Thermophys. **28**, 1800 (2007).

[199] J. Engert, J. Beyer, D. Drung, A. Kirste, D. Heyer, A. Fleischmann, C. Enss, and H.-J. Barthelmess. *Practical noise thermometers for low temperatures.* JPCS **150**, 012012 (2009).

[200] C. P. Lusher, J. Li, V. A. Maidanov, M. E. Digby, H. Dyball, A. Casey, J. Nyéki, V. V. Dmitriev, B. P. Cowan, and J. Saunders. *Current sensing noise thermometry using a low T_c DC SQUID preamplifier.* Meas. Sci. Technol. **12**, 1 (2001).

[201] A. Casey, F. Arnold, L. V. Levitin, C. P. Lusher, J. Nyéki, J. Saunders, A. Shibahara, H. v. d. Vliet, B. Yager, D. Drung, T. Schurig, G. Batey, M. N. Cuthbert, and A. J. Matthews. *Current Sensing Noise Thermometry: A Fast Practical Solution to Low Temperature Measurement.* J. Low Temp. Phys. **175**, 764 (2014).

[202] H.-Y. Hao, M. Neumann, C. Enss, and A. Fleischmann. *Contactless technique for thermal conductivity measurement at very low temperature.* Rev. Sci. Instrum. **75**, 2718 (2004).

[203] D. Rothfuss, A. Reiser, A. Fleischmann, and C. Enss. *Noise thermometry at ultra low temperatures.* Appl. Phys. Lett. **103**, 052605 (2013).

[204] Magnicon GmbH, Hamburg, Germany.

[205] J. Clarke and A. I. Braginski. *The SQUID Handbook: Fundamentals and Technology of SQUIDs and SQUID systems* (Wiley-VCH, Weinheim, 2004), 1st Edition.

[206] T. Varpula and T. Poutanen. *Magnetic field fluctuations arising from thermal motion of electric charge in conductors.* J. Appl. Phys. **55**, 4015 (1984).

[207] J. Beyer, M. Schmidt, J. Engert, S. AliValiollahi, and H. J. Barthelmess. *Reference measurements of SQUID-based magnetic-field fluctuation thermometers.* Supercond. Sci. Technol. **26**, 065010 (2013).

[208] J. Beyer, D. Drung, A. Kirste, J. Engert, A. Netsch, A. Fleischmann, and C. Enss. *A Magnetic-Field-Fluctuation Thermometer for the mK Range Based on SQUID-Magnetometry.* IEEE Trans Appl Supercond **17**, 760 (2007).

[209] P. Falferi and R. Mezzena. *A Simple Wide-Range Noise Thermometer With DC SQUID Readout for Operation Down to 10 mK.* Applied Superconductivity, IEEE Transactions on **21**, 48 (2011).

[210] F. C. Wellstood, C. Urbina, and J. Clarke. *Low-frequency noise in DC superconducting quantum interference devices below 1 K.* Appl. Phys. Lett. **50**, 772 (1987).

[211] K. Gloos, C. Mitschka, F. Pobell, and P. Smeibidl. *Thermal conductivity of normal and superconducting metals.* Cryogenics **30**, 14 (1990).

[212] V. J. Goldman and B. Su. *Resonant Tunneling in the Quantum Hall Regime: Measurement of Fractional Charge.* Science **267**, 1010 (1995).

[213] A. Kou, C. M. Marcus, L. N. Pfeiffer, and K. W. West. *Coulomb Oscillations in Antidots in the Integer and Fractional Quantum Hall Regimes.* Phys. Rev. Lett. **108**, 256803 (2012).

[214] R. Zielke, B. Braunecker, and D. Loss. *Cotunneling in the $\nu = 5/2$ fractional quantum Hall regime.* Phys. Rev. B **86**, 235307 (2012).

[215] J. Klinovaja and D. Loss. *Integer and fractional quantum Hall effect in a strip of stripes.* EPJ B **87**, 171 (2014).

[216] T. Meng, P. Stano, J. Klinovaja, and D. Loss. *Helical nuclear spin order in a strip of stripes in the quantum Hall regime.* EPJ B **87**, 203 (2014).

[217] I. G. Rau, S. Amasha, M. Grobis, R. M. Potok, H. Shtrikman, and D. Goldhaber-Gordon. *Nonsaturating Dephasing Time at Low Temperature in an Open Quantum Dot.* arXiv:1210.0087 (2012).

[218] O. Zilberberg, A. Carmi, and A. Romito. *Measuring cotunneling in its wake.* Phys. Rev. B **90**, 205413 (2014).

[219] P. Stano. Private communication (2014).

[220] A. J. Keller, S. Amasha, I. Weymann, C. P. Moca, I. G. Rau, J. A. Katine, H. Shtrikman, G. Zaránd, and D. Goldhaber-Gordon. *Emergent SU(4) Kondo physics in a spin–charge-entangled double quantum dot.* Nat. Phys. **10**, 145 (2014).

[221] S. Chesi and D. Loss. *Quantum Hall Ferromagnetic States and Spin-Orbit Interactions in the Fractional Regime.* Phys. Rev. Lett. **101**, 146803 (2008).

[222] P. J. Hakonen, R. T. Vuorinen, and J. E. Martikainen. *Nuclear antiferromagnetism in rhodium metal at positive and negative nanokelvin temperatures.* Phys. Rev. Lett. **70**, 2818 (1993).

List of Figures